From Palladium Chalcogenides to Iron Complexes: Understanding Structure-Function Relationships in Crystals and in Molecules

Glen J. Murray, MSci Hons

Thesis submitted to the University of Nottingham for Degree of Doctor of Philosophy

October 2020

Declaration

The work described in this thesis was carried out at the University of Nottingham between July 2016 and October 2019, under the supervision of Dr Maria Gimenez-Lopez and Prof Deborah L. Kays. All of the work is my own unless stated to the contrary and has not previously been submitted for any degrees at this or any other university.

Glen J. Murray

Abstract

This thesis is an investigation into the structure-function relationship of a range of different materials and molecules. In Chapter 2 a newly synthesised hybrid material palladium sulfide nanoparticles encapsulated at milled carbon nanofibers (PdS_x@CNF_m). PdS_x@CNF_m is investigated for its activity towards the hydrogen evolution reaction (HER) and exhibits switchable behaviour even after extended chronoamperometric and cycling studies. Electrochemical performance is related to structure through high-resolution transmission electron microscopy (HRTEM) and electron dispersive X-ray spectroscopy (EDS) before and after activation. Changes of the internal corrugated structure of the carbon nanofiber support as well as changes to the PdS_x nanoparticles are proposed as a mechanism for the switchable behaviour.

Chapter 3 investigates a set of *m*-terphenyl iodide precursors based on 2,6-$Ar_2C_6H_3I$ where Ar = 2,4,6-$Me_3C_6H_2^-$ (Mes) functionalised at the *para* position of the central aryl ring. Synthetic routes are described and carried out with the aim of studying the structural influence on the catalytic or magnetic properties of subsequent low-coordinate complexes. The concept is tested using a phenyl group initially followed by a pyrene moiety to exploit the non-covalent interactions between pyrene and carbon surfaces.

Chapter 4 investigates a range of spin crossover (SCO) materials with large and flexible high charge tetracarboxylate anions (TCA) in the form $[Fe(3\text{-}Bpp)_2]_2[TCA].xH_2O$ (3-Bpp = 2,6-bis(pyrazol-3-yl)pyridine). Switchable magnetic bistability is investigated through magnetic measurements and correlated to X-ray crystallographic data to rationalise the deviation from expected magnetic behaviours.

Acknowledgements

Firstly, I want to thank my supervisor Maria for giving me the opportunity to undertake this research and for giving me a wide range of topics to investigate. Without her this work would not have been possible. I would like to thank Dr Carlos Herreros-Lucas for the synthesis and characterisation of $PdS_x@CNF_m$ and for always being on hand as a sounding board for ideas whether in the UK or Spain. Dr Abdullah Kurtoglu for his work with Carlos developing the materials investigated and Dr Mehtap Aygun for her guidance in the early electrochemistry and throughout.

For their support and friendship, I would like the thank Graham Newton and the rest of the Newton group during my time in B45 alongside members of the Khlobystof group who have always been a crutch to lean on since my masters project in their lab.

I have so much gratitude towards everyone in the Kays group and my choice to move to B46 was made very special by Debbie whose support has been invaluable and everyone who helped in my transition to air sensitive work. Their love for chemistry is infectious, I have learned a great deal from them, they are all exceptional scientists.

Thanks to all the technical staff at Nottingham; Shaz and Kev for NMR, Graeme and Mick for mass spectrometry, Sandy and Dr Will Lewis for their help with crystallography and the opportunity to be involved with Diamond Light Source trips and Stephen Argent when he took over.

Finally, I would like to thank my family for their unconditional support. Most importantly I would like to thank Hayley for bringing excitement and unconditional support when things were their hardest.

Abbreviations

1-Bpp	2,6-bis(pyrazol-1-yl)pyridine
1D	one-dimensional
2D	two-dimensional
3-Bpp	2,6-bis(pyrazol-3-yl)pyridine
3D	three-dimensional
AE	alkali electrolyser
ATR	attenuated total reflectance (IR absorption)
Ar	aryl
BEV	battery electric vehicle
CA	chronoamperometry
CNF	carbon nanofiber
CNF_m	milled carbon nanofiber
CNTs	carbon nanotubes
Cold-FEG	cold field emission gun
CV	cyclic voltammetry
d	doublet (NMR)
DCM	dichloromethane
DFT	density functional theory

EDS	electron dispersive X-ray spectroscopy
EPSRC	engineering and physical sciences research council
ESI	electrospray ionisation
FCEV	fuel cell electric vehicle
GCE	glassy carbon electrode
HER	hydrogen evolution reaction
HS	high spin
I	*ipso*
IR	*Infrared*
^{i}Pr	isopropyl
iR	ohmic potential drop
J	coupling constant (NMR)
LIBs	lithium ion batteries
LS	low spin
LSV	linear scan voltammetry
m	*meta*
m	multiplet (NMR)
Mes	mesityl
MOFs	metal organic framework

MS	mass spectrometry
MWCNTs	multi walled carbon nanotubes
^{n}BuLi	*n*-butyl lithium
NHC	*N*-heterocyclic carbene
NMR	nuclear magnetic resonance spectroscopy
o	*ortho*
OER	oxygen evolution reaction
p	*para*
Pd/AC	palladium on activated charcoal
PdNP	palladium nanoparticles
PdNP@CNFm	palladium nanoparticles encapsulated in milled carbon nanofibres
PEMFC	proton exchange membrane fuel cell
PEM-WE	proton exchange membrane water electrolyser
ppm	parts per million
Pt/C	platinum on amorphous carbon black
q	quartet (NMR)/quaternary (^{13}C NMR)
R	alkyl chain
s	singlet
SCE	saturated calomel electrode

SOE	solid oxide electrolyser
SQUID	super conducting quantum interference device
St	stability test
SWCNTs	single walled carbon nanotubes
t	triplet
^{t}Bu	*t*-butyl
TCA	tetracarboxylate anion
TEM	transmission electron microscopy
THF	tetrahydrofuran
UKRI	UK research institute
vdWs	van der Waals forces
XRD	X-ray diffraction
δ	chemical shift
η10	overpotential at 10 $mAcm^{-2}$
π	pi orbital
σ	sigma orbital

Contents

List of Figures

Table of Schemes

Table of Tables

Chapter 1

Introduction

Chapter 1

1.1 Introduction

1.1.2 Overview

There are two overruling areas of interest for discussion in this thesis; new materials for use as electrodes in energy applications and the investigation of solid-state interactions in magnetic materials and low coordinate metal centres. The use of hybrid metal carbon nanostructures for energy storage applications will be discussed alongside the synthesis of spin crossover materials based on anion exchange of $[Fe(3\text{-}Bpp)_2][SO_4]$ and the synthesis of *para* functionalised *m*-terphenyl iodide ligands. These areas encompass intermolecular interactions and the interface between solution and solid phases. The physical and chemical adsorption of species to a solid surface are at the heart of electrochemical catalysis and the hydrogen bonding and π-π interactions in the solid-state are the basis for cooperativity in spin crossover materials.

1.1.3 Electrochemistry for Energy storage

Electrochemical techniques are useful in a wide range of application, from compound characterisation to detection of analytes, electrodeposition and most importantly to this thesis are essential for driving research in new energy applications. For example, the UK research institute (UKRI) Energy theme led by the Engineering and Physical Sciences Research Council (EPSRC) has £312.97 million worth of funding in this area.[1] Public interest has been shown to be highly favourable towards long term commitment to a more sustainable energy system.[2]

The world energy council publishes yearly global energy rankings based on three energy descriptors: energy security, energy equity and environmental sustainability. Their rankings

encourage diversifying energy production, increasing access to energy and policies for overall price reduction and directing change towards the sustainable decarbonisation of energy production.[3] As an example of decarbonisation the UK has made significant steps in decarbonising the production of electricity almost completely removing coal, however this improvement has not been seen in the automotive industry. With the implementation of battery electric vehicles and/or hydrogen fuel cell electric vehicles and their hybrids this will decrease the generation of greenhouse gases from automotives.[4] This is emphasised in the Ofgem decarbonisation programme action plan[5] and by the committee on climate change.[6] There is no consensus on any one plan to reach the ambitious zero carbon emissions set by many governments and as shown by many of these policy reports it will differ from nation to nation. However, there is a consensus that many different technologies will be involved in renewable energy generation including solar, offshore wind, hydrothermal alongside carbon capture technology.[7] Energy storage is therefore of a high priority in order to deal with the usual unpredictability of the renewable electricity. Hydrogen has excellent energy density as a fuel 120 kJ/g compared with conventional hydrocarbon fuels ~50 kJ/g.[8] Hydrogen can then be stored, transported and used in multiple process streams such as hydrogen fuel cells and in combination with natural gas. When burned the only by-product is water making renewable energy produced hydrogen a carbon zero source of energy.

When produced using the electricity sources mentioned above by electrolysis, hydrogen is carbon zero, unfortunately it is primarily produced from fossil fuels with as little as 4% being from electrolysis. The disparity is mainly due to the high cost of renewable energy. With the improvement of renewable energy sources production of hydrogen from water splitting has become more viable.[9] Commercial water electrolysers have three main technologies, alkaline

electrolysers (AE), proton exchange membrane water electrolysers (PEM-WE) and solid oxide electrolysers (SOE). Each has its benefits, AE is the cheapest and most readily available method however suffers from low current densities 400 mA/cm^2 with low operation pressures 25-30 bar and temperatures of 5-100 ^{o}C. SOE benefit from high pressure and temperature operation of more than 50 bar and 500-850 ^{o}C suitable for industrial application with high current densities of more than 3 A/cm^2. However, SOE suffer from stability and degradation issues. Finally, PEM-WE use the same concepts as proton exchange membrane fuel cells (PEMFC) working in the backwards mode, these have much higher current density than AE at 2 A/cm^2 working at 50-80 ^{o}C and generate ultrapure H_2 99.999% at pressures below 30 bar. PEM-WE suffer from expensive noble metal HER and OER catalysts.[10,11]

Hydrogen as an energy vector has opportunities throughout the decarbonisation efforts for the energy supply chains including the need to move away from natural gas heating of homes and towards electric vehicles.[12,13] Once the production of carbon zero hydrogen is sufficiently cheap at a grid scale then the investment in the lower level infrastructure such as filling stations, etc. will follow as commercial fuel cell electric vehicles (FCEV) are already available. Carbon zero production of hydrogen would also decarbonise all industries that use hydrogen such as synthetic hydrocarbon production.[14] Until such time, the implementation of carbon capture technology in current reformation methods could allow the transition to hydrogen as a fuel.[7] Hydrogen produced from fossil fuel sources requires purification for use in PEMFCs due to poisoning of the catalysts which will add additional costs. Production of hydrogen by PEM-WE from renewable energy can be used directly with PEMFCs making it a closed loop system. If the end goal of the produced hydrogen is not PEMFC the only by-product of the

splitting is oxygen which can be also be collected from the electrolysis and utilised elsewhere. However, efficiencies of electrolysers are not currently capable of making this viable.[10]

The area of energy research can be further broken down into specific applications with high public interest such as battery technology and hydrogen economy including fuel cells and hydrogen production which have been widely reviewed.[4,15–20] These areas of research also encompass a huge cross disciplinary effort involving academia, industrial research and development and legislative bodies. As the technologies involved are at different stages of development a cross disciplinary approach is required to speed up integration into current infrastructures.[21]

As mentioned earlier, the use of hydrogen is no longer being proposed as a singular solution to global energy demands, but electrochemistry underpins each energy solution. Research towards a hydrogen economy, battery technology and supercapacitors can be further reduced to the individual cathodic and anodic reactions occurring at the electrodes of the system dependant on the chemistry of the system in question. This is represented graphically by **Figure 1. 1**, which is by no means exhaustive, but gives an idea of the immense scale of the challenge and the applicability of electrochemistry to this real-world problem.

Each electrode for each application will have a set of required properties underpinned by the target electrochemical reaction and the application for which it is intended. For example, the criteria for a cathode material for PEM water electrolysis needs to be stable at negative potentials in acidic conditions, be sufficiently active to produce hydrogen under low overpotentials, be electrically conductive. Although PEMFC and PEM-WE are commercially available there is still room for performance and cost improvements, the state-of-the-art cathode is still Pt/C, and has been for some time.[22,23] The extremely fast kinetics of the

hydrogen evolution reaction and hydrogen oxidation reaction at cathode mean they are not a limiting factor in the performance and scale up of production. The high cost of the Pt at the cathode can be offset slightly by the high performance and therefore low loading, however sluggish kinetics at the anode for the OER mean that high anode metal loading is required to generate adequate currents.[16,24]

Alongside a hydrogen economy, advancement in battery technology and chemistries figure headed by the Nobel Prize winning discovery of lithium-ion batteries will be significant contributors to the energy challenge. Depending on the chemistries involved batteries can, like hydrogen, lend themselves to different energy application. For example, sodium ion batteries due to their lower energy density but decreased cost and increased Na abundance compared with LIBs show promise for larger grid storage applications.[25–27] LIB developments including layered transition metal oxide cathodes have led to high charge density and longer range battery electric vehicles can now demonstrate comparable range to combustion engine cars.[28,29] Materials for battery cathodes and anodes must intercalate ions at potentials as far removed from each other as possible in order to increase cell voltage.[30] Another string to the bow of energy storage applications are supercapacitors; the application for supercapacitors overlaps with the potential applications of LIBs which deliver high energy density sacrificing power depending on design, supercapacitors have much faster charge/discharge and high power output. They can be used alongside LIBs to smooth out high power electrical energy and deliver high power energy for example when accelerating and breaking for energy recovery in battery electric vehicles (BEVs) and hybrid BEVs.[31] Supercapacitors can work from a variety of different mechanisms including intercalation mechanisms similar to that found in LIBs and hybrid variants,[32] and **Figure 1. 1** highlights electric double layer capacitors which

involve psuedocapacitance formed from the deposition of electrolyte on the surface of a carbon anode or metal oxide cathode.[33]

A running theme throughout all the applications introduced here which has yet to be properly covered is the use of carbon.[22,34] It is used in a huge array of applications across the breadth of electrochemical analysis and application. It can be used as an additive for machinability and conductivity in battery cathodes,[28] active catalyst,[35,36] support,[22,34,37–40] working electrode[41] and counter electrode.[42] Carbon materials are materials with a huge repertoire of applications due to their high degree of functionalisation and the structures involving carbon that can be achieved. The range of different conformations and allotropes of pure carbon that can be expanded by the functionalisation means that it dominates the electrocatalysis literature. Carbon has been exploited in batteries as an anode in the form of graphite for lithium ion chelation with the addition of silicon, and in the cathode as amorphous carbon black to improve the electrical contact. Where high cost metal catalysts are used for HER and OER it has been exploited as a metal free catalyst when doped with heteroatoms such as nitrogen and sulfur or even just the presence of defects is capable of increasing catalytic performance which will be covered in the Chapter 2.[43–45] We will show in the form of carbon nanofibers it is electrochemically non-innocent as a substrate. When reducing catalyst loading for HER carbon in the form of graphene[34], single[46] and multi-walled[47] carbon nanotubes, graphitised carbon nanofibers[48] (CNFs) and amorphous carbon black (Pt/C)[49] have all been shown to reduce catalyst loading, improve electrical conductivity, provide increased active sites for proton adsorption.

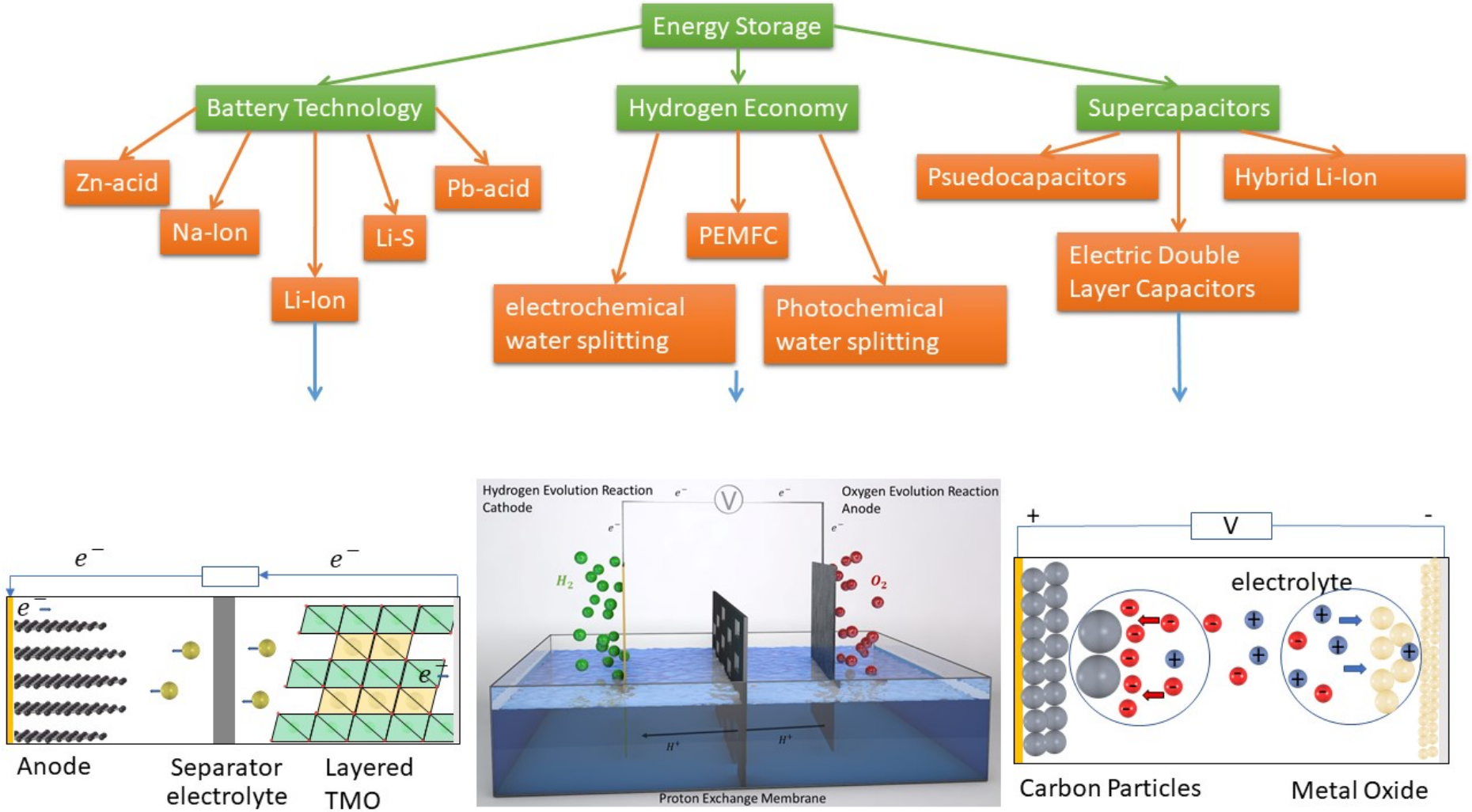

Figure 1. 1 *Schematic representation of the wide range of chemistries and applications of electrochemistry in energy storage applications showing Li-Ion batteries (LIB)*[50]*, Proton exchange membrane electrolysis*[51] *and electric double layer capacitors (EDLCs).*[33]

The electrochemical investigations in this thesis have their sights set on tackling the challenges put forward by this global endeavour. However, they are firmly set at the early stages of that journey, in the discovery and investigation of new materials for energy application. In this endeavour the HER shown in eq. 1.2 under standard conditions is an ideal system to start with due to its well defined kinetics, practical methods and reaction mechanisms.[51] HER is a multistep two-electron transfer process taking place at the cathode with three possible mechanisms eq. 1.6,7,8. The route to developing new materials has been driven by many factors including costs, availability and performance.[52] The electrolysis of water consists of the cathodic HER and the anodic OER eq. 1.3 which can occur in basic and acidic conditions under different mechanisms.[53] Electrolysers can be designed to work under basic (eq. 1.4,1.5) and neutral conditions but are most commonly used in acidic conditions (eq. 1.2,1.3) due to the lower operating temperatures and more benign by-products.

Total reaction $2H_2O \rightarrow 2H_2 + O_2$ (1.1)

In acidic electrolyte:

Cathode: $2H^+ + 2e^- \rightarrow H_2,\ E_c = 0\ V$ (*vs.RHE*) (1.2)

Anode: $2H_2O \rightarrow O_2 + 4H^+ + 4e^-, E_a = 1.23\ V$ (*vs.RHE*) (1.3)

In alkaline electrolyte:

Cathode: $2H_2O + 2e^- \rightarrow H_2 + 2OH^-, E_c = -0.83\ V$ (*vs.RHE*) (1.4)

Anode: $4OH^- \rightarrow O_2 + 2H_2O + 4e^-, E_a = -0.40\ V$ (*vs.RHE*) (1.5)

As electrochemistry is a surface technique it is probing the interface between the solid-liquid phase boundary at the electrodes. The interactions between the catalyst surface and the

adsorbed species H^* are key to optimising the catalyst performance, this is qualitatively represented by volcano plots **Figure 1. 2** and was used computationally to predict new materials by density functional theory (DFT) calculations, as reported by Nørskov et al.[54] They were able to predict the binding energy of MoS_2 as a good candidate material for HER catalysis which kick started a huge effort to develop effective MoS_2 catalysts leading to the refinement of this technology and the discovery of edge site activity and a plethora of intricate supported MoS_2 hybrid materials.[37,55–62]

$H_3O^+ + e^- + * \rightarrow H^* + H_2O$, Volmer reaction (1.6)

$H^* + H_3O^+ + e^- \rightarrow H_2 + H_2$, Heyrovsky reaction (1.7)

$H^* + H^* \rightarrow H_2$, Tafel reaction (1.8)

The hydrogen evolution reaction proceeds via two mechanistic steps, proton adsorption on an active site represented by * eq. 1.6, followed by either the electrochemical desorption of hydrogen the Heyrovsky reaction eq. 1.7 or the chemical desorption of hydrogen the Tafel reaction eq. 1.8.

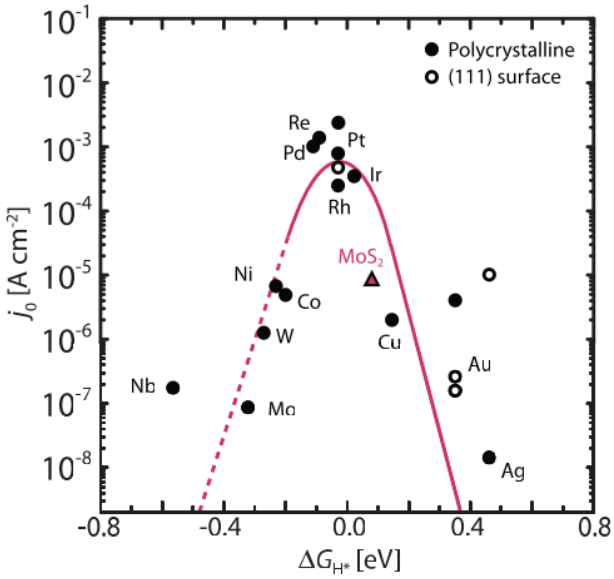

Figure 1. 2 *HER volcano plot for MoS_2 showing current density j_0 (A cm^{-2}) vs Gibbs free energy of adsorption of a proton ΔG_{H^*} taken from*[54]

The volcano plot is a good indicator of the performance of a catalyst as optimum proton binding energies allow protons to be adsorbed and desorbed with minimal overpotentials, however there are many other contributing factors including active site density which was initially an issue for MoS_2.[62] Free energy diagrams shown in **Figure 1. 3** show the computed

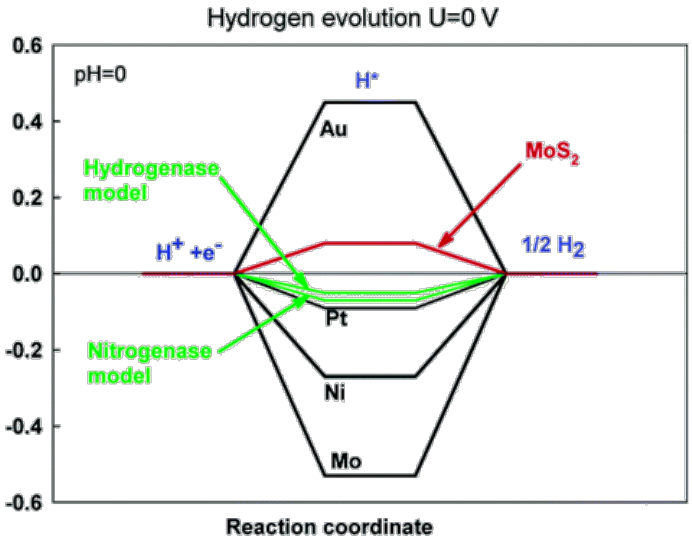

Figure 1. 3 *Computed free energy for HER at standard pressure and temperature and a potential of U = 0 vs. SHE, with pH = 0. The result for MoS2 is the free energy required to increase the hydrogen coverage from 25% to 50%.*[63]

The thermodynamic equilibrium potentials for water splitting are shown in eq. 1.2 and 1.3 for the HER and OER, these values are not practical. Overpotential η refers to the additional potentials required to overcome practical aspects of the process.

$$E_{op} = 1.23\ V + \eta_a + \eta_c + \eta_{other} \quad (1.9)$$

E_{op} is the operating potential, η_a and η_c refer to anodic and cathodic overpotentials respectively. The theoretical potential for the HER being 0 means that any deviation from this is the overpotential. Activation overpotentials η_a and η_c can be reduced by the choice and design of the electrode materials i.e. the choice of catalyst. η_{other} is a combination of practical effects caused by concentration limitations due to the consumption of ions at the electrode surface and the formation of a diffusion gradient from bulk to surface. This can be overcome by high concentrations of protons and stirring of the solution. Electrolyte resistance can increase the overpotential but is accounted for by an iR correction calculation.[64]

When screening catalysts for the HER a three electrode setup is used including a glassy carbon working electrode, reference hydrogen electrode (RHE) and a counter electrode usually platinum however this has certain practical issues involved with the dissolution of Pt at high positive potentials and extensive cycling.[42] A set of catalytic indicators including onset potential, Tafel slope, overpotential at 10 $mAcm^{-2}$, cycling stability and exchange current density obtained through linear sweep voltammetry and Tafel plots. These are further explained in the Chapter 2.

1.1.4 Intermolecular Interactions for Immobilisation

The adsorption of a proton on the surface of an electrode is a charge transfer interaction between the negative electrode and the positive proton, where the equilibrium is driven by an applied potential. This differs from the intermolecular interactions that govern the behaviours explored in the chapters 3 and 4 involving metal complexes in the solid state. In these chapters the intermolecular interactions which underpin the behaviours of interest are a combination of attractive forces, from short range vdWs interactions to π- π interactions, anion-π interactions, hydrogen bonds and ionic interactions.[65–68] The combination and control of these interactions is the basis of the field of crystal engineering.[69,70] Through the control of structure and understanding the fundamental influence of the intermolecular interactions on the desired properties it is possible to move towards controlling function. Intermolecular interactions have been observed to play a significant role in biological systems[71] and are now regularly exploited for the hybridisation of materials for applications including single molecule magnets,[72] host guest interaction in supramolecular systems[73] and anchoring of catalysts which will be further explored later.

Anchoring of molecules is achieved through a variety of interactions and is particularly useful in single molecule magnets, in order for these materials to be employed in spintronic applications and devices they must be successfully adhered to conductive surfaces and studied whilst maintaining their bistable properties.[74] Various approaches to grafting these complexes have been explored including long chain alkyl groups terminated with sulfur moieties for grafting to gold surfaces[75], phosphonates, carboxylates and methyl silanes are used to graft to metal oxide surfaces[76], encapsulation can also be exploited.[77]

1.1.5 Spin Crossover

The phenomenon of spin crossover has been reviewed and revisited many times since its discovery by Cambi et al.[78–81] Complexes with electronic configuration d^{4-7} are capable of switching between low spin (LS) and high spin (HS) states through the application of an external perturbation such as temperature, pressure, light and an applied magnetic field. The properties displayed are still of significant interest for data storage, molecular sensors, and display devices.[80,82] Currently spin crossover research areas are focussing on metal organic frameworks (MOFs) and two dimensional coordination polymers.[83,84] Molecular design in Fe(II) d^6 complexes has lead to the synthesis of a huge number of 2,6-bis(pyrazol-1-yl)pyridine (1-Bpp) and 2,6-bis(pyrazol-3-yl)pyridine (3-Bpp) derivatives being functionalised at each available position.[85–90]

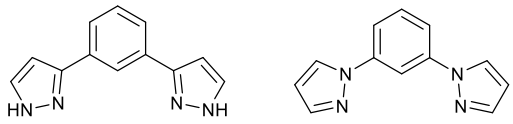

Figure 1. 4 *Chemical structure of isomers 2 6-bis(pyrazol-1-yl)pyridine and 2 6-bis(pyrazol-3-yl)pyridine*

The family of terpyridine like ligands based on 1-Bpp and 3-Bpp **Figure 1. 4** show a highly cooperative spin transition in the solid state due to their intermolecular interactions, the correlation of these interactions to the function of a material is highly desirable for designing new materials and this has been a significant trend in spin crossover research.[69,91,92] Investigation into the first coordination sphere and ligand design are extensive. The spin transitioin of these terpyridine based ligands are also highly susceptible to changes in the second coordination sphere and specifically for the 3-Bpp isomer any hydrogen bonding interactions. **Figure 1. 5** shows an investigation by the Gimenez-Lopez group on the substitution of small discrete counterions like SO_4, Cl^-,Br^-, NO_3 etc. which have been

investigated previously to larger and higher charge counterions. Through crystallographic and magnetic measurements, it is possible to correlate the structural changes of the hydrated and dehydrated complexes to the magnetic susceptibility measurements and rationalise the changes.

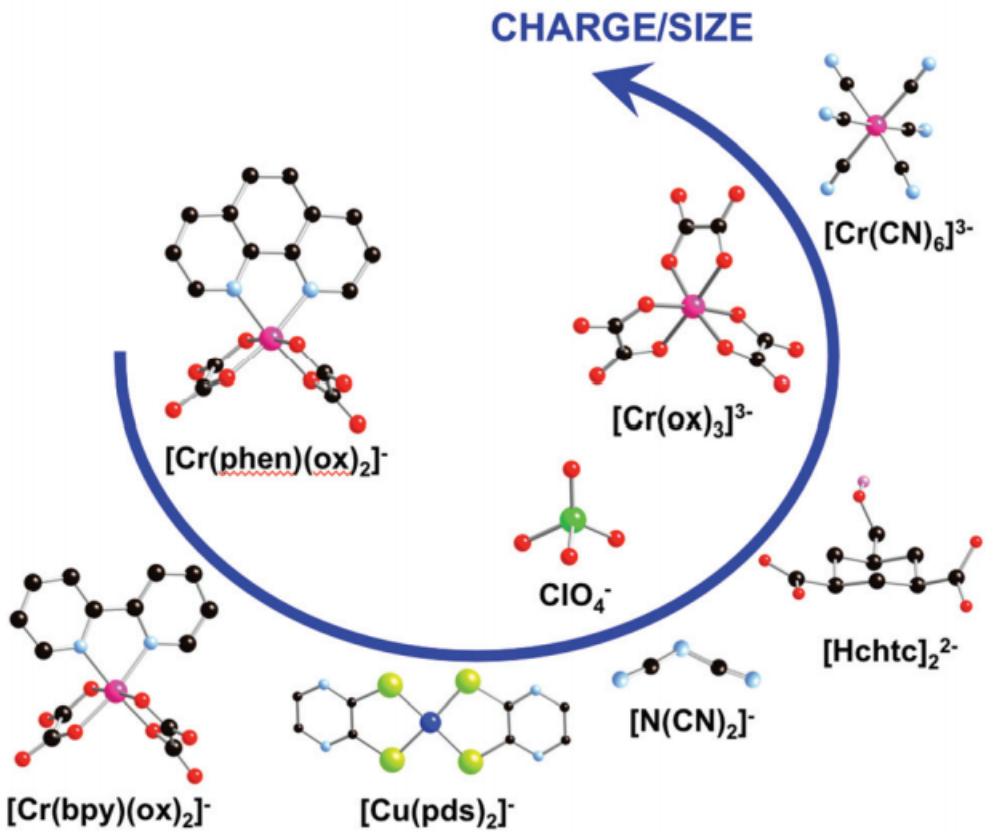

Figure 1. 5 *Study of size/charge ratio in* $[Fe(3\text{-}Bpp)_2]^{2+}$ *counterions by the Gimenez Lopez Group*[92]

An advancement of this work is to move towards counterions based on organic carboxylates. Previous reports show the ability of these compounds to form porous hydrogen bonded networks. **Figure 1. 6** shows examples of $[Fe(3\text{-}Bpp)_2]^{2+}$ complexes with organic carboxylate counterions in the form of adipate and cyclohexanetricarboxylate.

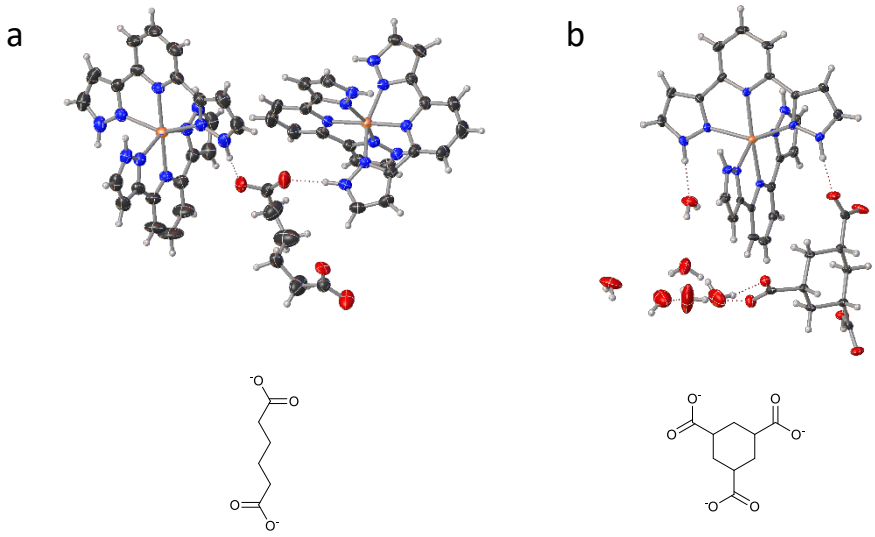

Figure 1. 6 *a) Crystal structure for 2[Fe(3-Bpp)$_2$][$C_6H_8O_4$][93] b) Fe(3-Bpp)$_2$]($C_9H_{10}O_6$)·5.5H_2O[94]*

1.1.6 Scope and objectives

The aim of this project is to synthesise and investigate new materials for energy, magnetic and catalytic applications. The emphasis being on novel structures guided by principles covered in the introduction. The resulting materials will therefor give insight into the structure-function relationship of the chosen application and further guide the synthesis of new materials.

Chapter 2 aims to explore the activity of a PdS_x@CNF_m composite towards the hydrogen evolution reaction (HER). The material exhibits switchable behaviour even after extended chronoamperometric and cycling studies. Electrochemical performance is related to structure through high-resolution transmission electron microscopy (HRTEM) and electron dispersive X-ray spectroscopy (EDS) before and after activation. Changes of the internal corrugated structure of the carbon nanofiber support as well as changes to the PdS_x nanoparticles are proposed as a mechanism for the switchable behaviour.

Chapter 3 aims to synthesise a set of *m*-terphenyl iodide precursors based on 2,6-$Ar_2C_6H_3I$ where Ar = 2,4,6-$Me_3C_6H_2$ - (Mes) functionalised at the para position of the central aryl ring. *m*-Terphenyl ligands have been successfully functionalised with a variety of flanking aryl groups and buttressing groups. A small range of functional groups have been used at the para position however these are generally restricted to electron donating and withdrawing groups. In the case of low coordinate metal centres this has not extended to tethering or immobilising groups. Synthetic routes are described and carried out with the aim of studying the structural influence on the catalytic or magnetic properties of subsequent low-coordinate complexes. The synthetic routes are tested using a phenyl group initially followed by a pyrene moiety to exploit the non-covalent interactions between pyrene and carbon surfaces.

Chapter 4 focuses on the synthesis of a range of spin crossover (SCO) materials with large and flexible high charge tetracarboxylate anions (TCA). The 3-Bpp ligand is chosen to form Fe(II) complexes due to its free pyrazole NH function capable of forming hydrogen bonds. $[Fe(3\text{-}Bpp)_2]^{2+}$ is known to be susceptible to hydrogen bonding from solvent molecules in solution affecting the spin transition temperature. In the solid-state, hydrogen bonding networks can be formed increasing cooperativity in the spin transition. Using a metathesis reaction, discrete counterions can be exchanged for the large TCA molecules which can act as hydrogen bond acceptors. Materials in the form $[Fe(3\text{-}Bpp)_2]_2[TCA].xH_2O$ were synthesized and characterised. Switchable magnetic bistability is investigated through magnetic measurements and correlated to X-ray crystallographic data to rationalise the deviation from expected magnetic behaviours.

1.2 References

1 https://epsrc.ukri.org/research/ourportfolio/themes/energy/.

2 C. Hepburn, N. Winser CBE FREng and P. Richard Parker CBE FREng, 1–8.

3 World Energy Council, *Trilemma Index*, 2019, 1–79.

4 Y. Manoharan, S. E. Hosseini, B. Butler, H. Alzhahrani, B. T. F. Senior, T. Ashuri and J. Krohn, *Appl. Sci.*, 2019, 9.

5 Ofgem, *Ofgem*, 2020, 13.

6 Committee on Climate Change, *Hydrogen in a low-carbon economy*, 2018.

7 M. Voldsund, K. Jordal and R. Anantharaman, *Int. J. Hydrogen Energy*, 2016, **41**, 4969–4992.

8 K. T. Møller, T. R. Jensen, E. Akiba and H. wen Li, *Prog. Nat. Sci. Mater. Int.*, 2017, **27**, 34–40.

9 Y. Yao, X. Gao, Z. Li and X. Meng, *Catalysts*, 2020, **10**, 335.

10 S. Shiva Kumar and V. Himabindu, *Mater. Sci. Energy Technol.*, 2019, **2**, 442–454.

11 J. P. Hughes, J. Clipsham, H. Chavushoglu, S. J. Rowley-Neale and C. E. Banks, *Renew. Sustain. Energy Rev.*, 2021, **139**, 110709.

12 I. Staffell, D. Scamman, A. Velazquez Abad, P. Balcombe, P. E. Dodds, P. Ekins, N. Shah and K. R. Ward, *Energy Environ. Sci.*, 2019, **12**, 463–491.

13 N. P. Brandon and Z. Kurban, *Philos. Trans. R. Soc. A Math. Phys. Eng. Sci.*, 2017, **375**,

20160400.

14 K. Ayers, *MRS Energy Sustain.*, 2017, **4**, 1–10.

15 Z. Abdin, A. Zafaranloo, A. Rafiee, W. Mérida, W. Lipiński and K. R. Khalilpour, *Renew. Sustain. Energy Rev.*, 2020, **120**, 109620.

16 J. O. Abe, A. P. I. Popoola, E. Ajenifuja and O. M. Popoola, *Int. J. Hydrogen Energy*, 2019, **44**, 15072–15086.

17 Z. P. Cano, D. Banham, S. Ye, A. Hintennach, J. Lu, M. Fowler and Z. Chen, *Nat. Energy*, 2018, **3**, 279–289.

18 A. R. Dehghani-Sanij, E. Tharumalingam, M. B. Dusseault and R. Fraser, *Renew. Sustain. Energy Rev.*, 2019, **104**, 192–208.

19 I. Vinoth Kanna and P. Paturu, *Int. J. Ambient Energy*, 2020, **41**, 1433–1436.

20 C. Acar and I. Dincer, *J. Clean. Prod.*, 2019, **218**, 835–849.

21 E. Rozzi, F. D. Minuto, A. Lanzini and P. Leone, *Energies*, 2020, **13**, 420.

22 A. Eftekhari, *Int. J. Hydrogen Energy*, 2017, **42**, 11053–11077.

23 M. Bernt, A. Siebel and H. A. Gasteiger, *J. Electrochem. Soc.*, 2018, **165**, F305–F314.

24 N. T. Suen, S. F. Hung, Q. Quan, N. Zhang, Y. J. Xu and H. M. Chen, *Chem. Soc. Rev.*, 2017, **46**, 337–365.

25 J. Y. Hwang, S. T. Myung and Y. K. Sun, *Chem. Soc. Rev.*, 2017, **46**, 3529–3614.

26 N. Yabuuchi, K. Kubota, M. Dahbi and S. Komaba, *Chem. Rev.*, 2014, **114**, 11636–11682.

27 J. W. Choi and D. Aurbach, *Nat. Rev. Mater.*, 2016, **1**, 420.

28 T. Kim, W. Song, D. Y. Son, L. K. Ono and Y. Qi, *J. Mater. Chem. A*, 2019, **7**, 2942–2964.

29 X. Wang, Y. L. Ding, Y. P. Deng and Z. Chen, *Adv. Energy Mater.*, 2020, **10**, 1–28.

30 A. Manthiram, *Nat. Commun.*, 2020, **11**, 1–9.

31 Poonam, K. Sharma, A. Arora and S. K. Tripathi, *J. Energy Storage*, 2019, **21**, 801–825.

32 J. Ronsmans, B. Lalande and J. S. R. M. N. V, .

33 P. Simon, Y. Gogotsi and B. Dunn, *Science.*, 2014, **343**, 1210–1211.

34 S. Shahgaldi and J. Hamelin, *Carbon N. Y.*, 2015, **94**, 705–728.

35 X. Zou and Y. Zhang, *Chem. Soc. Rev.*, 2015, **44**, 5148–80.

36 C. Tang and Q. Zhang, *Adv. Mater.*, 2017, **29**, 1604103.

37 V. Georgakilas, J. N. Tiwari, K. C. Kemp, J. A. Perman, A. B. Bourlinos, K. S. Kim and R. Zboril, *Chem. Rev.*, 2016, **116**, 5464–5519.

38 S. Verma, S. Sinha-Ray and S. Sinha-Ray, *Polymers (Basel).*, 2020, **12**, 43–47.

39 Y. Shao, G. Yin, J. Zhang and Y. Gao, *Electrochim. Acta*, 2006, **51**, 5853–5857.

40 J. Speder, A. Zana, I. Spanos, J. J. K. Kirkensgaard, K. Mortensen, M. Hanzlik and M. Arenz, *J. Power Sources*, 2014, **261**, 14–22.

41 Y. Yi, G. Weinberg, M. Prenzel, M. Greiner, S. Heumann, S. Becker and R. Schlögl, *Catal. Today*, 2017, **295**, 32–40.

42 G. Dong, M. Fang, H. Wang, S. Yip, H. Y. Cheung, F. Wang, C. Y. Wong, S. T. Chu and J. C. Ho, *J. Mater. Chem. A*, 2015, **3**, 13080–13086.

43 G. P. Wu, Y. Y. Wang, D. H. Li, C. X. Lu, W. Z. Shen, X. T. Li and Z. H. Feng, *Carbon N. Y.*,

2011, **49**, 2152–2155.

44 Y. A. Kim, T. Hayashi, J. H. Kim and M. Endo, *J. Energy Chem.*, 2013, **22**, 183–194.

45 A. Ambrosi, A. Bonanni and M. Pumera, *Nanoscale*, 2011, **3**, 2256–2260.

46 J. Wu, Y. Xue, X. Yan, W. S. Yan, Q. M. Cheng and Y. Xie, *Nano Res.*, 2012, **5**, 521–530.

47 M. Xiao, X. Liang, W. Li, Y. Yang and Y. Miao, *J. Electrochem. Soc.*, 2015, **162**, H415–H418.

48 M. del Carmen Gimenez-Lopez, A. Kurtoglu, D. A. Walsh and A. N. Khlobystov, *Adv. Mater.*, 2016, **28**, 9103–9108.

49 S. A. Grigoriev, P. Millet and V. N. Fateev, *J. Power Sources*, 2008, **177**, 281–285.

50 Z. Chen, W. Zhang and Z. Yang, *Nanotechnology*, 2020, **31**, 012001.

51 J. Tymoczko, F. Calle-Vallejo, W. Schuhmann and A. S. Bandarenka, *Nat. Commun.*, 2016, **7**, 10990.

52 Y. Li, Y. Sun, Y. Qin, W. Zhang, L. Wang, M. Luo, H. Yang and S. Guo, *Adv. Energy Mater.*, 2020, **10**, 1–20.

53 J. K. Norskov, T. Bligaard, A. Logadottir, J. R. Kitchin, J. G. Chen and S. Pandelov, *J. Electrochem. Soc.*, 2005, **152**, J23–J26.

54 Z. W. She, J. Kibsgaard, C. F. Dickens, I. Chorkendorff, J. K. Nørskov and T. F. Jaramillo, *Science.*, 2017, **355**, 1–12.

55 J. D. Benck, T. R. Hellstern, J. Kibsgaard, P. Chakthranont and T. F. Jaramillo, *ACS Catal.*, 2014, **4**, 3957–3971.

56 Z. Luo, Y. Ouyang, H. Zhang, M. Xiao, J. Ge, Z. Jiang, J. Wang, D. Tang, X. Cao, C. Liu and W. Xing, *Nat. Commun.*, 2018, **9**, 1–8.

57 D. M. Hou, W. J. Zhou, X. J. Liu, K. Zhou, J. Xie, G. Q. Li and S. W. Chen, *Electrochim. Acta*, 2015, **166**, 26–31.

58 T. F. Jaramillo, K. P. Jorgensen, J. Bonde, J. H. Nielsen, S. Horch and I. Chorkendorff, *Science.*, 2007, **317**, 100–102.

59 B. B. Li, S. Z. Qiao, X. R. Zheng, X. J. Yang, Z. D. Cui, S. L. Zhu, Z. Y. Li and Y. Q. Liang, *J. Power Sources*, 2015, **284**, 68–76.

60 B. J. Guo, K. Yu, H. L. Li, H. L. Song, Y. Y. Zhang, X. Lei, H. Fu, Y. H. Tan and Z. G. Zhu, *ACS Appl. Mater. Interfaces*, 2016, **8**, 5517–5525.

61 Y. G. Li, H. L. Wang, L. M. Xie, Y. Y. Liang, G. S. Hong and H. J. Dai, *J. Am. Chem. Soc.*, 2011, **133**, 7296–7299.

62 U. Gupta and C. N. R. Rao, *Nano Energy*, 2017, **41**, 49–65.

63 B. Hinnemann, P. G. Moses, J. Bonde, K. P. Jørgensen, J. H. Nielsen, S. Horch, I. Chorkendorff and J. K. Nørskov, *J. Am. Chem. Soc.*, 2005, **127**, 5308–5309.

64 Z. Li, R. Ge, J. Su and L. Chen, *Adv. Mater. Interfaces*, 2020, **7**, 1–13.

65 G. Zhao, X. Li, M. Huang, Z. Zhen, Y. Zhong, Q. Chen, X. Zhao, Y. He, R. Hu, T. Yang, R. Zhang, C. Li, J. Kong, J. Bin Xu, R. S. Ruoff and H. Zhu, *Chem. Soc. Rev.*, 2017, **46**, 4417–4449.

66 C. R. Martinez and B. L. Iverson, *Chem. Sci.*, 2012, **3**, 2191–2201.

67 M. Nishio, *Phys. Chem. Chem. Phys.*, 2011, **13**, 13873–13900.

68 M. Giese, M. Albrecht and K. Rissanen, *Chem. Commun.*, 2016, **52**, 1778–1795.

69 M. A. Halcrow, *Chem. Soc. Rev.*, 2011, **40**, 4119–4142.

70 D. Braga, F. Grepioni and G. R. Desiraju, *Chem. Rev.*, 1998, **98**, 1375–1405.

71 M. Nishio, Y. Umezawa, J. Fantini, M. S. Weiss and P. Chakrabarti, *Phys. Chem. Chem. Phys.*, 2014, **16**, 12648–12683.

72 S. Kyatskaya, J. R. G. Mascarós, L. Bogani, F. Hennrich, M. Kappes, W. Wernsdorfer and M. Ruben, *J. Am. Chem. Soc.*, 2009, **131**, 15143–15151.

73 C. M. Niemeyer, *Mater. Sci.*, 2001, **40**, 4128–4158.

74 R. J. Holmberg and M. Murugesu, *J. Mater. Chem. C*, 2015, **3**, 11986–11998.

75 M. Mannini, F. Pineider, C. Danieli, F. Totti, L. Sorace, P. Sainctavit, M. A. Arrio, E. Otero, L. Joly, J. C. Cezar, A. Cornia and R. Sessoli, *Nature*, 2010, **468**, 417–421.

76 V. E. Campbell, M. Tonelli, I. Cimatti, J. B. Moussy, L. Tortech, Y. J. Dappe, E. Rivière, R. Guillot, S. Delprat, R. Mattana, P. Seneor, P. Ohresser, F. Choueikani, E. Otero, F. Koprowiak, V. G. Chilkuri, N. Suaud, N. Guihéry, A. Galtayries, F. Miserque, M. A. Arrio, P. Sainctavit and T. Mallah, *Nat. Commun.*, 2016, **7**, 13646.

77 M. Del Carmen Giménez-López, F. Moro, A. La Torre, C. J. Gómez-García, P. D. Brown, J. Van Slageren and A. N. Khlobystov, *Nat. Commun.*, 2011, **2**, 407.

78 M. A. Halcrow, *Coord. Chem. Rev.*, 2005, **249**, 2880–2908.

79 G. Aromí, L. A. Barrios, O. Roubeau and P. Gamez, *Coord. Chem. Rev.*, 2011, **255**, 485–546.

80 J. Ferrando-Soria, J. Vallejo, M. Castellano, J. Martínez-Lillo, E. Pardo, J. Cano, I. Castro, F. Lloret, R. Ruiz-García and M. Julve, *Coord. Chem. Rev.*, 2017, **339**, 17–103.

81 C. M. Quintero, G. Félix, I. Suleimanov, J. S. Costa, G. Molnár, L. Salmon, W. Nicolazzi and A. Bousseksou, *Beilstein J. Nanotechnol.*, 2014, **5**, 2230–2239.

82 M. Gobbi, M. A. Novak and E. Del Barco, *J. Appl. Phys.*, 2019, **125**, 9–12.

83 E. Coronado, *Nat. Rev. Mater.*, 2020, **5**, 87–104.

84 H. Hagiwara, R. Minoura, T. Udagawa, K. Mibu and J. Okabayashi, *Inorg. Chem.*, 2020, **59**, 9866–9880.

85 S. A. Barrett and M. A. Halcrow, *RSC Adv.*, 2014, **4**, 11240–11243.

86 K. H. Sugiyarto and H. A. Goodwin, *Aust. J. Chem.*, 1988, **41**, 1645–1663.

87 M. A. Halcrow, *Coord. Chem. Rev.*, 2009, **253**, 2493–2514.

88 L. J. Kershaw Cook, R. Mohammed, G. Sherborne, T. D. Roberts, S. Alvarez and M. A. Halcrow, *Coord. Chem. Rev.*, 2015, **289**–**290**, 2–12.

89 J. Y. Li, Y. C. Chen, Z. M. Zhang, W. Liu, Z. P. Ni and M. L. Tong, *Chem. - A Eur. J.*, 2015, **21**, 1645–1651.

90 L. J. Kershaw Cook, R. Kulmaczewski, R. Mohammed, S. Dudley, S. A. Barrett, M. A. Little, R. J. Deeth and M. A. Halcrow, *Angew. Chemie - Int. Ed.*, 2016, **55**, 4327–4331.

91 M. A. Halcrow, *Crystals*, 2016, **6**, 58.

92 M. del C. Giménez-López, M. Clemente-León and C. Giménez-Saiz, *Dalt. Trans.*, 2018, **47**, 10453–10462.

93 V. Jornet-Mollá, Y. Duan, C. Giménez-Saiz, J. C. Waerenborgh and F. M. Romero, *Dalt. Trans.*, 2016, **45**, 17918–17928.

94 E. Coronado, M. del Carmen Gimenez-Lopez, C. Giménez-Saiz and F. M. Romero, *CrystEngComm*, 2009, **11**, 2198–2203.

Chapter 2

In Situ Electrochemical Switching of PdS_x in Carbon Nanofibers as HER Electrocatalysts

2.1 Abstract

Electrocatalysts for HER have been extensively studied, Pt and Pd like metals supported on carbon being the most effective in this area. Electrocatalysts tend to be single use, in this paper a new PdS_x nanoparticle with PtS like structure anchored to milled carbon nanofibers (CNF_m) is introduced as a highly efficient and switchable electrocatalyst. The active catalyst is accessed through electrochemical cycling and possesses all the hallmarks of an excellent catalyst. The catalyst shows exceptional onset potential when compared with commercial and benchmark Pt/C, an overpotential of 21mV @10mA/cm^2 and a far superior Tafel slope of ~14mV/dec. The synergistic behaviour during positive and negative potential cycling allows us to repeatedly regenerate the active species which are consumed during exposure to negative potentials where other catalysts would simply need to be replaced.

2.2 Introduction

There is an ongoing battle to combat climate change and reduce carbon emissions globally. In order to truly impact carbon emissions alternative fuels and energy storage must come into effect, one major route to this is the implementation of the hydrogen economy. Due to the low natural abundance of molecular hydrogen it is unable to fulfil global demands, and it is necessary to synthesise hydrogen. Currently the main hydrogen production method is steam reformation of fossil fuel sources which has carbon dioxide as a by-product. The use of renewable energy to produce hydrogen is the first and main hurdle to the implementation of a clean hydrogen economy.[1] Implementing an energy-hydrogen-energy system has been the subject of many academic reviews and is part of a politically backed global push to be carbon neutral by 2050.[2] Consensus within the literature is that the hydrogen economy will be most effectively implemented as a complete overhaul but in conjunction with other technologies

in varying sectors in order to meet energy needs with the smoothest integration into existing systems.[3]

Decreasing prices in renewable electricity technologies including wind and solar cells has brought their use in conjunction with electrolysers to an economically viable level.[4] These sources can then be used to generate hydrogen by electrolysis of water to be stored and used as fuel at a later date with no emission of CO_2.[2]

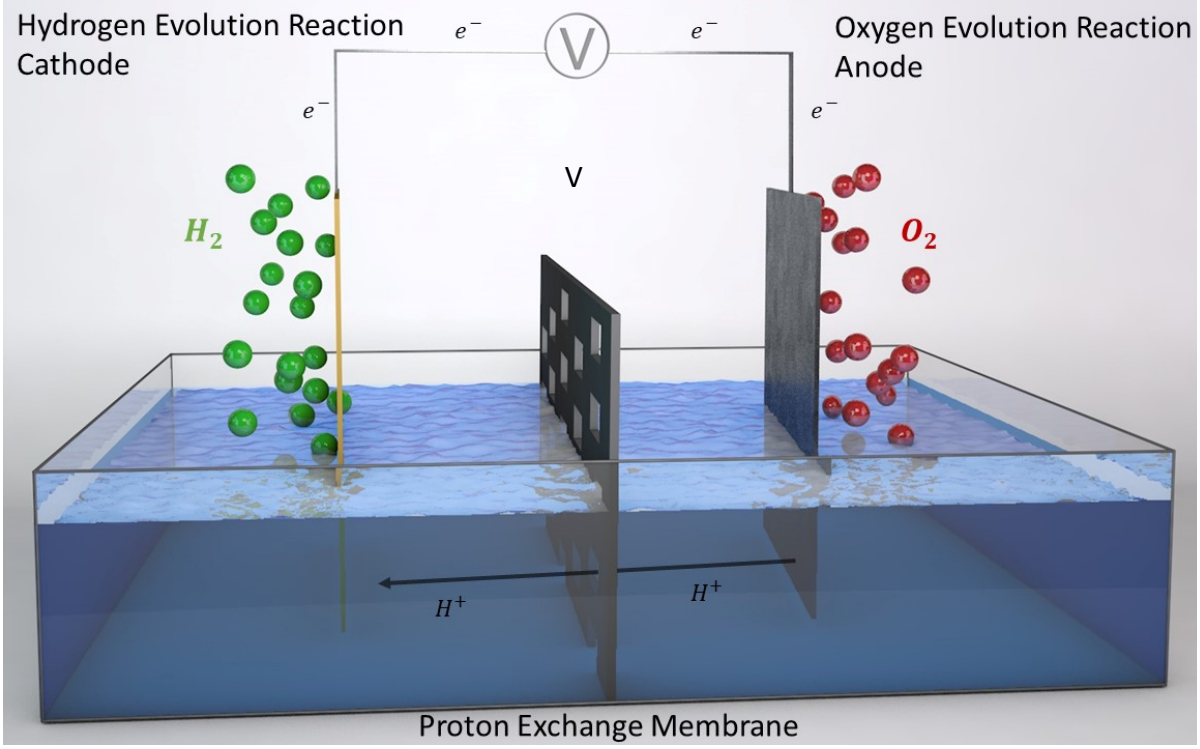

Scheme 2. 1 *Proton exchange membrane water splitting electrolyser. Cathodic HER* $2H^+ + 2e^- = H_2$ *and anodic OER* $H_2O = 2H^+ + \frac{1}{2}O_2 + 2e^-$ *in acidic electrolyte.*

The electrochemical water splitting reaction shown in **Scheme 2. 1** involves the oxygen evolution reaction (OER) at the anode and the hydrogen evolution reaction (HER) at the cathode.

Cathode	$2H^+ + 2e^- = H_2$	$E_c^\theta = 0.0\ V$	vs RHE
Anode	$H_2O = 2H^+ + \frac{1}{2}O_2 + 2e^-$	$E_a^\theta = 1.23\ V$	vs RHE

Total reaction $H_2O = H_2 + \frac{1}{2}O_2$ $E^{\theta}_{Cell} = 1.23\ V$ vs RHE

This work concentrates on electrocatalysts for the cathodic HER in acidic conditions for which Pt is the benchmark due to its favourable binding energy for protons.[5] With improving technologies and the potential implementation of these technologies throughout the world, Pt becomes a significant road block for widespread implementation due to its high cost. Thus efforts to improve on Pt and overcome its high cost have seen the development of a huge array of different catalysts from alloys to nanoparticles with extended 1D, 2D and 3D structures which have been widely reviewed and discussed in the literature.[6]

Pd has been considered an alternative to Pt due to its similar proton adsorption energy and has thus been significantly investigated and reviewed.[7] The behaviour of palladium nanoparticles, alloys and composites have been well documented allowing work in this area to continue with various substrates and morphologies being developed and characterised. Due to the high cost of Pt and Pd significant research into improving catalytic activity and reducing metal loading is ongoing alongside the search for new materials as hydrogen evolution catalysts. This research lead to the computational discovery of MoS_2 as an ideal candidate[8]. The elucidation of the active sites of MoS_2 as the sulfur-rich edge sites gave rise to an increased study of the effects of the support material on the HER.[8,9] Examples of metal chalcogenides as HER catalyst can be found due to the success of MoS_2 which has inspired significant investigations into catalyst-support studies and site-specific investigation to determine and improve activity within MoS_2. Transition metal chalcogenides have also been reviewed these include PtS_2 and $PdSe_2$.[10,11]

PdS as nanocorals have previously been investigated as a catalyst and light absorber for water splitting due to its favourable band gap, however this data shows it does not compete

electrochemically with metallic Pd or Pt. [12] Metal chalcogenides have received a great deal of interest and these investigation along with the wealth of information on Pd as a catalyst for HER have lead the Gimenez-Lopez group to develop novel PdS_x nanoparticles.[7,10–15]

The choice of catalyst support is very significant for developing a catalyst, carbon is an excellent support with a great deal of investigation in to its use as it enables the reduction of precious metal loading and increases conductivity of chemically active but electrically insulating materials. Moreover, carbon is essentially inactive towards the HER at low overpotentials and stable to negative potentials in acidic conditions. Investigations of heteroatom-doped carbon show improved intrinsic activity towards the HER due to heteroatoms acting as preferential binding sites.[16–18] Amorphous carbons are used as supports for Pt due to their ability to withstand acidic conditions both oxidising and reducing. Carbon nanotubes (CNTs) both single and multiwalled along with graphene have also been employed, less explored are graphitised carbon nanofibers (CNFs).[19] These materials have corrugated internal structures which have been shown to stabilise metal nanoparticles to agglomeration and allow solvent to access these sites for reactions to occur. Due to this encapsulation effect and high degree of graphitisation they are an ideal candidate to stabilise and improve catalytic materials.[20,21]

Examples of electrochemically activated materials or *in operando* activated materials are few and far between. Studies on the use of Pt counter electrodes and the number of CV cycles necessary to activate carbon materials which is around 13000 CV at -0.56 to 0.24V at 50mV/s determined that these conditions were dissolving and depositing Pt from the counter electrode as NPs on the carbon substrate.[22] Electrochemical activation of $MoTe_2$ occurs during negative chronoamperometric experiments.[23] A similar phenomenon also occurs for Pt

dichalcogenides pre-treated at reductive potentials. These materials observe a 50% reduction in overpotential.[13]

In this work we focused on the synthesis of a novel hybrid palladium sulfide nanoparticle (PdS_x) confined within carbon nanofibers and for the first time showed by extensive investigation of its in-situ electrochemical activation towards the HER, an alternative to commercial Pt/C. The new PdS_x NP were characterised through a number of spectroscopies and x-ray diffraction confirming their structure. The PdS_x@CNF_m composite was electrochemically activated with a wide window cycling regime. The activated material was confirmed to compete with Pt/C in all common electrocatalyst parameters and was then tested by various electrochemical methods including chronoamperometry and cyclic voltammetry to elucidate the synergistic route to activation final active species.

2.3 Experimental

2.3.1 Synthesis of milled carbon nanofibers (CNF_m).

Milled carbon nanofibers (CNF_m) were produced by mechanical ball milling using a Retsch MM400 ball mill instrument (600 rpm). In a typical experiment, 50 mg of CNF (Pyrograh, PR24) were placed into a stainless-steel container (5mL) with a stainless-steel ball (10 mm diameter) and milled in air for 180 min at 600 rpm (98% yield). No further purifications steps were required.

2.3.2 Synthesis of preformed palladium nanoparticles (PdNP).

The synthesis of dodecanethiolate-stabilised PdNPs was performed using a modified Brust–Schiffrin protocol. To an aqueous solution of the metal salt (0.2 mmol, K_2PdCl_4) in deionised water (30 mL) was added a solution containing tetraoctylammonium bromide (0.4 mmol, 223

mg) in toluene (60 mL) and the mixture was vigorously stirred at room temperature for 10 min. To this mixture was added a solution containing dodecanethiol (0.2 mmol, 50 µL) in toluene (10 mL) and the mixture was vigorously stirred at room temperature for 10 min. To the reaction mixture was added a further solution containing sodium borohydride (2.0 mmol, 75.6 mg) in deionised water (30 mL) and the resulting black mixture was vigorously stirred at room temperature for 20 hours. The biphasic mixture was then separated, retaining the organic layer which was washed with water (3 x 100 mL) and dried over anhydrous sodium sulfate. This was concentrated (*c.a.* 5 mL) under vacuum and the product precipitated from solution by addition of ethanol (350 mL) and storing at -30˚C for 24 hours. The resulting precipitate was filtered through a 0.2 µm pore size PTFE membrane, the solid washed with ethanol (200 mL), acetone (200 mL) and finally dried under vacuum to yield a brown solid product (56.7 mg PdNP).

2.3.3 Synthesis of preformed PdNP encapsulated CNF_m composites (PdNP@CNF_m)

Initially, CNF_m (10 mg) were dispersed in hexane (10 mL) by 10 minutes sonication and added dropwise to a stirring suspension of PdNPs (20mg) in hexane. The resulted dark suspension was sonicated for 15 min. Subsequently, it was filtered through a 0.2 µm pore size PTFE membrane, the solid washed with hexane (200 mL), acetone (200 mL) and finally dried under vacuum.

2.3.4 Synthesis of PdS_x composites in vacuum.

Solid composites (10 mg, PdNP@CNF_m) were sealed under vacuum (10^{-5} mbar) in a Pyrex tube to be subsequently placed in a pre-heated oven (300^{o}C) for 2 hours. Once the material cooled down, the heated PdS_x@CNF_m composite was sonicated for 15 minutes in hexane (50mL) and

filtered through a 0.2 µm pore size PTFE membrane. The solid was washed with hexane (100 mL), acetone (200 mL) and finally dried under vacuum.

2.3.5 Material characterization

High resolution transmission electron microscopy (HRTEM) was performed on a JEOL JEM F200 microscope equipped with a cold field-emission gun (Cold-FEG) operated at 200 kV with an ultra-high-resolution pole piece. TEM images were acquired using a Gatan OneView camera. Energy Dispersive X-ray Spectroscopy (EDS) was performed with a Centurio Large Angle Silicon Drift Detector (SDD) that collects X-rays from a detection area of 100 mm^2. TEM specimens were prepared by casting several drops of a suspension of the carbon material in hexane onto a nickel or copper-grid mounted "holey" carbon film before drying under a stream of nitrogen. TGA was carried out on an SDT Q-600 TA instrument over the range of 25-1000 °C in air with a scan rate of 5 °C/min. The Raman spectra were performed with RENISHAW Raman microscope with laser Ion Ar (514 nm). Powder XRD patterns were recorded using a PANalytical diffractometer equipped with Cu Kα source (λ=1.5418Å). The data was analysed and processed using the X' Pert Data software package. XPS measurements were recorded using a Kratos with monochromated Al Kα radiation (10 kV anode potential, 15 A emission current) in fixed analyser transmission mode (80 eV pass energy).

2.3.6 Electrochemical measurements

Electrochemical experiments were carried out on a computer-controlled potentiostat (Autolab 302N) at room temperature using a conventional three-electrode cell with 0.1M $HClO_4$ aqueous solution as electrolyte. A Pt wire and a HydroFlex platinum-hydrogen reference electrode (RHE) were used as the counter and reference electrode, respectively.

Meaning that no potential corrections are required. All the electrochemical measurements were corrected by the ohmic potential drop (iR) losses from the solution resistance, this was done by taking an average of the first 10 frequency measurements in the EIS spectra. Characteristic cyclic voltammetry (CV) measurements were taken between 0 and 1V at a scan rate of 10mV/s, linear sweep voltammetry (LSV) for hydrogen evolution was performed between 0.2V and -0.9V vs RHE at a scan rate of 10mV/s. In situ activation CVs were performed with and upper and lower potential of 1.2V and -1V vs RHE respectively starting at an applied potential of 0V at a scan rate of 10 and 50mV/s. For the chronoamperometry activation (pulsing activation), 1300 cycles were carried out by alternating the potential for 1s between -0.9V and 1.2V vs RHE, respectively.

2.4 Results and Discussion

2.4.1 Preparation and characterisation of preformed Pd nanoparticles (PdNP)

The synthesis of palladium sulfide nanoparticles encapsulated into milled carbon nanofiber (PdS_x@CNF_m) was carried out following a three-step experimental procedure (**Scheme 2. 2**). It was reported that the Brust-Schiffrin protocol enables the formation of very small and spherical low crystalline nanoparticles protected by an organic monolayer as well as controlling the morphology of nanoparticles by adjusting the metal/surfactant ratio.[24] Firstly, preformed palladium nanoparticles were synthesized via a modified Brust–Schiffrin protocol, which were stabilised by dodecanethiol (PdNP) (**Figure 2. 1**).[24]

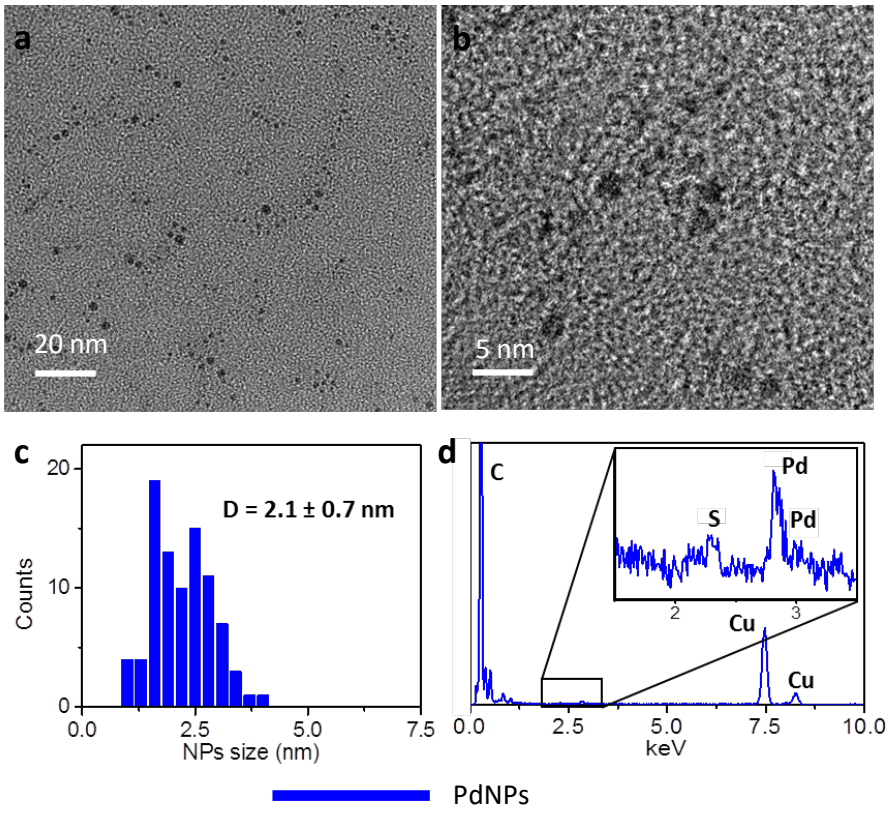

Figure 2. 1 (a-b) *HRTEM images,* ***(c)*** *size distribution (D) measured by HRTEM (more than 80 NPs) with an average diameter (D) of 2.1 ± 0.7 nm, and* ***(d)*** *EDX of preformed PdNP. Scale bars are 20 and 5 nm, respectively.*

The resultant material was imaged by HRTEM confirming the formation of very small and similar size of nanoparticles with an average diameter of 2.1 ± 0.7 nm which was consistent with the literature (**Figure 2. 1a-c**).[24] EDX confirmed the atomic composition of dodecanethiolate-stabilised PdNPs (**Figure 2. 1d**). Preformed nanoparticles were further analysed by powder XRD and a broadening of the XRD peak was observed due to the presence of very small nanoparticles in size (**Figure 2. 2a**). IR and Raman analysis were used to investigate the chemical structure of preformed nanoparticles. IR confirmed the presence of dodecanethiol interacting with palladium corresponding to a peak at 720 cm^{-1} which was related to rocking vibrational mode (long alkyl chain, $-C_{12}H_{25}$) while Raman measurement indicated peaks at 328, 1080 and 2888 cm^{-1} corresponding to the Pd-S vibration, C-C stretching and C-H stretching, respectively (**Figure 2. 2b and c**).[16-17]

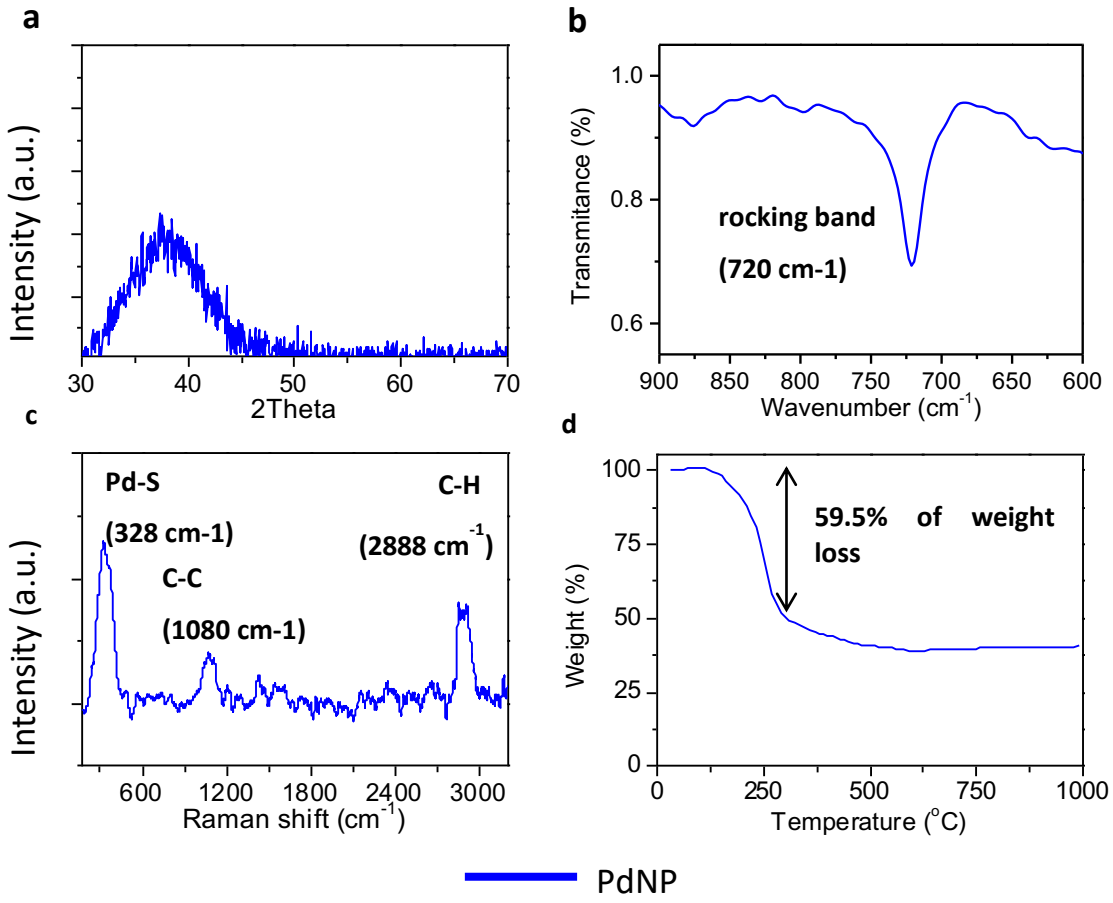

Figure 2. 2 (a) *Powder XRD* ***(b)*** *IR spectra* ***(c)*** *Raman spectra and,* ***(d)*** *TGA measurements of preformed PdNP. TGA of preformed palladium nanoparticles was performed in air with a heating rate of 5 °C/min.*

Thermal gravimetric analysis (TGA) in air of preformed Pd nanoparticles shows a weight loss of 59.5% at 250˚C and 40.5% of Pd loading by weight (**Figure 4d**). It was revealed that our preformed palladium nanoparticles had more surfactant (almost twice) than that of other metal nanoparticles synthesised by the same protocol (**Figure S 1**).[24] The high sulfur content observed in these nanoparticles are in line with studies of palladium with dodecanethiol. For example, previous studies on the preparation of self-assembled monolayer of thiolate on several metals such as Pd, Au, Cu, Ag and Pt reported that the Pd surface has more affinity to adsorb the larger amounts of S than other metals.[26–28] In the preparation method, palladium has the ability to promote a radical dissociative chemisorption process of adsorbed thiolates

leading to the cleavage of the C-S bond and a successive formation of a Pd-S layer underneath the thiolate monolayer and Pd sulfide nanoparticles with Pd (+2) states instead of Pd (0).

Preformed nanoparticles (PdNPs) were then deposited on a Pyrex® glass container, sealed under vacuum, and heated at a temperature of 300˚C to remove the surfactant and leave sulfur, leading to PdS_x nanoparticles. Powder XRD of preformed and annealed PdS_x nanoparticles was investigated and compared with Pd and PdS references (**Figure 2. 3**). However, the patterns of this material did not match with these references. We found that the PdS_x nanoparticles after thermal treatment show a similar XRD pattern to PtS with peaks at 2θ = 30, 36 and 46. Despite the fact that Pd and S retaining their square planar and tetrahedral coordination both in PdS and PtS, the former is less symmetric and denser structure with half as many channels (**Figure 2. 4**). Rozhdestvinaa and co-workers have recently investigated that sulfur vacancies in the crystal structure are more stable in PtS than PdS solid state structure and density functional theory calculations performed by Marmier and co-workers have identified that the PtS is more stable than the PdS structure.[29,30] Hence, it can be proposed that sulfur vacancies in preformed PdS_x nanoparticles (as suggested by the low S/Pd ratio) would favour the packing of the atoms to have a PtS-like structure. Note that although it would be of great interest to fully understand the formation of PtS-like structure and its relation with the S/Pd ratio as well as the identification of vacancy-ordered phases, it is out of the scope of this paper as it would require neutron powder diffraction measurements and Rietveld refinements. To the extent of our knowledge, palladium sulfide nanoparticle with a PtS-like structure have not been investigated previously and they show great potential towards electrochemical applications.[10,31]

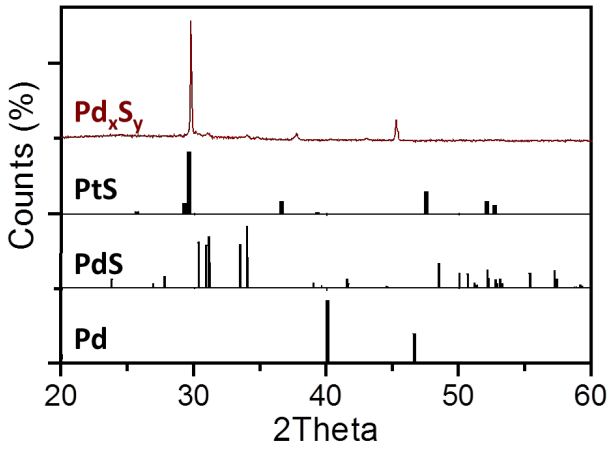

Figure 2. 3 *Powder XRD patterns of thermally treated PdS_x nanoparticles at 300°C for 2 hours under vacuum (brown, top) with PtS[32], PdS[33] and Pd(0)[34] references, respectively.*

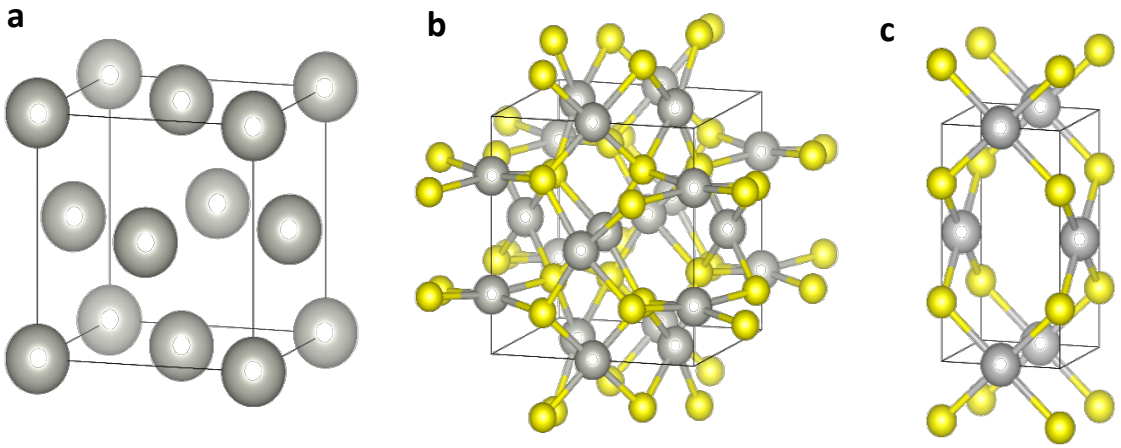

Figure 2. 4 *Crystal structure models of **(a)** Pd(0) JCPDS No. 89-4897 [35], **(b)** PdS JCPDS No. 25-1234[35] , and **(c)** PtS JCPDS No. 18-0972[35]*

2.4.2 Combining preformed PdS_x nanoparticles with carbon nanofibers

An experimental procedure was developed to combine preformed Pd nanoparticles with CNF. (**Scheme 2. 1**).

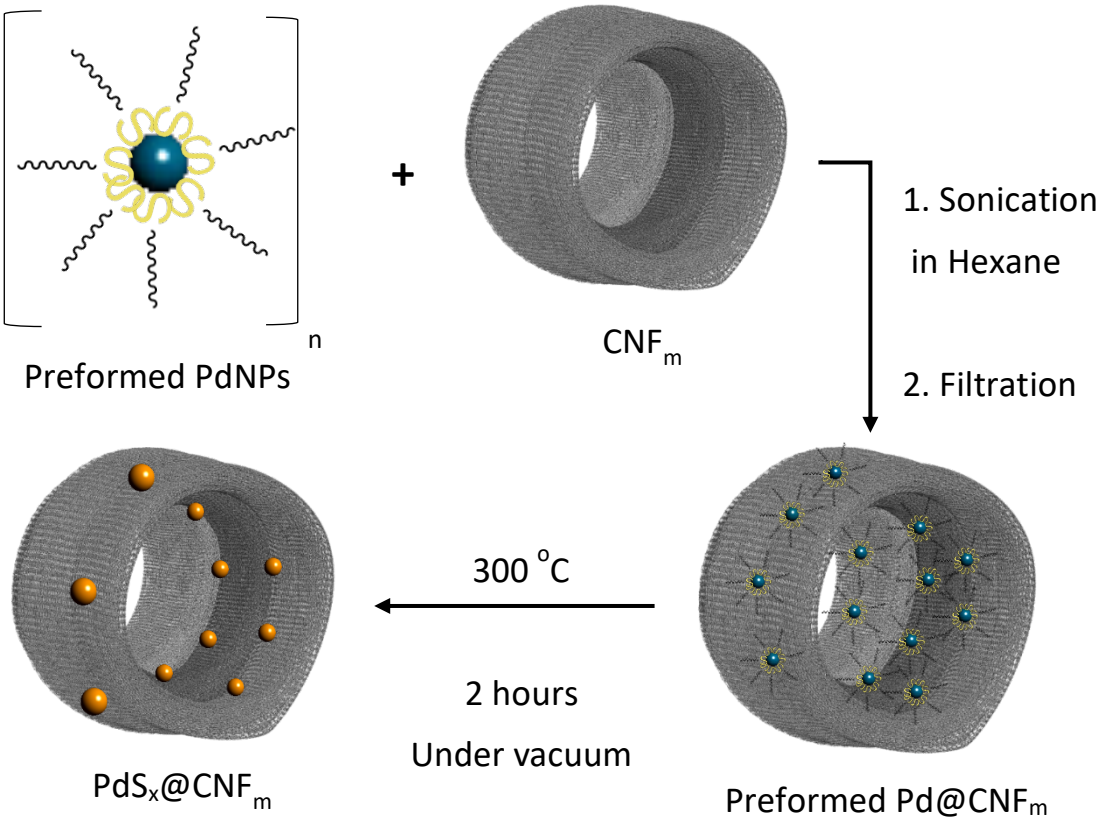

Scheme 2. 2 *Schematic representation of the synthesis protocol of PdS_x nanoparticles within CNF_m ($PdS_x@CNF_m$).*

CNF was also ball-milled prior to combination with preformed PdNPs to reduce the length dependence on the mass transport resistance and improve film preparation for electrochemical applications. HRTEM confirmed the significantly shortened CNF (CNF_m) (**Figure 2. 5a**) in length (2.4 ± 1.9 µm) (**Figure 2. 5d**) by ball milling, while maintaining the integrity of the folded step-edges of the graphitic planes in their cavities (**Figure 2. 5b**), these fibres are pure and contain no impurities shown by EDS (**Figure 2. 5c**).

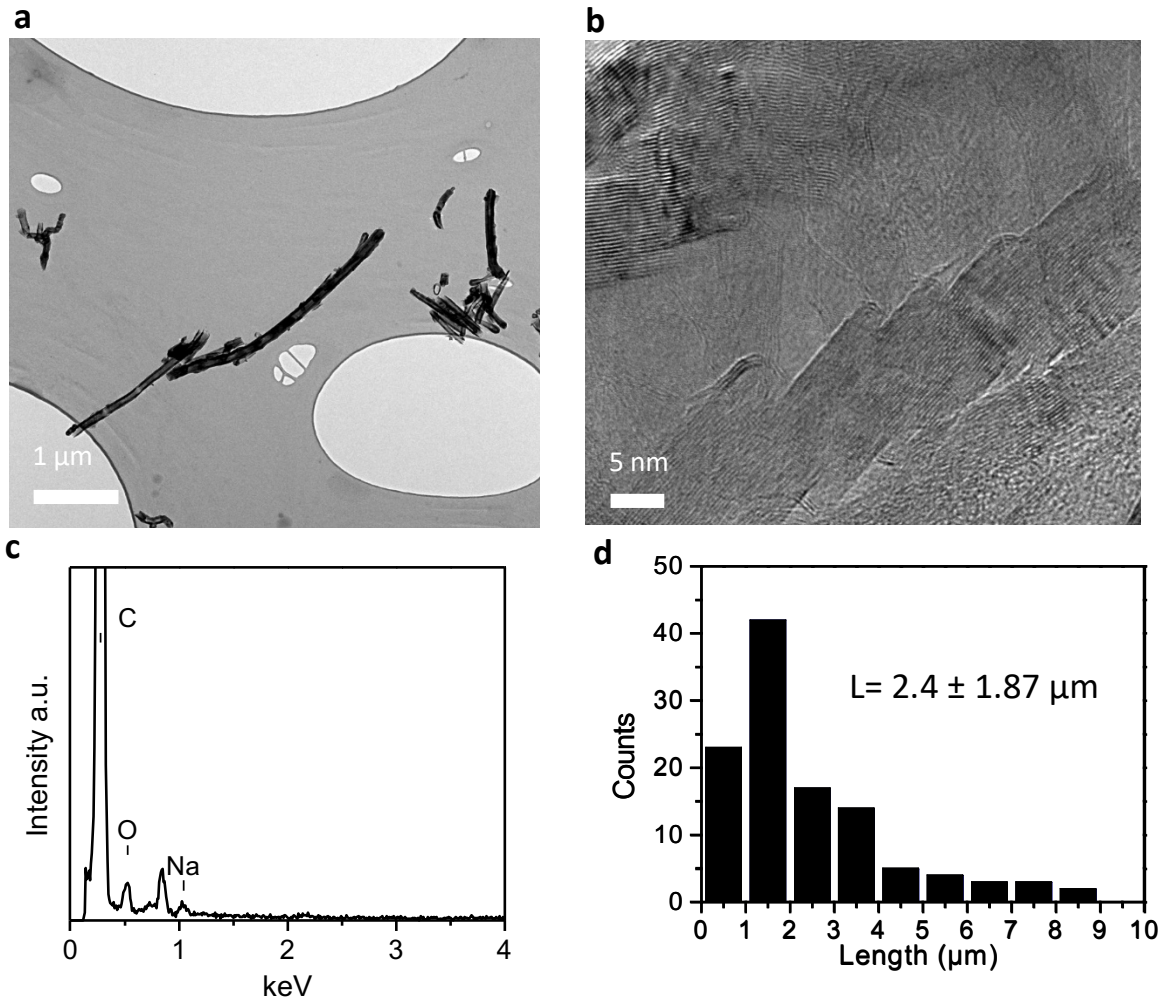

Figure 2. 5 (a-b) *HRTEM images,* ***(c)*** *EDX and* ***(d)*** *size distribution of milled carbon fibres (CNF_m) with an average length of 2.4 ± 1.9 µm measured by HRTEM*

CNF and CNF_m were then mixed with PdNPs by sonication in hexane and thermally annealed at 300 ^{0}C for 2 hours to remove the surfactant to form PdS_x@CNF and PdS_x@CNF_m, respectively (**Scheme 2**, Experimental Section).

HRTEM images confirmed the presence of homogeneously distributed PdS_x nanoparticles with a mean size of 4.2 ± 0.8 nm both inside and outside of CNF_m (**Figure 2. 6c,d,e**), the presence of Pd and S was confirmed by EDS (**Figure 2. 6f**). While there were slightly bigger nanoparticles with a mean size of 4.2 ± 0.8 nm and 10.1 ± 0.8 nm inside and outside of the long CNF, respectively (**Figure 2. 6a,b**). This is due to the presence of small structural defects on the external CNF_m surface produced during the milling treatment. The external defects of

CNF_m enabled the stabilisation of the PdS_x nanoparticles to a similar extent as the internal folded step edges (**Figure S2**) leading to uniformly distributed NPs in size both internally and externally. The external stabilisation does not occur on the outside of the long CNF due to a smoother exterior (**Figure 2. 6a**).

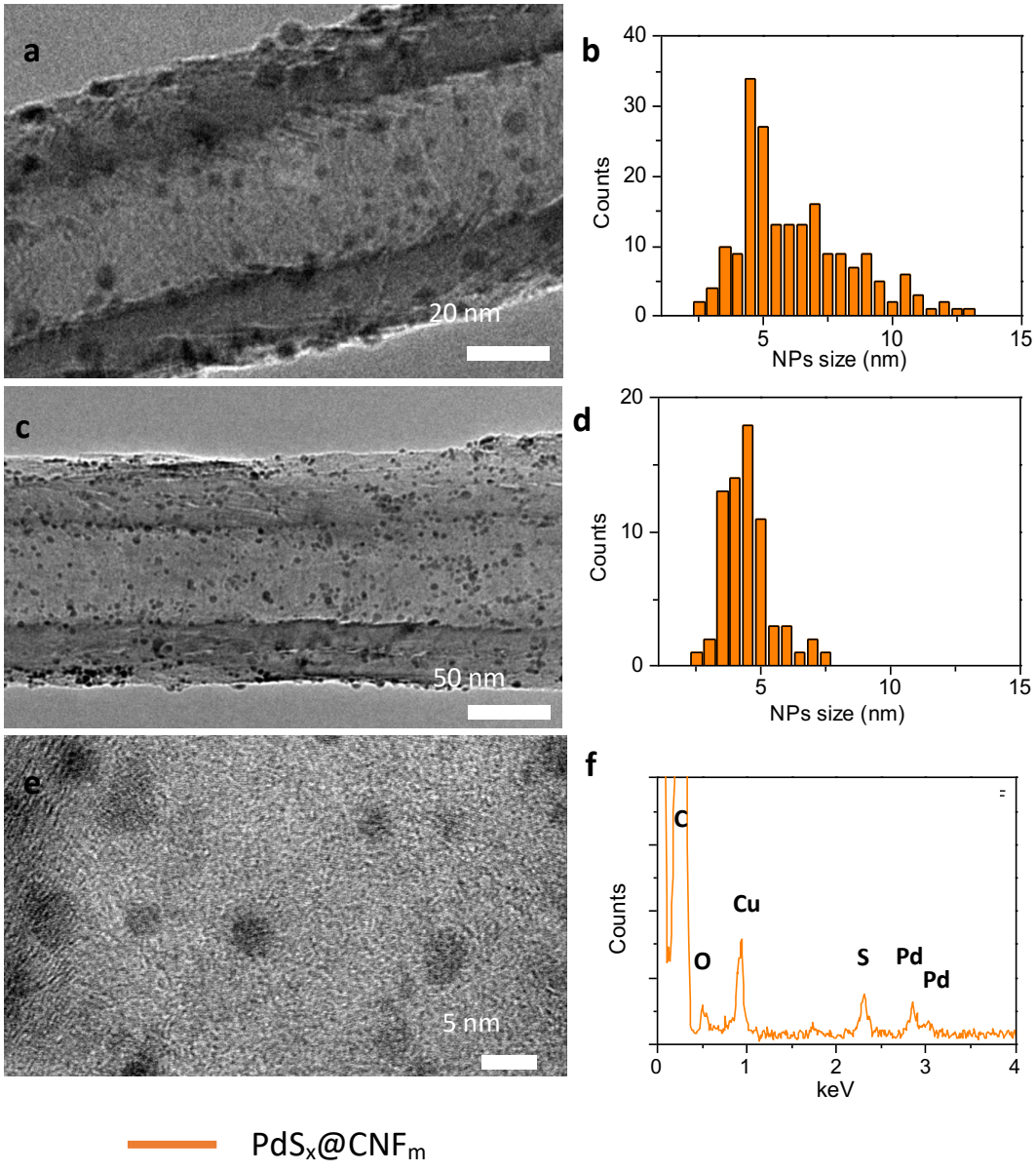

Figure 2. 6 *TEM image and statistical size distribution of* ***(a-b)*** *PdS_x@CNF and* ***(c,e)*** *PdS_x@CNF_m* ***(f)*** *EDX of PdS_x@CNF_m confirming the presence of Pd and S. Scale bars are 20, 50 and 5 nm, respectively.*

PdS_x@CNF_m were further characterised by IR and Raman spectroscopy, powder XRD and TGA. IR spectroscopy confirmed the removal of surfactant after the thermal annealing due to the

absence of the rocking vibrational mode at 720 cm^{-1} compared to preformed PdNPs (**Figure 2. 7a**). The detection of sulfur by EDS (**Figure 2. 6f**) and the small weight loss at ~250^{o}C of $PdS_x@CNF_m$ in air by TGA (**Figure 2. 7b**) support the formation of palladium sulfide. Powder XRD showed that carbon does not have an effect on the structural composition of nanoparticles during thermal treatment as a similar XRD pattern of preformed palladium sulfide nanoparticles are obtained after thermal annealing (**Figure 2. 7c**). Similarly, palladium sulfide formation is further confirmed by the presence of Pd-S bonds at ~340 cm^{-1} in both annealed preformed nanoparticles and $PdS_x@CNF_m$ by Raman spectroscopy (**Figure 2. 7d**), it is noteworthy that neither Pd-O or C-C stretching bands were observed at 650 cm^{-1} and 1080 cm^{-1} in the spectrum. $PdS_x@CNF$ was used as a control experiment in which nanoparticles were large enough to acquire more accurate data by XRD and Raman spectroscopy, the nanoparticles in $PdS_x@CNF_m$ are too small in size to detect by Raman spectroscopy and have low crystallinity **(Figure 2. 7c-d and Figure S3).**

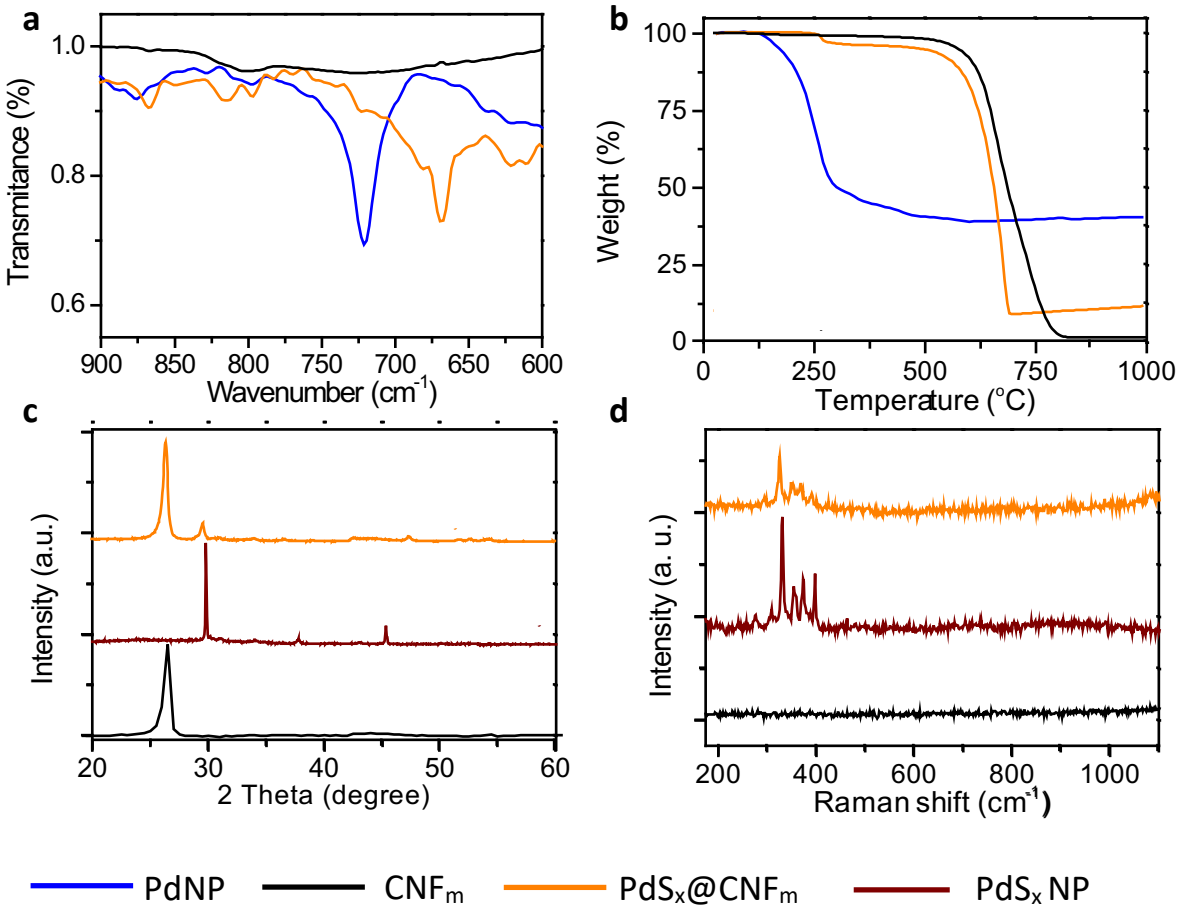

Figure 2. 7 (a) *IR,* ***(b)*** *TGA,* ***(c)*** *powder XRD, and* ***(d)*** *Raman of PdS_x@CNF (orange), PdS_x@CNF_m(orange), CNF_m (black) and thermally annealed preformed PdNPs (PdS_x NP, brown).*

X-ray photoelectron spectroscopy (XPS) was performed to further investigate the surface chemical composition of PdS_x@CNF_m, with preformed dodecanethiol-stabilised palladium nanoparticles were used as background. Wide scan XPS showed sulfur content in both samples, with a S and Pd atomic ratio (%) of 0.84 and 0.78, respectively (**Figure 2. 8a**). High resolution XPS spectra revealed the appearance of a positively charged sharp peak Pd $3d_{5/2}$ at a binding energy of 337.5 eV (**Figure 2. 8c**) and negatively charged S $2p_{3/2}$ at 162 eV (**Figure 2. 8b)** in both sample, confirming the presence of palladium sulfide.[36] Contrary to the literature, no Pd (0) was observed shown by the absence of a peak located at 335.5 eV **Figure 2. 8c**).[18] Hence, XPS confirms that palladium sulfide is present in PdS_x@CNF_m, which is in agreement with powder XRD data and TGA analysis.

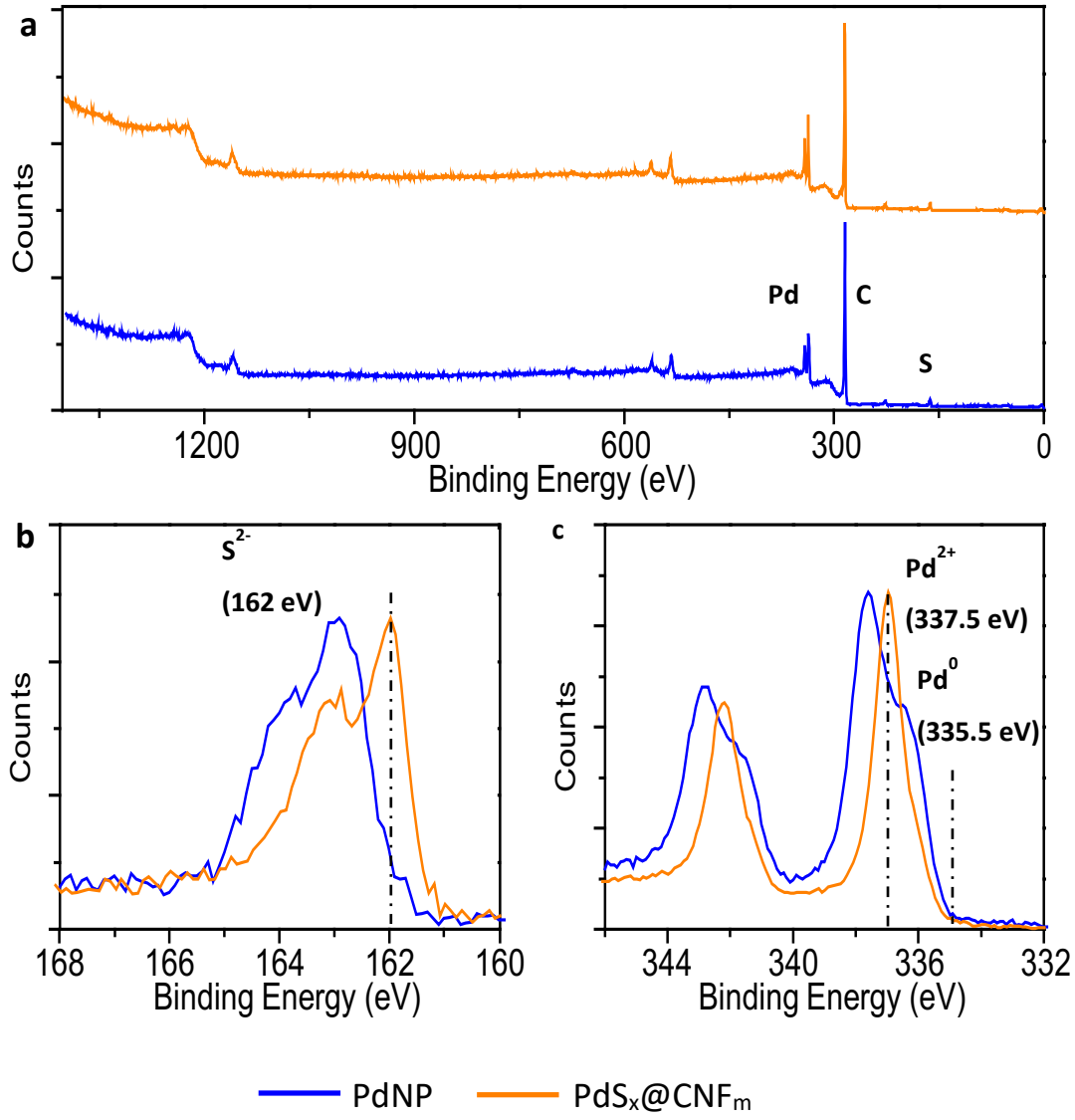

Figure 2. 8 a) *Wide scan XPS spectra and high resolution* ***(b)*** *S 2p and* ***(c)*** *Pd 3d XPS of preformed palladium nanoparticles (PdNPs) and $PdS_x@CNF_m$. Charge correction for the C 1s spectrum was set at the binding energy of 284.6 eV.*[37,38]

The atomic composition of $PdS_x@CNF_m$ was further imaged via EDX-STEM mapping techniques, showing that sulfur is located in nanoparticles both inside (**Figure 2. 9a**) and outside (**Figure 2. 9b**) carbon nanofibers.

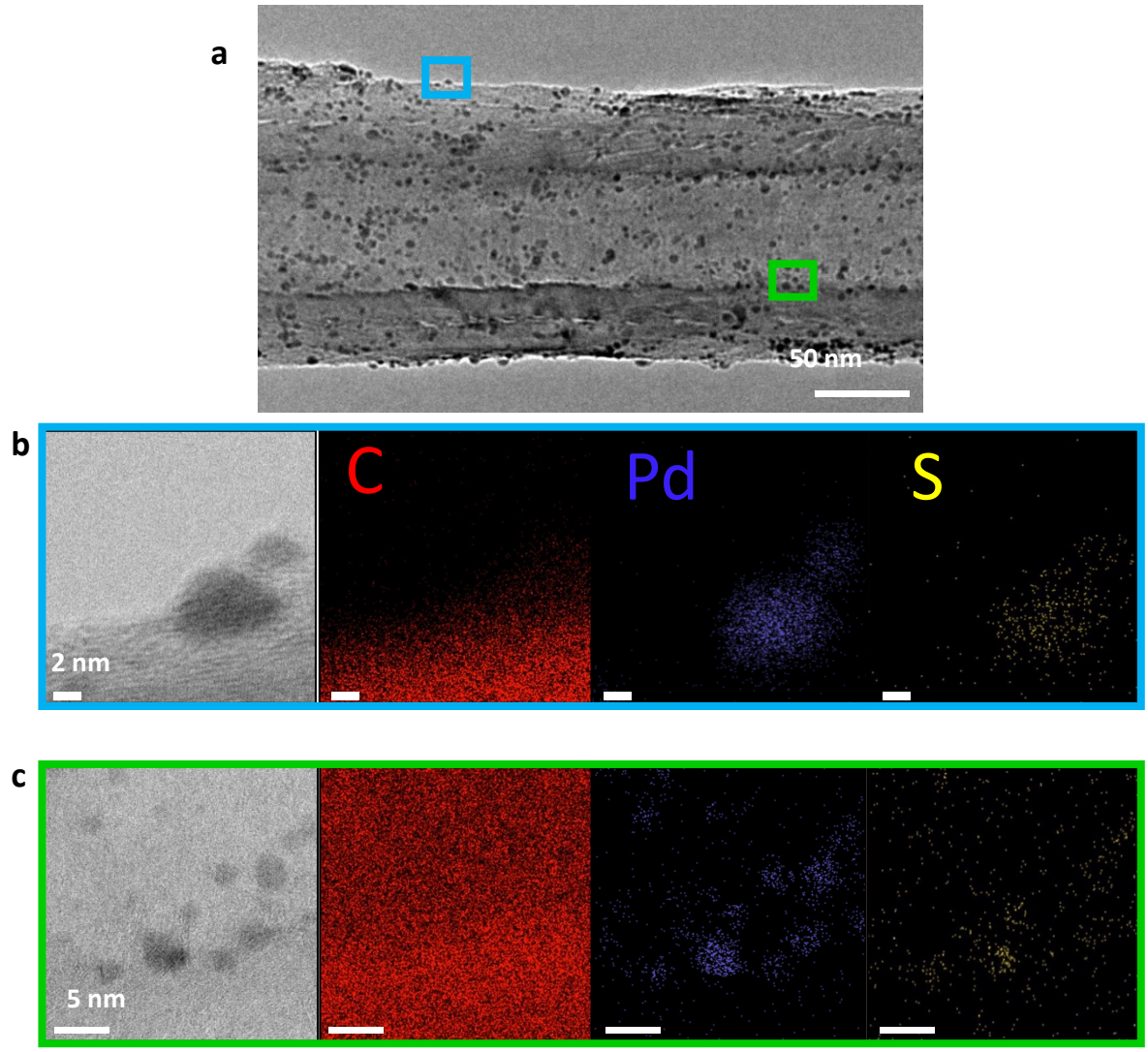

Figure 2. 9 a) *HRTEM image of PdS_x@CNF_m* ***(b,c)*** *EDS mapping of PdS_x@CNF_m showing the presence of PdS_x NPs both inside and outside CNF_m. C (red), Pd (blue) and S (yellow) atoms.*

In conclusion, we have successfully synthesized palladium sulfide nanoparticles with a PtS like structure, developed a procedure to encapsulate them within shortened carbon nanofibers and characterised with a number of combined spectroscopic analysis to be used as an electrocatalyst towards hydrogen production.

2.5 Electrochemical Investigation

The PdS_x NPs shown in the previous section exhibit a porous crystal structure after thermal treatment similar to that of PtS differentiating itself from the more dense PdS $P4_2/m$ crystal structure.[29] The reduced Pd:S ratio is proposed to give rise to sulfur vacancies similar to

natural PtS. It is possible that the PtS-like crystal structure has the potential for structural change due to vacancies and collapse to PdS $P4_2/m$ which could be induced electrochemically. Therefore, the development of novel crystalline PdS_x NPs with PtS $P4_2/mmc$-like structure presents the opportunity to investigate their surface for the HER

2.5.1 Hydrogen Evolution Reaction (HER) Activity

The electrocatalytic activity of PdS_x@CNF_m hybrid for HER was evaluated in H_2-saurated 0.1M $HClO_4$ electrolyte and compared with state-of-art Pt nanoparticles supported on carbon black (Pt/C, 20%) and Pd nanoparticles supported on activated charcoal (Pd/AC, 10%) catalyst (**Figure 2. 10a**). Each material was drop cast on a glassy carbon electrode (GCE) in the form of a hexane dispersion and investigated as a HER electrocatalyst by linear sweep voltammetry (LSV).[16] Electrocatalysts are commonly categorised by four main parameters; onset potential at which the HER starts, the overpotential required to generate 10mAcm^{-2} (η_{10}) a current which is produced by a 12.3% efficient solar cell, both of which are obtained from the LSV.[5,39,40] Additionally, information about the efficiency of the catalyst can be obtained by plotting the log of the current density *vs* the overpotential in the form of a Tafel Plot. The Tafel slope b derived from the Tafel equation (eq. 2.1) where η is the overpotential, b is the Tafel slope, j is current density and j_0 is the exchange current density. The Tafel slope indicates the increase in potential which is required to increase the current density by a factor of 10, and alongside this value the exchange current density can also be determined from the intercept which shows the inherent activity of the material.[40]

$$\eta = blog(\frac{j}{j_0}) \qquad \text{(eq. 2.1)}$$

Initial investigations of the hybrid PdS_x@CNF_m showed that the incorporation of the PdS_x NP greatly increased the activity compared with bare CNF_m (**Figure 2. 10a)**. However, they do not compete with either commercial catalysts Pt/C or Pd/AC which have superior onset potentials of approximately 0V and overpotentials at 10mAcm^{-2} are 21.5mV and 40.5mV, respectively. Electrochemical parameters for each catalyst are shown in **Error! Reference source not found.**. Moreover, the activity of the material was investigated by determining the Tafel plot which showed that PdS_x@CNF_m and CNF_m are again inferior to the commercial catalysts Pt/C and Pd/AC which show ~30 and 40 mV/dec respectively.[41,42] The high Tafel slope of the CNF_m is consistent with data from the literature.[43,44]

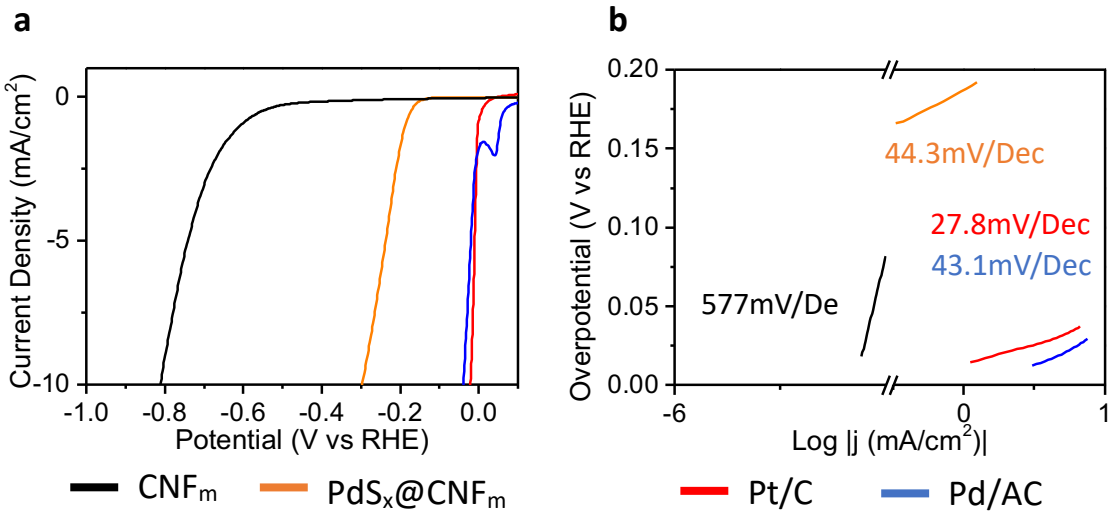

Figure 2. 10 a) *LSV for CNF_m, PdS_x@CNF_m and Pt/C commercial* ***(b)*** *Tafel plots for CNF_m, PdS_x@CNF_m, Pd/AC and Pt/C*

Table 1. 1 *Electrochemical parameters for HER catalysts PdS_x@CNF_m, Pt/C, Pd/AC and CNF_m where η@10mAcm^{-2} is the overpotential at 10 mA current. Tafel slope is the energy required to increase the activity by 10^1. Onset potential is the potential at which the HER begins, or the negative current is generated. LSV recorded at 10 mV/s in 0.1M $HClO_3$.*

	Activation scans	η@10 mAcm^{-2}	Change in η@ 10mAcm^{-2}	Tafel Slope (mV/Dec)	Onset potential (mV)
PdS_xNP@CNF_m	0	296.3	274.4	44.3	-200
	200	22.0		13.9	0
Pt/C	0	21.5	-1.8	27.8	0
	200	23.3		15.8	0
Pd/AC	0	40.5	18.8	43.1	0
	200	21.8		15.1	0
CNF_m	0	812.4	259.9	577	600
	225	552.6		172.7	400

2.5.2 Material Activation

Interestingly, continued electrochemical investigation of the same material showed an increase in the activity of the PdS_x@CNF_m with respect to the HER. Initially, common practice indicates an electrochemical surface cleaning regime from 0-1.2 V be employed for metallic electrodes normally to remove any residual surfactant from nanoparticle formation or other impurities.[45,46] For each HER LSV 50 surface cleaning CVs were performed. In this experiment the surface cleaning CVs and HER LSVs together were shown to be capable of improving the activity of the material towards the HER. Alongside these surface cleaning and HER

experiments, the material also underwent a cycling-based stability regime, scanning from 0.4 to -0.2V for cycles up to 12625 cycles **(Figure 2. 11a)**.

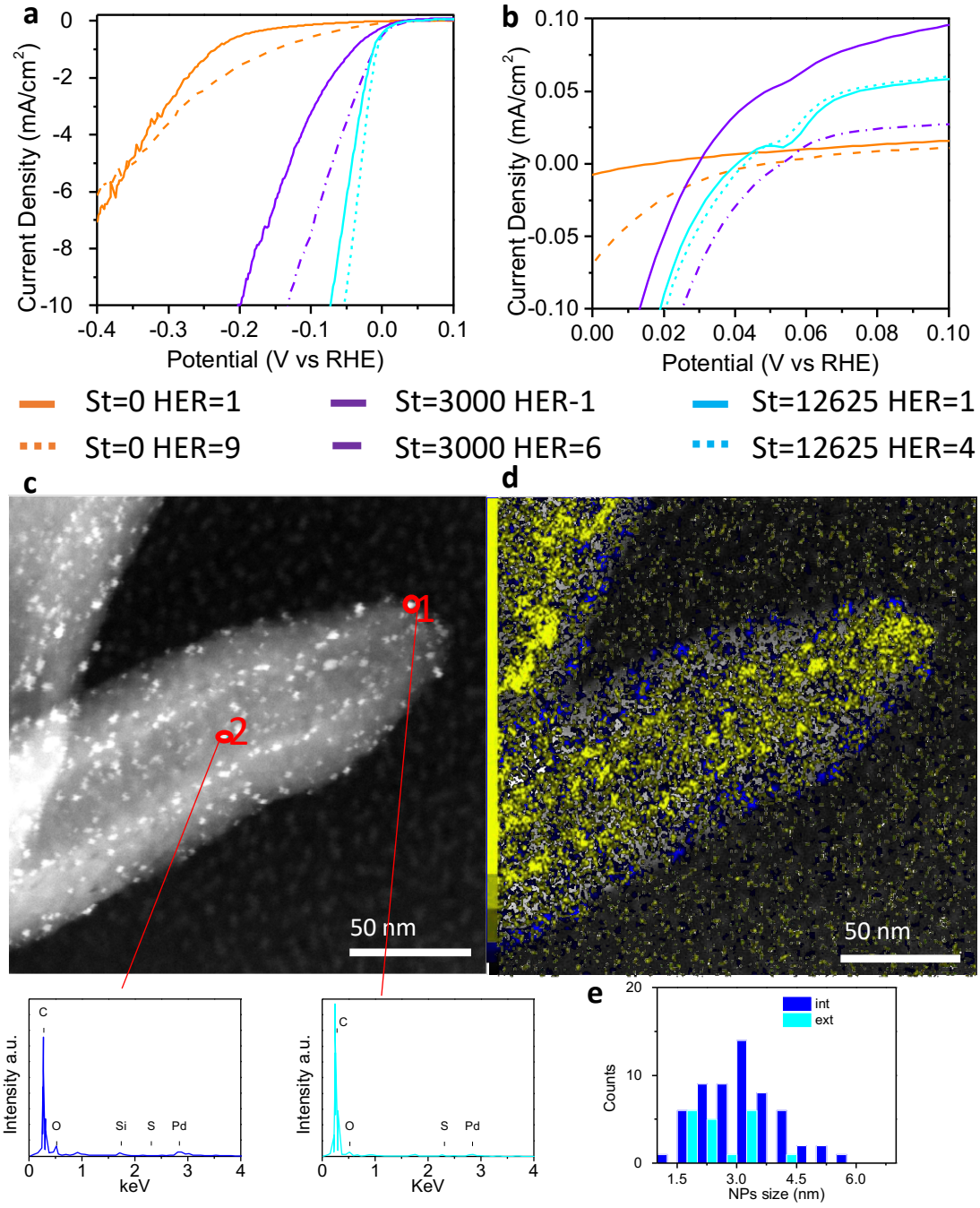

Figure 2. 11 a) *PdS_x@CNF_m LSV after Stability (St), Surface Cleaning CV and HER LSV. For St=0 HER=0 (Orange), St=0 HER=9 (Orang dash), St=3000 HER=1 (Purple), St=3000 HER=6 (Purple Dash), St=12625 HER=1 (Cyan), St=12625 HER=4 (Cyan Dash)* ***(b)*** *Magnification showing the development of the characteristic Pd proton absorption region.* ***(c-d)*** *Darkfield TEM of PdS_x@CNF_m St=12625 HER=4 and overlayed EDX mapping S (yellow) Pd (blue)* ***(e)*** *Statistical analysis for PdS_x@CNF_m after electrochemical experiment showing particle size distribution (D) of 2.1 ± 0.71 nm external and internal 3.1 ± 1.01 nm*

Figure 2. 11a shows that the LSV curves improve after subsequent application of positive potential in the form of surface cleaning and negative potential in the form of the HER LSV. The improvement can be attributed to the application of these two protocols St=3000 HER1 to HER6, but also between experiments of St=0, St=3000 and St=12625. The extensive cycling in both positive and negative potentials gives an insight into the ability of CNF_m to protect the encapsulated nanoparticles from dissolution, a discernible difference is seen between internal nanoparticles containing sulfur (yellow) and a lack of sulfur in external nanoparticles appearing as predominantly palladium (blue). A characteristic Pd proton absorption peak can be observed in a less intense form in St=3000 HER1-6 and St=12625 HER1-4 **Figure 2. 11b.** Increasing the surface area of active metal nanoparticles through controlling morphology is a common approach to increasing catalytic activity.[47,48] We propose that the PdS_x acts as a reserve of Pd and a surface at which the dissolved Pd atoms can redeposit and adhere to, thus decreasing the size of the active Pd and increasing the surface area and activity (**Figure S4**). This potentially atomic or monolayer phenomenon can only occur within the CNF_m due to confinement at the folded edge.[21,49] Externally the dissolution of Pd and S will lead firstly to the complete or near complete loss of sulfur then eventually loss of Pd. The presence of a PdS_x core in the internal nanoparticles means that the process of proton absorption and structural rearrangement, that is characteristic of Pd catalysts, no longer occurs. This means the amount of Pd present is below the detection limits of the potentiostat, the PdS_x nanoparticles likely do not possess the same response to absorption as there is no phase change associated with the absorption into the PtS-like porous structure.[50] This phenomenon increases the activity of the surface with respect to HER and allows an earlier onset compared with other palladium catalysts.[48,51] The presence of external Pd NPs and internal $Pd@PdS_x$ nanoparticles was confirmed by cycling extensively in both oxidising and reducing potentials.

The presence of internal PdS_x can be explained by confinement inside the hollow nanofibers specifically at the folded edges as the rate of dissolution of sulfur and Pd at positive potentials was reduced. This can be further attributed to the migration of the sulfur species to open edges seen in previous work, creating yet more catalytic active sites.[13,43,52,53]

It is apparent through electrochemical cycling that we are capable of altering the $PdS_x@CNF_m$ structure. The hypothesised route to activation through scanning at 50mV/s has been shown graphically in **Scheme 2. 3**. Briefly, as the potential is increased from 0 to 1.2V the material passes through oxidising potentials capable of oxidising the graphitic carbon and dissolving the Pd^{2+} shown graphically in **Scheme 2. 3a** where PdS_x surface is oxidised along with the carbon support. These processes are reversed when scanning from 1.2 to 0V redepositing the palladium metal **Scheme 2. 3b**, however edge carbons that have been oxidised will not undergo the reduction to graphitised carbon as these groups will become progressively further away from each other. From 0 to -0.9V the oxidised groups on the carbon will be reduced to hydroxyl groups or removed **Scheme 2. 3c**.[54] After cycling to 200+ cycles at 50mV/s, the material will look as hypothesised in **Scheme 2. 3d**.

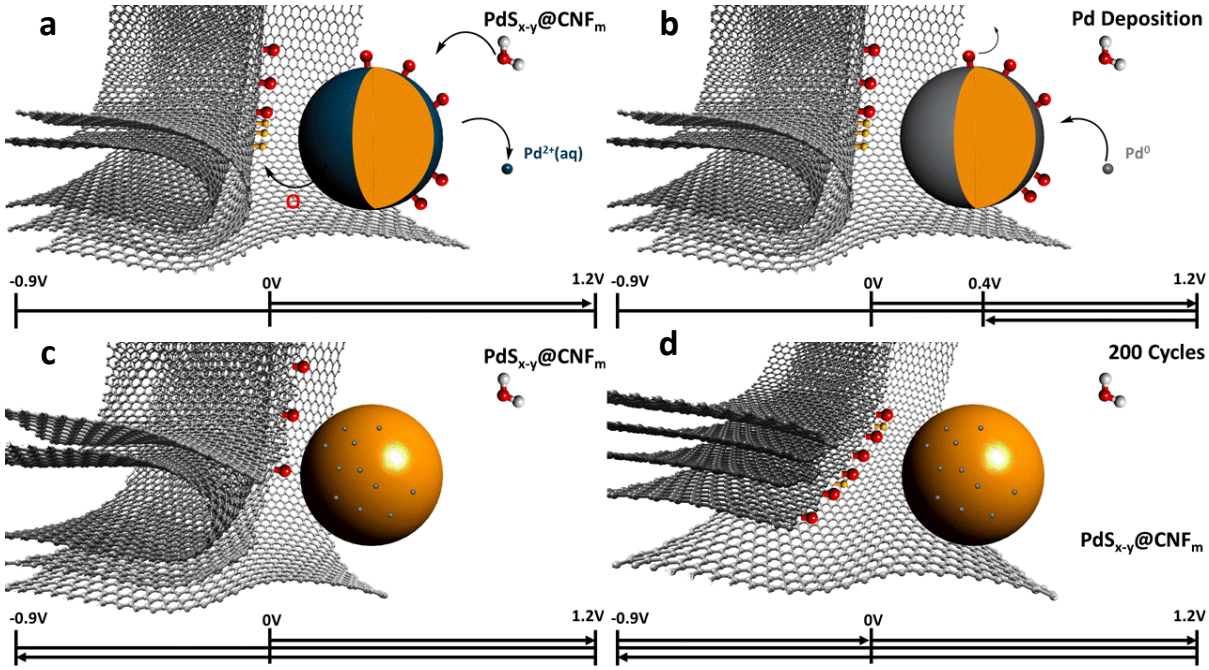

Scheme 2. 3 a-c) *shows the hypothesised progression at different potentials during one wide window scan.* ***d)*** *shows the final activated n=200* $Pd_{x-y}@CNF_m$ *material.* PdS_x *(orange),* Pd^{2+} *atoms (blue),*Pd^0 *(light grey), C (grey), O (red), S (yellow), H (white).*

2.5.3 Pulsing vs Cycling Experiments

With a new insight into alternating potentials to activate the $PdS_x@CNF_m$ we investigated several methods of obtaining alternating positive and negative potentials in order to oxidise and reduce the material. A potential range of -0.9 to 1.2V was chosen to incorporate all potentials experienced by the initial sample during the three applied experiments. Scan rates of 10mV (**Figure S5**), 50mV and pulsing (infinite scan rate) were investigated to determine any scan rate dependence. **Figure 2. 12a** shows how cycling between -0.9V and 1.2V is not scan rate dependant as both experiments reach the desired activity. However, alternating pulsing at -0.9V and 1.2V does not have the same activating effect. This is reflected by the lack of characteristic hydrogen desorption peak shown by the activated material in (**Figure 2. 12b**) Pulsing at 1s per pulse for 1300s (**Figure 2. 12a**) at each potential has the time equivalent of

cycling 12 times and 30 times for 10 (**Figure S 5**) and 50mV/s (**Figure 2. 12a**) respectively, these two intervals make it clear that time spent cycling is more important than time at the extreme potentials. (**Figure 2. 12d (iii-iv**)) shows that the internal graphitic structure after pulsing is still well intact, the pulsing experiment has not generated a material with increased HER activity.

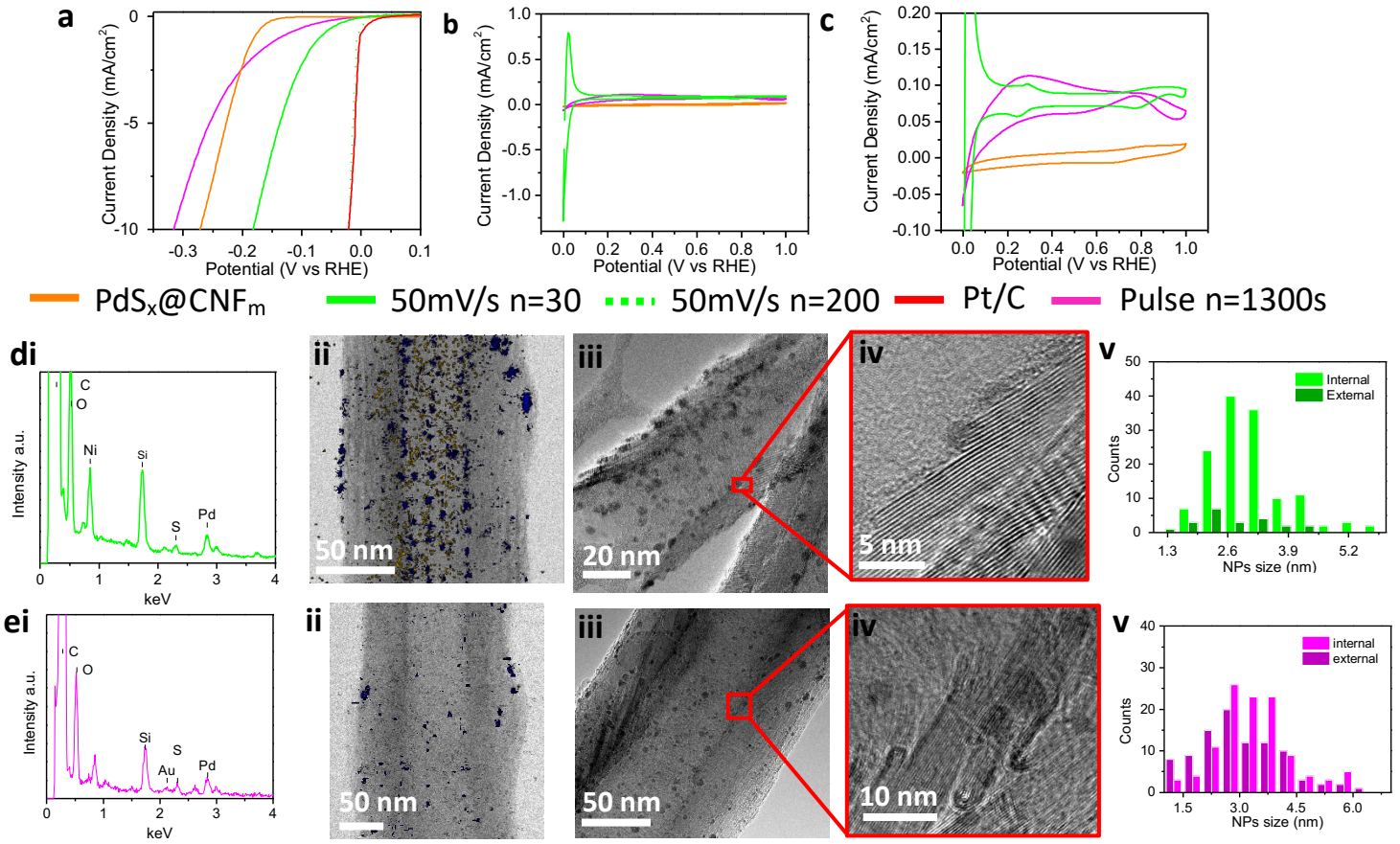

Figure 2. 12 a) *HER LSV for $PdS_x@CNF_m$ Initial (orange), n=1300s Pulsing (Pink), where n is the number of seconds at each potential -0.9 and 1.2V, PdS* ***(b)*** *CV for $PdS_x@CNF_m$, (pulsing pink) and $PdS_x@CNF_m$ (initial black)* ***(c)*** *magnification of CV for $PdS_x@CNF_m$, (pulsing pink) and $PdS_x@CNF_m$ (initial black)* ***(di)*** *EDX Graph* ***(ii)*** *EDX mapping image* ***(iii-iv)*** *HRTEM of $PdS_{x-y}@CNF_m$* ***(v)*** *Particle size distribution 3.07 ± 0.81 nm external 2.70 ± 0.78 nm* ***(e i)*** *EDX Graph* ***(ii)*** *EDX mapping image* ***(iii-iv)*** *HRTEM of $PdS_x@CNF_m$ after pulsing* ***(v)*** *Particle size distribution 3.33 ± 0.95 nm external 3.00 ± 1.08 nm*

With the development of a wide potential window activation procedure (see experimental) which is able to improve the PdS_x@CNF_m with respect to the HER. **Figure 2. 12c** (**i-v**) shows the activated material characterised by EDS mapping and TEM, both oxidative and reductive cycling in the potential window generates a material with open internal edges shown in **Figure 2. 12c** (**iv**) with intimate interactions with the PdS_x NPs. **Figure 2. 13a** Shows how progressive cycling between -0.9 and 1.2V increases the HER activity through LSV curves and the η_{10} value plotted against number of scans, 200 cycles was used as the end point for activation at 50mv/s as the η_{10} value becomes concordant and remains steady up to 1000 cycles (**Figure 2. 13b**).

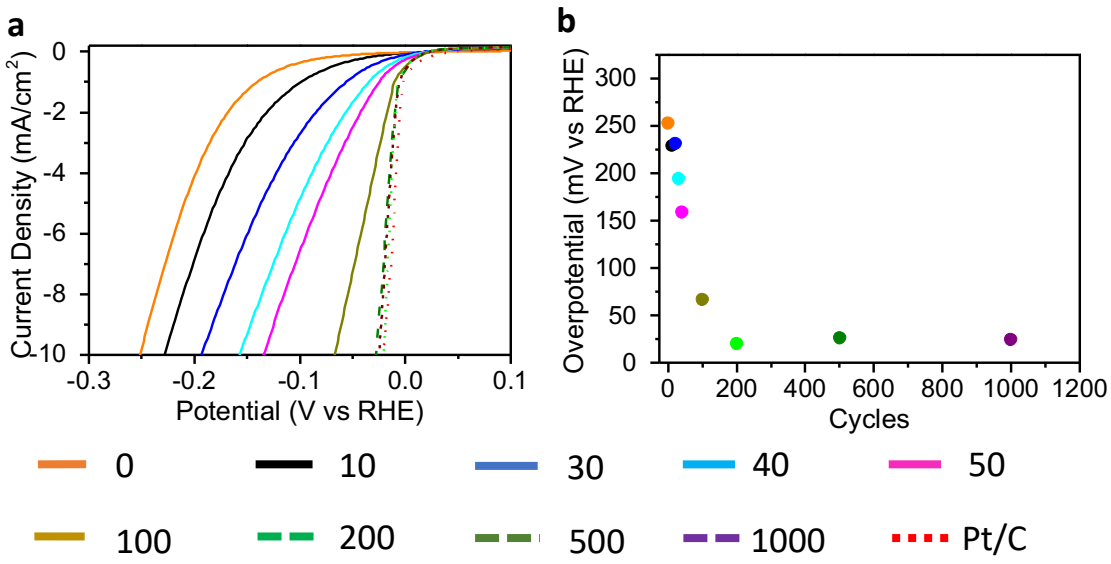

***Figure 2. 13 a**) HER LSV for PdS_x@CNF_m after 1000 wide window activation cycles to produce PdS_{x-y}@CNF_m (**b**) plot of overpotential at 10ma/cm^{-2} (η_{10}) vs no. of cycles*

Figure 2. 12c (**i-ii**) shows EDX mapping of the NPs in the material internally PdS_x is present whereas externally sulfur has begun to dissolve into the solution but is still present at some NPs. The PdS_{x-y}@CNF_m showed an exceptionally low Tafel slope of 14mV/Dec compared with 28mV/Dec for the initial commercial Pt/C (**Figure 2. 14b)**. This reduction in Tafel slope is not only observed in the PdS_{x-y}@CNF_m but also in the Pt/C where the post activation Tafel slope

is reduced to 16mV/Dec, despite the decrease in Tafel slope of the Pt/C the η_{10} value does not improve.

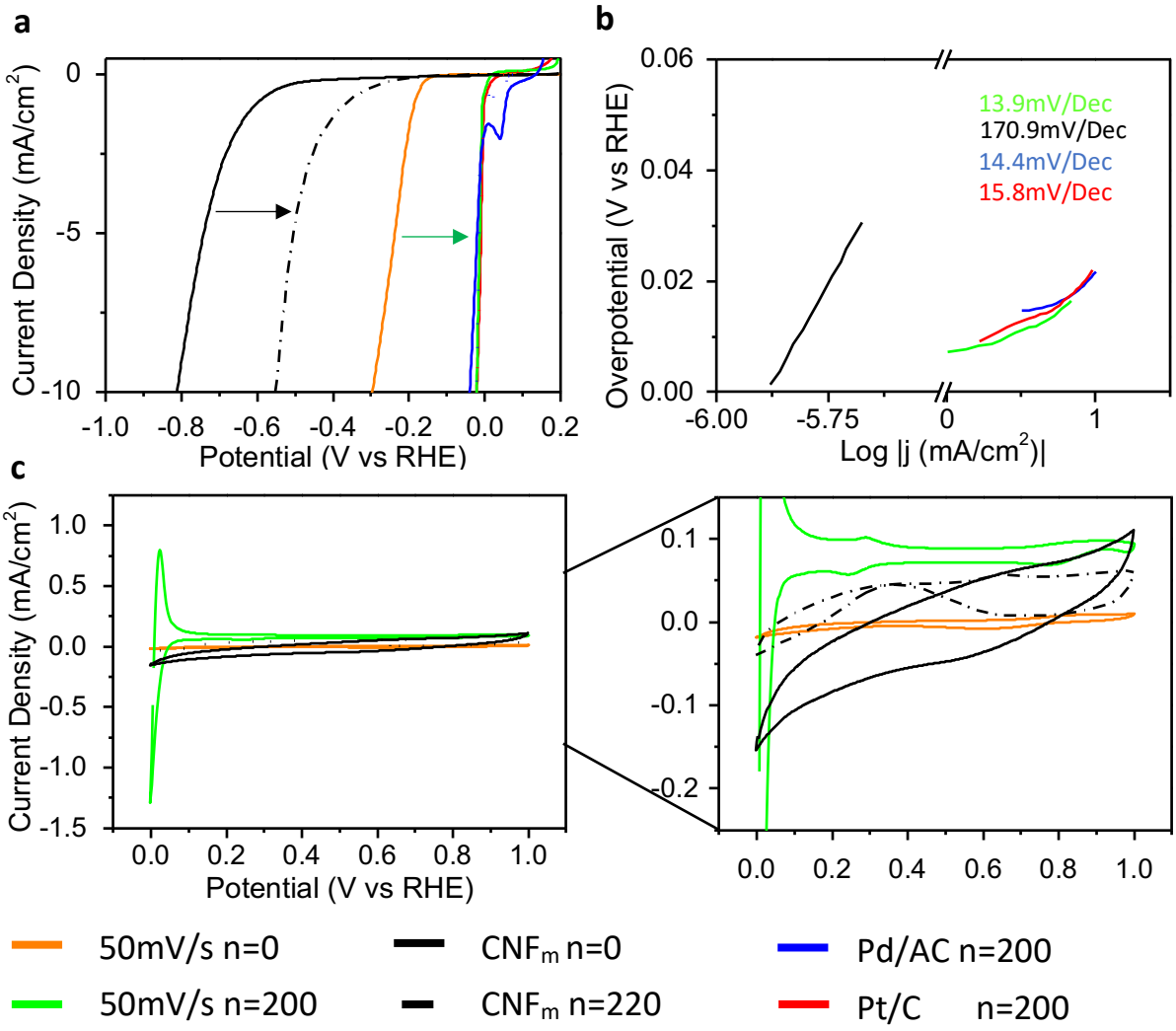

Figure 2. 14 (a) *HER LSV comparison for before and after wide window activation* ***(b)*** *Tafel plots after activation* ***(c)*** *CV before and after activation for CNF$_m$ (black) and before PdS$_x$@CNF$_m$ (orange) and after PdS$_{x-y}$CNF$_m$ (green)* ***(d)*** *Magnification for CV before and after activation CNF$_m$ (black) and PdS$_x$@CNF$_m$ before (orange) after PdS$_{x-y}$@CNF$_m$ (green)*

Figure 2. 14a shows the LSV before and after activation for CNF$_m$ vs PdS$_x$@CNF$_m$ with the latter now able to compete with the benchmark Pt/C commercial catalyst. The activation protocol increased the activity of the CNF$_m$ and PdS$_x$@CNF$_m$ materials to a similar extent; each of the four parameters mentioned above showed improvement. The change was most notable in the η_{10} value which decreased by 260mV and 274mV for CNF$_m$ and PdS$_x$@CNF$_m$

respectively, and the electrochemically activated material $PdS_{x-y}@CNF_m$ (**Figure 2. 14**, green) is now considered to be our active catalyst.

During the activation of the material the growth of the hydrogen desorption peak at 0.03V shown in **Figure 2. 14c** can be observed.[55] An increase in the ability of the material to adsorb protons is key for its activity as a catalyst and is in line with the hydrogen spill-over theory which says that adsorbed species at the active catalyst can become adsorbed either physically or chemically to the support surface due to species mobility.[56] Having a reserve of adsorbed protons ready to shuttle towards the active catalyst has been shown to be of great advantage in these materials.[57] The activity of the material can be related to the growth of this peak and therefore attributed significantly to the selective opening and oxidation of the edges as a similar improvement in activity can be seen in the CNF_m sample when subjected to the same procedure. The hydrogen desorption peak can be used to qualitatively show that the material is activated towards the HER, there a clear relationship between increasing the peak height/area to increased activity the increase in activity shown continues to improve after the peak has formed (**Figure S6**).

2.5.4 Cyclability and Mechanistic Details

The stability of a catalyst for applications in hydrogen fuel cells or electrolysers is crucial for the longevity of these technologies. Electrocatalysts tend to be single use, once they have degraded that electrode material will need to be replaced. During the activation of $PdS_x@CNF_m$ we were able to consume the active species and regenerate it by further wide window cycling, recovering the original performance. Using a range of electrochemical techniques including cyclic voltammetry (CV), linear sweep voltammetry (LSV) and chronoamperometry (CA) we were able to elucidate the species responsible for the high activity of the material.

Due to the complex nature of the active $PdS_{x-y}@CNF_m$, elucidation of mechanistic details poses a significant challenge. A combination of structural characterisation and extensive electrochemical experimentation has led us to deduce the intricate interplay between each component of $PdS_{x-y}@CNF_m$. As shown in **Scheme 2. 3** and previous sections the material is activated by repeated oxidative and reductive cycling. In order to access the activated state, the material must be scanned through the entire potential range proposed in the material activation section.

2.5.5 Chronoamperometric Switching

Chronoamperometric (CA) experiments are used to evaluate the stability of material to different potentials. CA was performed at -0.1, -0.5 and -0.9 V, as a function of time for $PdS_{x-y}@CNF_m$ and compared the results with a CNF_m background and Pt/C benchmark electrocatalysts (**Figure 2. 15**). CA experiments showed that the relationship between current decrease over time for activated CNF_m and $PdS_{x-y}@CNF_m$ were distinctly different. Understanding the current responses of the materials was aided by CV, providing an insight into the species that are evolving during the experiment.

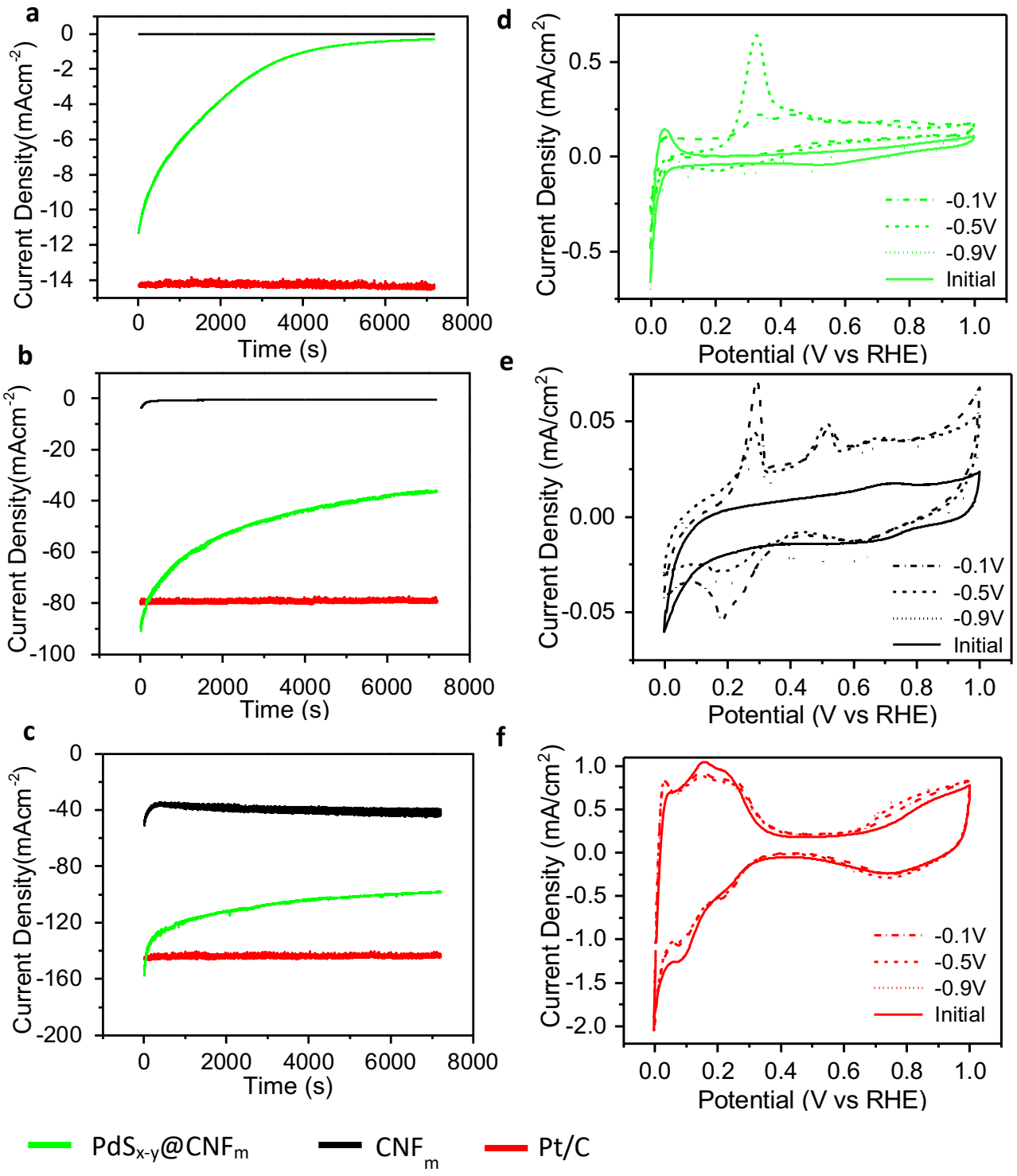

Figure 2. 15 *Chronoamperometric experiments with duration of 2 hours for CNF_m (black), $PdS_{x-y}@CNF_m$ (green) and Pt/C (red) at* ***(a)*** *-0.1V* ***(b)*** *-0.5V* ***(c)*** *-0.9V. CV pre and post CA for* ***(d)*** *$PdS_{x-y}@CNF_m$ and* ***(e)*** *CNF_m* ***(f)*** *Pt/C*

Figure 2. 15a-c demonstrates the behaviour of the materials at different applied potentials of -0.1, -0.5 and -0.9V respectively. The activated electrode materials $PdS_{x-y}@CNF_m$ and CNF_m show similar behaviours; an initial decrease in current at negative potentials followed by a plateau. The presence of PdS_x NPs gives a significant increase in the current density produced, CNF_m are relatively inactive when compared to the hybrid $PdS_{x-y}@CNF_m$ at -0.1 and -0.5V, only at -0.9V does the CNF_m show inherent activity towards the HER. The initial decay in current can be attributed to the consumption of the adsorbed hydrogen present in the oxygen functionalised carbon, then the reduction of the oxygen containing groups have been well documented in the literature involving electrochemically reduced graphene oxide.[54] It is shown that it requires significant negative potential and cycling down to -1.3V vs the saturated calomel electrode (SCE) to reduce the majority of C=O groups, however some C-OH groups will survive these potentials. At higher overpotentials the $PdS_{x-y}@CNF_m$ is initially more active than Pt/C in that it generates more current, due to the increased activity of the carbon support at these high overpotentials.

Figure 2. 15d and **e** show the generation of new oxidation peaks in the CV at ~0.3V and 0.6V due to the continued application of negative potential during CA experiments. These can be attributed to the increased presence of dangling bonds at the internal edges and external defects of the CNF_m support, increase in the density of defects due to activation allows the kinetically slow oxidation of carbon to be seen over the bulk graphitized nature of the initial CNF_m.[21,58–60] It is well reported that edge sites increase activity towards surface adsorbed reactions.[60–62] These terminal carbons are oxidised to CO_2 and CO respectively when cycling between 0 and 1V during the CV; these are not reversible processes like the quinone-hydroquinone behaviour shown by CNTs in oxidative cycling.[58,63–65] On comparison of the

PdS_{x-y}@CNF_m and CNF_m CVs a significant increase in the relative intensity the 0.3V carbon oxidation peak can be attributed to the catalytic behaviour of the PdS_{x-y} NPs.

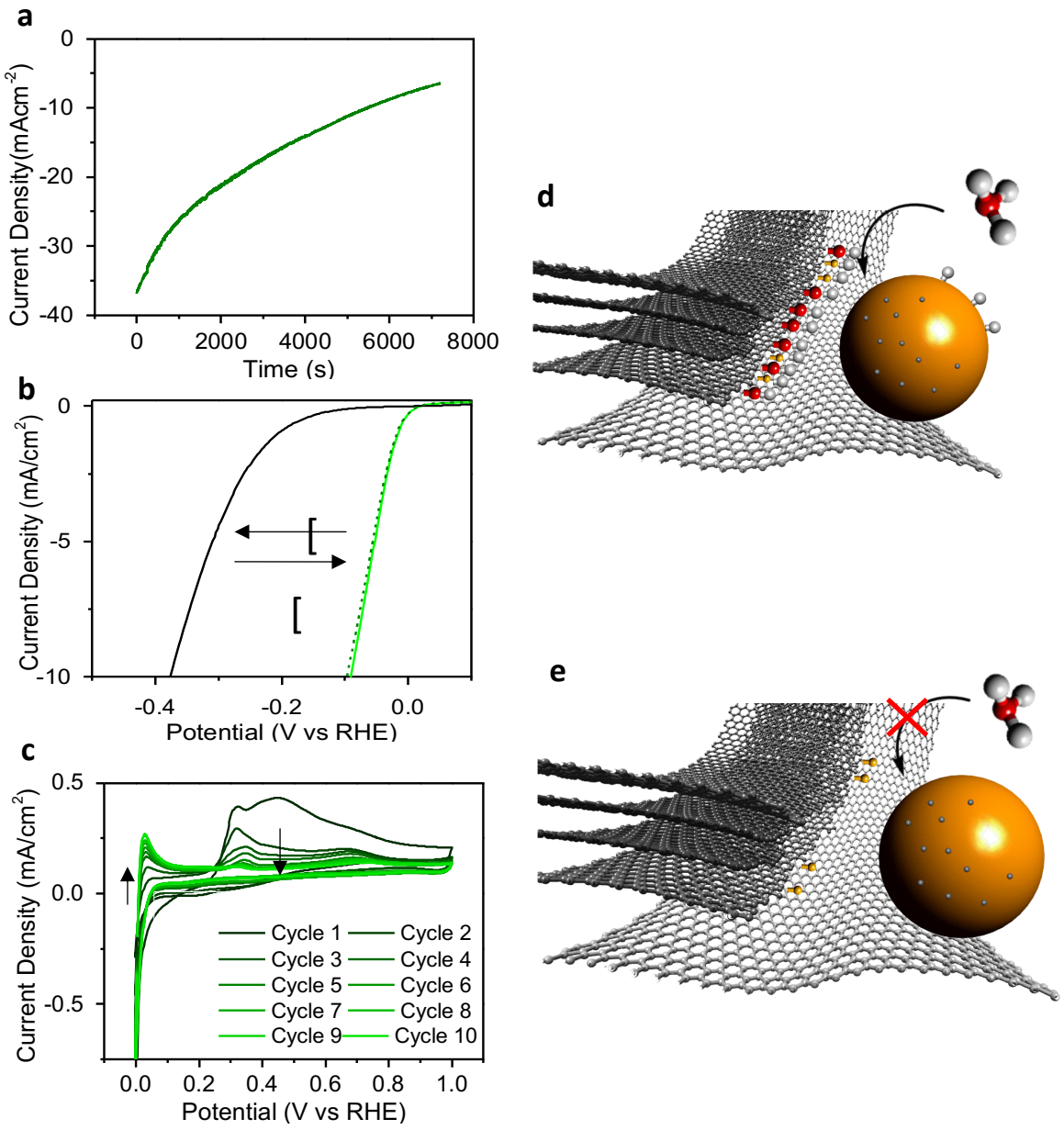

Figure 2. 16 (a) *CA at -0.3V for PdS_{x-y}@CNF_m (green)* ***(b)*** *HER LSV before CA at -0.3V, after CA and after 10 CV cycles to regenerate hydrogen desorption peak shown in B.* ***(c)*** *CV between 0 and 1V post CA showing decrease in oxidative peaks ~0.3V and ~0.6V related to CO_2 and CO evolution in acidic conditions alongside an increase in hydrogen adsorption peak.*[66] ***(d)*** *Schematic of HER before CA* ***(e)*** *Schematic of HER after CA*

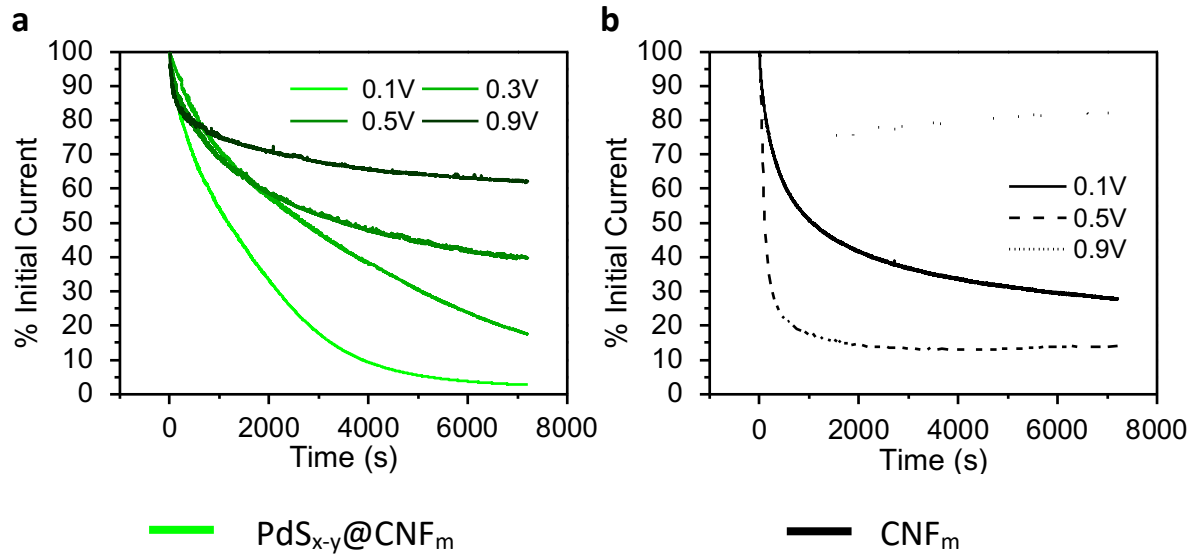

Figure 2. 17 *CA* ***a****)* PdS_{x-y}*@*CNF_m *(green) and (****b****)* CNF_m *(black) as % of initial current*

CA performed at -0.3V (**Figure 2. 16a**) allowed further investigation of the oxidation peaks shown in **Figure 2. 16c**, due to oxidative cycling the hydrogen desorption peak increases and presence of the carbon oxidation peaks decrease as these moieties become saturated with oxygen terminating groups. Due to the nature of the edges and the species generated by holding at negative potential, the initial oxidation of these terminating carbon atoms is not reversible. **Figure 2. 16b** shows the LSV before and after reduction by CA at -0.3V, the activity is then recovered by 10 oxidation cycles between 0 and 1V during the CV in **Figure 2. 16c**, this is shown schematically in **Figure 2. 16 d** and **e** as the stripping and reoxidation of the carbon CNF_m support. The degradation profiles of the chronoamperometric experiments show a decreasing % loss of current from -0.1V to -0.9V (**Figure 2. 17**), this implies that the degradation of the active catalyst competes with the HER at less negative potentials. This is further confirmed by the increased charge of the peaks present in the CV post exposure to less negative potentials (**Figure 2. 15 d-e**).

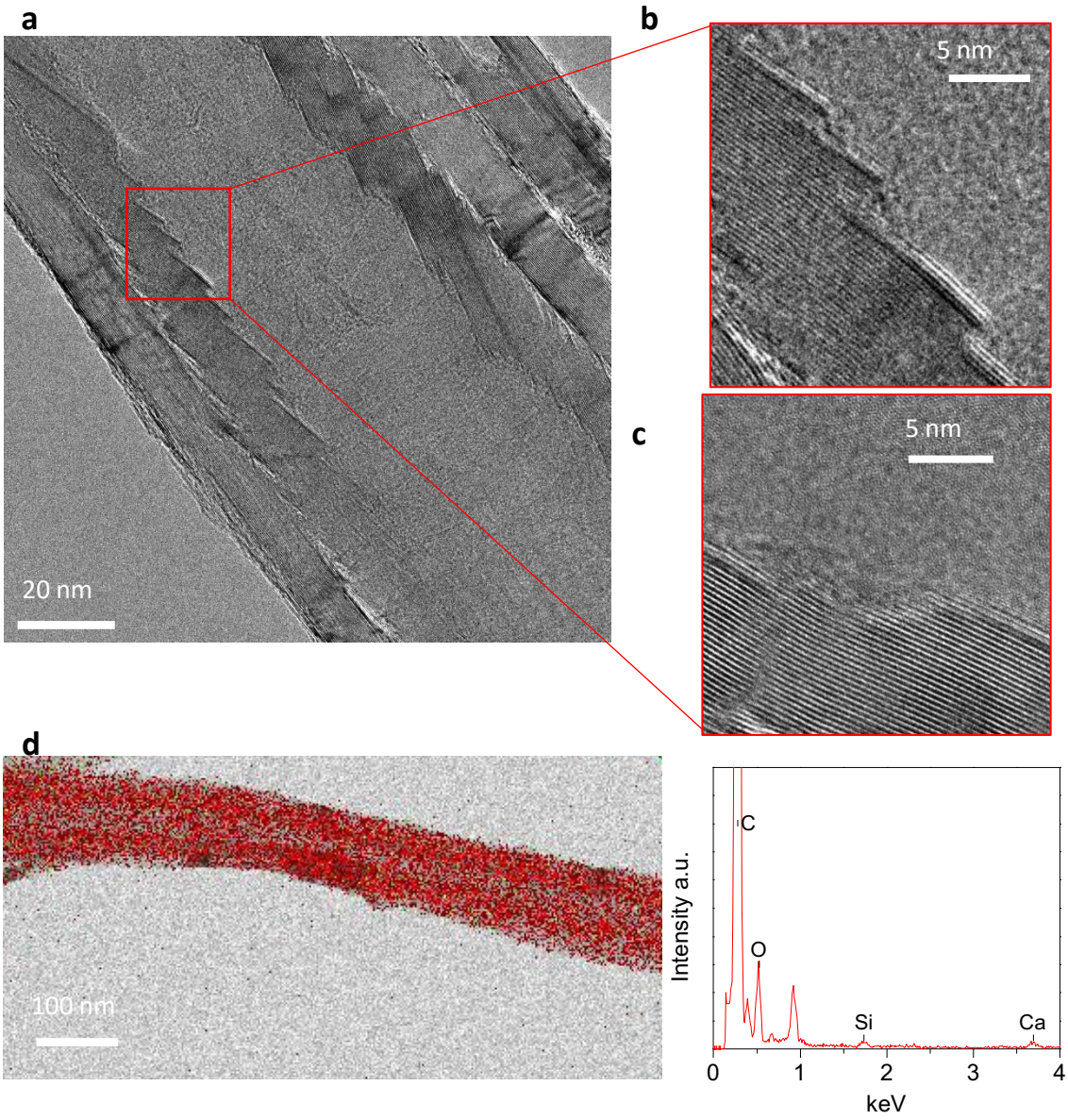

Figure 2. 18 (a) *HRTEM images of activated CNF_m after chronoamperometric stability testing* ***(b-c)*** *Internal graphitic edges* ***(d)*** *EDX mapping of activated CNF_m after chronoamperometric stability testing, EDX plot C (red)*

TEM images of activated CNF_m after CA experiments (**Figure 2. 18**) show that the internal step edges have been irreversibly opened and degraded. Continuous reductive chronoamperometry has the effect of "deactivating" the material. However, to what extent the material is "deactivated" depends on the applied potential. Interestingly there is a decrease in the loss of current on increasing applied potential, for example, there is greater

decrease in current as a percentage of initial current in the -0.1V decreasing to -0.9V. This is further shown in the CV post CA in **Figure 2. 15**d where -0.9V is not dissimilar to the initial CV.

Reductive potentials produce a $PdS_{x-y}@CNF_m$ resting state where the support is reduced and unable to act as a shuttle for adsorbed hydrogen atoms. This hypothesis is confirmed by cycling experiments and chronoamperometric experiments (**Figure 2. 15**) where the active hydrogen desorption peak can be selectively removed when applying a negative potential or cycling to negative potentials (**Figure S7**). The Pd present at the edges catalyses the cleavage of the C-O bond along with the C-C bonds at -0.1V.[67]

This not only provides an insight into reasons for activation but also the observed kinetics of the reactions. At -0.1V the reduction of oxygen containing groups at the surface of the carbon support dominates the current generated. The stored hydrogen atoms are consumed through hydrogen evolution and then the current plateaus, this same behaviour is seen in the CNF_m background, as this material cannot undergo HER at such low potentials the current generated tends towards 0 after hydrogen is evolved and oxygen containing groups are depleted. The species formed can then be seen in the CV (**Figure 2. 15**) as dangling bonds which are readily oxidised.[68] These are less prominent in the CV at -0.9V, the change between -0.5V and -0.9V is due to the adsorption, migration of protons and subsequent evolution of hydrogen is active at both PdS_{x-y} NPs surface and CNF_m support surface. The oxidative peaks in the CV post chronoamperometry are no longer seen (**Figure 2. 15**d) proving that there are not the same exposed carbon edges to be oxidised this phenomenon could be due to the reaction of sulfur with the newly exposed edges with after removal of oxygen (**Scheme 2. 4**).[69]

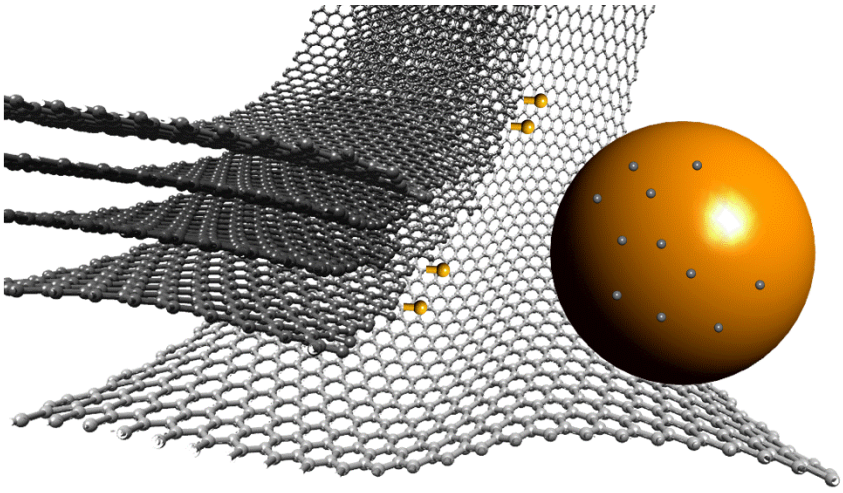

Scheme 2. 4 *Schematic of material generated after CA of PdS_{x-y}@CNF_m at -0.9V showing opened edges which are capped with sulfur groups. PdS_xNP (orange), S (yellow), Pd (blue), O (red) and H (white)*

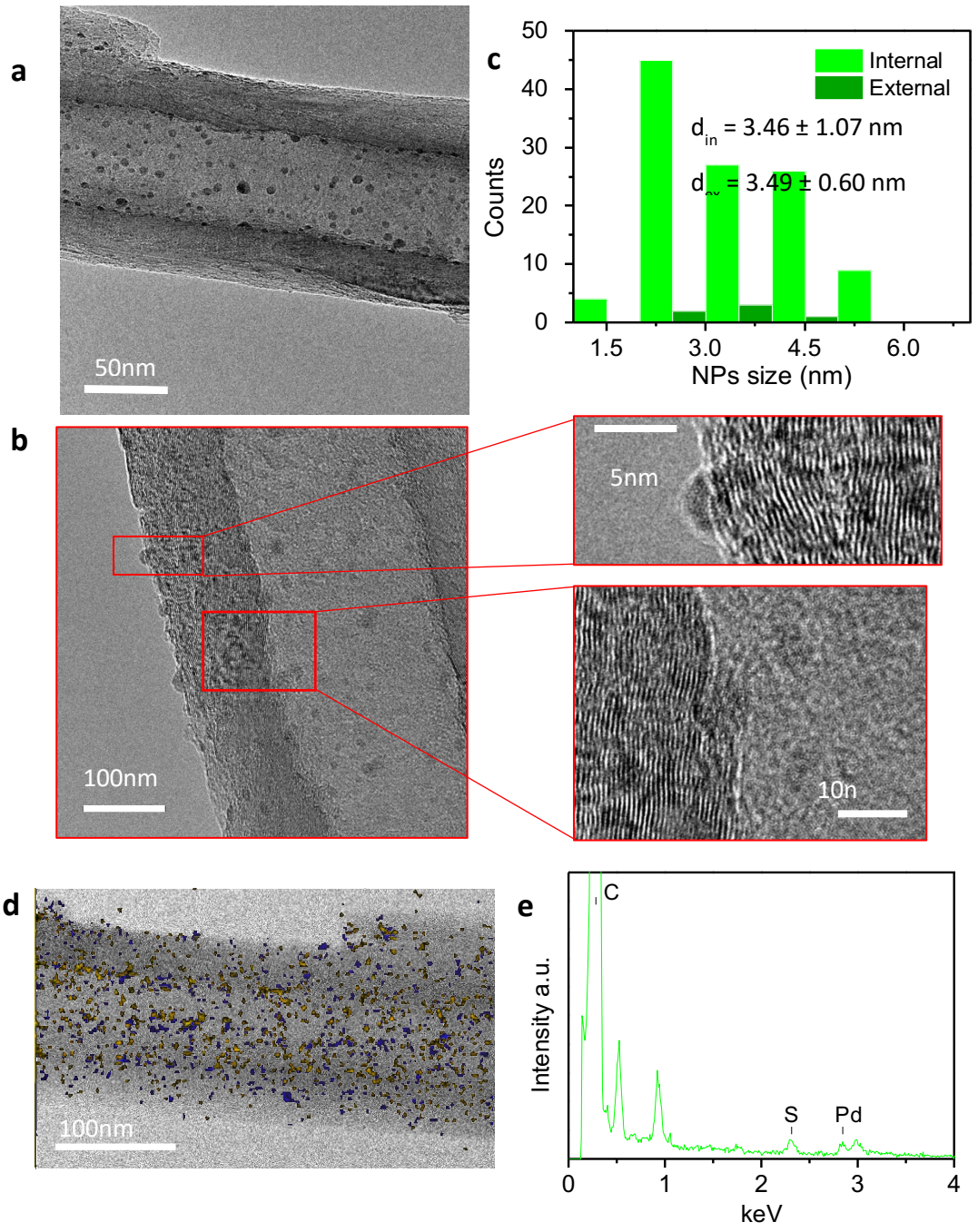

Figure 2. 19 (a-b) *HRTEM of $PdS_{x-y}@CNF_m$ after negative chronoamperometry and stability cycling* ***(c)*** *Histogram of internal (green) 3.4±1 nm and external (dark green) 3.5 ±0.6 nm NPs (d-e) EDX mapping of $PdS_{x-y}@CNF_m$ after negative chronoamperometry and stability cycling Pd (blue), S (yellow).*

The HRTEM images in **Figure 2. 19a** show that electrochemical activation by cycling does not change the tubular structure of the material, the size distribution of the nanoparticles are consistent with initial sample **Figure 2. 6**. The graphitisation of the external and internal layers was maintained with inter layer d-spacing of 0.36 nm and 0.33 nm respectively shown in

Figure 2. 19c indicating that the oxidisation of the carbon has not been extensive enough to increase the d-spacing between layers. Characteristic folded edges are no longer present in the extensively cycled sample. EDX mapping an graph in **Figure 2. 19d-e** shows that sulfur is still present, predominantly inside of the nanofibers.

We have a material which is able to avoid degradation due to kinetically favouring the production of hydrogen, proved by lack of oxidative peaks in the CV after chronoamperometry at -0.9V (**Figure 2. 15**d). This material is extremely interesting due to the working potential at the cathode of a commercial electrolyser would need to be in excess of -1.2V in order to facilitate water splitting at the anode. Our material being more stable at more negative potentials is advantageous as it would avoid the inherent degradation at lower overpotentials (**Figure 2. 17**).

Confinement within the carbon structure slows the loss of sulfur from the particles caused by the activation protocol. This encapsulation appears to maintain an increased stability due to interactions with edges and reduced Pd loss when confined which was confirmed by the use of a milled nanofiber with a less tubular structure ($PR19_m$) shown in (**Figure S 9**). We demonstrate that this increases the longevity of the catalyst and should maintain the materials activity long after external particles are dissolved. The particle size remains small keeping the surface area high.

2.5.7 OCP Switching

Once activated, recovery of the material through further oxidation of the carbon support is possible at positive potentials, as shown in **Figure 2. 16**. This phenomenon is also shown in (**Figure 2. 20**a) where the sample is left at OCP and recovered, with the loss of the hydrogen

desorption peak (**Figure 2. 20**b). Pre-polarization has been used in sensors to increase the activity of electrodes to specific analytes.[70] Passivation of the active surface occurs under open circuit conditions. The OCP measurement shown in **Figure 2. 20**c is taken directly after wide window cycles and is therefore at the 0V end point of this cycle.

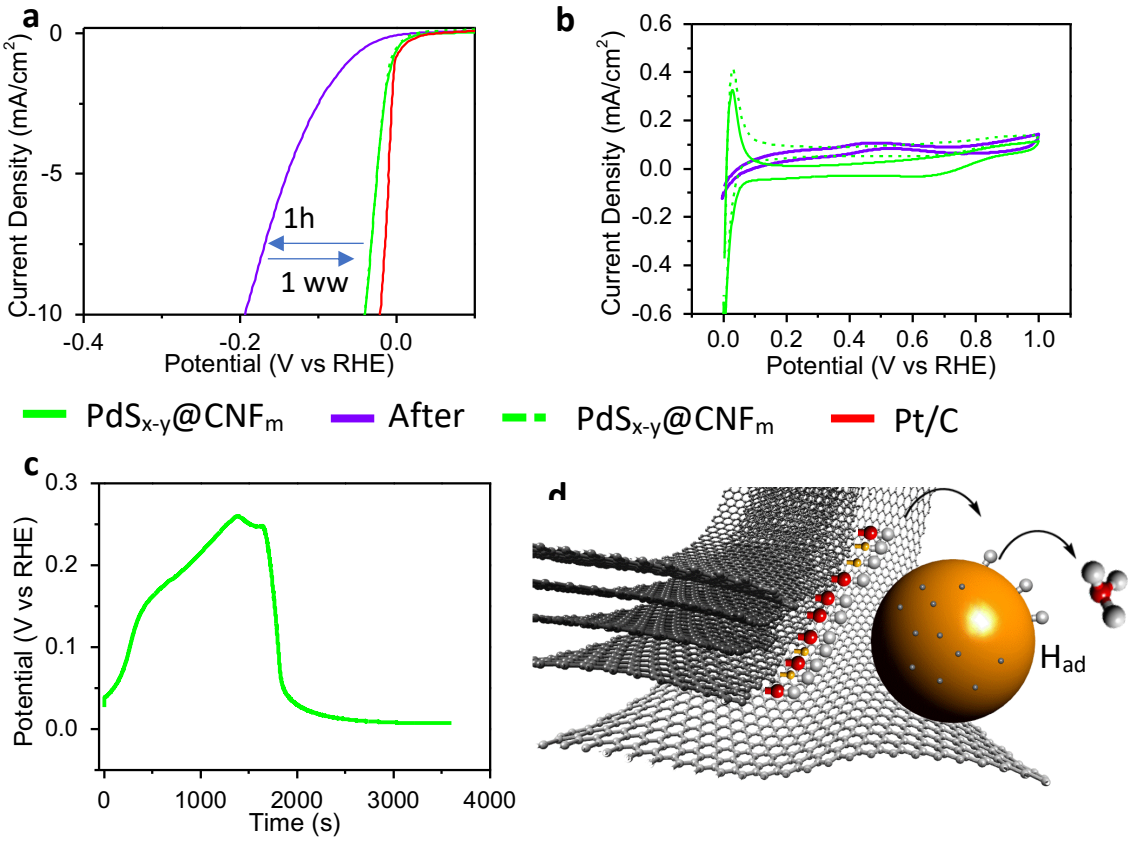

Figure 2. 20 (a) *LSV curves of $PdS_{x-y}@CNF_m$ before 1h OCP (green), $PdS_{x-y}@CNF_m$ after 1h OCP (purple) and after an additional wide window cycle (green dash) compared with Pt/C initial (red).* ***(b)*** *CV of $PdS_{x-y}@CNF_m$ before (green) and after OCP (purple) and after regeneration (green dash)* ***(c)*** *OCP plot of Potential (V) over time 1h.* ***(d)*** *Schematic of Proton desorption and suspected route to deactivation.*

During the OCP measurement the potential increases, indicating a surface oxidation is occurring (**Figure 2. 20**c). We propose that this is due to the release of adsorbed protons on local oxygen containing groups (**Figure 2. 20**d). The potential then decreases and plateaus, so all available surface is fully passivated, and the system returns to equilibrium. There will also be a contribution from desorption of protons from within the lattice of the Pd present.

2.6 Conclusions

The synthesis of novel crystalline PdS_x nanoparticles deposited at CNF_m and the electrochemical generation and switch between an active catalyst PdS_{x-y}@CNF and resting PdS_{x-y}@CNF catalyst for HER which is capable of competing with Pt/C has been reported. The active catalyst is irreversibly obtained through the implementation of a wide window activation from -0.9 V to 1.2 V at either 50 or 10 mV/s, selectively oxidising and reducing the internal folded edges of the CNF_m. Mild oxidation of the carbon support combined with the redeposition of Pd atoms at the surface of the PdS nanoparticles and shuttling of S between the NPs and carbon support confined within the tubular structure we are able to improve the materials activity towards the HER. The dissolved Pd contributes to the catalytic edge opening process and allows us to access the activated support material much faster than in the absence of NPs. The synergistic behaviour between the new oxygen and sulfur terminated edge sites and the NPs adhered to these surfaces creates a catalyst that equals and improves upon commercial Pt/C with respect to onset potential, η@10mAcm^{-2}, i_0 and Tafel slope. We have demonstrated the extent at which the CNF_m are electrochemically non-innocent and how we are able to exploit this electrochemically and electrocatalytically with the presence of PdS_x NPs to generate a material with promise at extreme negative potentials for use in electrolysers. Further studies of our activated material will show its ability as a catalyst for other key reactions within electrolysers and fuel cells.

2.7 References

1 F. Dawood, M. Anda and G. M. Shafiullah, *Int. J. Hydrogen Energy*, 2020, **45**, 3847–3869.

2 Committee on Climate Change, *Hydrogen in a low-carbon economy*, 2018.

3 Z. Abdin, A. Zafaranloo, A. Rafiee, W. Mérida, W. Lipiński and K. R. Khalilpour, *Renew. Sustain. Energy Rev.*, 2020, **120**, 1-32.

4 J. O. M. Bockris, *Int. J. Hydrogen Energy*, 2008, **33**, 2129–2131.

5 H. Wang and L. Gao, *Curr. Opin. Electrochem.*, 2018, **7**, 7–14.

6 A. Eftekhari, *Int. J. Hydrogen Energy*, 2017, **42**, 11053–11077.

7 S. Sarkar and S. C. Peter, *Inorg. Chem. Front.*, 2018, **5**, 2060–2080.

8 Z. Luo, Y. Ouyang, H. Zhang, M. Xiao, J. Ge, Z. Jiang, J. Wang, D. Tang, X. Cao, C. Liu and W. Xing, *Nat. Commun.*, 2018, **9**, 1–8.

9 T. F. Jaramillo, K. P. Jørgensen, J. Bonde, J. H. Nielsen, S. Horch and I. Chorkendorff, *Science.*, 2007, **317**, 100–102.

10 B. You and Y. Sun, *Chempluschem*, 2016, **81**, 1045–1055.

11 X. Chia and M. Pumera, *Chem. Soc. Rev.*, 2018, **47**, 5602–5613.

12 M. Barawi, I. J. Ferrer, J. R. Ares and C. Sanchez, *ACS Appl. Mater. Interfaces*, 2014, **6**, 20544–20549.

13 X. Chia, A. Adriano, P. Lazar, Z. Sofer, J. Luxa and M. Pumera, *Adv. Funct. Mater.*, 2016,

26, 4306–4318.

14 L. Zhang, Q. Chang, H. Chen and M. Shao, *Nano Energy*, 2016, **29**, 198–219.

15 M. H. Naveen, Y. Huang, S. Bisalere Kantharajappa, K. D. Seo, D. S. Park and Y. B. Shim, *ACS Appl. Energy Mater.*, 2021, **4**, 575–585.

16 X. Zou and Y. Zhang, *Chem. Soc. Rev.*, 2015, **44**, 5148–80.

17 X. M. Liu, Y. Tang, E. S. Xu, T. C. Fitzgibbons, G. S. Larsen, H. R. Gutierrez, H. H. Tseng, M. S. Yu, C. S. Tsao, J. V. Badding, V. H. Crespi and A. D. Lueking, *Nano Lett.*, 2013, **13**, 137–141.

18 C. Hu and L. Dai, *Adv. Mater.*, 2017, **29**, 1–9.

19 S. A. Grigoriev, M. S. Mamat, K. A. Dzhus, G. S. Walker and P. Millet, *Int. J. Hydrogen Energy*, 2011, **36**, 4143–4147.

20 A. La Torre, M. D. C. Giménez-López, M. W. Fay, G. A. Rance, W. A. Solomonsz, T. W. Chamberlain, P. D. Brown and A. N. Khlobystov, *ACS Nano*, 2012, **6**, 2000–2007.

21 M. A. Lebedeva, T. W. Chamberlain, A. Thomas, B. E. Thomas, C. T. Stoppiello, E. Volkova, M. Suyetin and A. N. Khlobystov, *Nanoscale*, 2016, **8**, 11727–11737.

22 G. Dong, M. Fang, H. Wang, S. Yip, H. Y. Cheung, F. Wang, C. Y. Wong, S. T. Chu and J. C. Ho, *J. Mater. Chem. A*, 2015, **3**, 13080–13086.

23 J. C. McGlynn, T. Dankwort, L. Kienle, N. A. G. Bandeira, J. P. Fraser, E. K. Gibson, I. Cascallana-Matías, K. Kamarás, M. D. Symes, H. N. Miras and A. Y. Ganin, *Nat. Commun.*, , DOI:10.1038/s41467-019-12831-0.

24 M. Brust, M. Walker, D. Bethell, D. J. Schiffrin and R. Whyman, 2000, 801–802.

25 R. Lu, W. Gan, B. H. Wu, H. Chen and H. F. Wang, *J. Phys. Chem. B*, 2004, **108**, 7297–7306.

26 J. Christopher Love, D. B. Wolfe, R. Haasch, M. L. Chabinyc, K. E. Paul, G. M. Whitesides and R. G. Nuzzo, *J. Am. Chem. Soc.*, 2003, **125**, 2597–2609.

27 H. Murayama, N. Ichikuni, Y. Negishi, T. Nagata and T. Tsukuda, *Chem. Phys. Lett.*, 2003, **376**, 26–32.

28 C. Vericat, M. E. Vela, G. Corthey, E. Pensa, E. Cortés, M. H. Fonticelli, F. Ibañez, G. E. Benitez, P. Carro and R. C. Salvarezza, *RSC Adv.*, 2014, **4**, 27730–27754.

29 V. I. Rozhdestvina, A. A. Udovenko, S. V. Rubanov and N. V. Mudrovskaya, *Crystallogr. Reports*, 2016, **61**, 193–202.

30 A. Marmier, P. S. Ntoahae, P. E. Ngoepe, D. G. Pettifor and S. C. Parker, *Phys. Rev. B - Condens. Matter Mater. Phys.*, 2010, **81**, 4–7.

31 B. B. Huang, L. Y. Chen, Y. Wang, L. Z. Ouyang and J. S. Ye, *Chem. Eur. J.*, 2017, **23**, 7710–7718.

32 R. Collins, R. Kaner, P. Russo, D. Avignant and A. Wold, *Inorg. Chem.*, 1979, **18**, 727–729.

33 N. E. Brese, P. J. Squattrito and J. A. Ibers, *Acta Crystallogr. Sect. C*, 1985, **41**, 1829–1830.

34 E. Swanson, H.E.; Tatge, *Standard X-ray diffraction powder patterns I, National Bureau of Standards (U.S.), Circular, 539, 1-95 (1953)*, .

35 S. Gates-Rector and T. Blanton, *Powder Diffr.*, 2019, **34**, 352–360.

36 R. Bhatt, S. Bhattacharya, R. Basu, A. Singh, U. Deshpande, C. Surger, S. Basu, D. K. Aswal and S. K. Gupta, *Thin Solid Films*, 2013, **539**, 41–46.

37 J. R. J. R. C.D. Wagner, A.V. Naumkin, A. Kraut-Vass, J.W. Allison, C.J. Powell, NIST Standard Reference Database 20.

38 H. Bennettand and G. J. Ouver, *J. Chem. Educ.*, 1993, **70**, A25.

39 J. Wei, M. Zhou, A. Long, Y. Xue, H. Liao, C. Wei and Z. J. Xu, *Nano-Micro Lett.*, 2018, **10**, 1–15.

40 Z. Zhuang, J. Huang, Y. Li, L. Zhou and L. Mai, *ChemElectroChem*, 2019, **6**, 3570–3589.

41 T. Shinagawa, A. T. Garcia-Esparza and K. Takanabe, *Sci. Rep.*, 2015, **5**, 1–21.

42 S. Sarkar and S. C. Peter, *Inorg. Chem. Front.*, 2018, **5**, 2060–2080.

43 Y. Zhou, Y. Leng, W. Zhou, J. Huang, M. Zhao, J. Zhan, C. Feng, Z. Tang, S. Chen and H. Liu, *Nano Energy*, 2015, **16**, 357–366.

44 W. Zhou, J. Jia, J. Lu, L. Yang, D. Hou, G. Li and S. Chen, *Nano Energy*, 2016, **28**, 29–43.

45 S. Bong, B. Jang, D. Han and Y. Piao, *ACS Omega*, 2019, **4**, 20330–20334.

46 C. A. Martins, P. S. Fernández, H. E. Troiani, M. E. Martins, A. Arenillas and G. A. Camara, *Electrocatalysis*, 2014, **5**, 204–212.

47 K. Naga Mahesh, R. Balaji and K. S. Dhathathreyan, *Int. J. Hydrogen Energy*, 2016, **41**, 46–51.

48 J. Zheng, S. Zhou, S. Gu, B. Xu and Y. Yan, *J. Electrochem. Soc.*, 2016, **163**, F499–F506.

49 B. Cornelio, A. R. Saunders, W. A. Solomonsz, M. Laronze-Cochard, A. Fontana, J. Sapi,

A. N. Khlobystov and G. A. Rance, *J. Mater. Chem. A*, 2015, **3**, 3918–3927.

50 M. Baldauf and D. M. Kolb, *Electrochim. Acta*, 1993, **38**, 2145–2153.

51 S. Sarkar and S. Sampath, *Chem. Commun.*, 2014, **50**, 7359–7362.

52 X. Zhang, J. Zhu, C. S. Tiwary, Z. Ma, H. Huang, J. Zhang, Z. Lu, W. Huang and Y. Wu, *ACS Appl. Mater. Interfaces*, 2016, **8**, 10858–10865.

53 C. H. Choi, M. Kim, H. C. Kwon, S. J. Cho, S. Yun, H. T. Kim, K. J. J. Mayrhofer, H. Kim and M. Choi, *Nat. Commun.*, 2016, **7**, 1–9.

54 H.-L. Guo, X.-F. Wang, Q.-Y. Qian, F.-B. Wang and X.-H. Xia, *ACS Nano*, 2009, **3**, 2653–9.

55 M. Grdeń, M. Łukaszewski, G. Jerkiewicz and A. Czerwiński, *Electrochim. Acta*, 2008, **53**, 7583–7598.

56 D. P. Zhan, J. Velmurugan and M. V Mirkin, *J. Am. Chem. Soc.*, 2009, **131**, 14756–14760.

57 J. Park, S. Lee, H. E. Kim, A. Cho, S. Kim, Y. Ye, J. W. Han, H. Lee, J. H. Jang and J. Lee, *Angew. Chemie - Int. Ed.*, 2019, **58**, 16038–16042.

58 Y. Yi, J. Tornow, E. Willinger, M. G. Willinger, C. Ranjan and R. Schlçgl, *ChemElectroChem*, 2015, **2**, 1929–1937.

59 J. Li, R. Cui, Y. Chang, H. Huang, X. Guo, J. Wang, R. Liu, K. Chen, J. Kong, G. Xing and B. Sun, *RSC Adv.*, 2020, **10**, 36378–36385.

60 A. Ambrosi, A. Bonanni and M. Pumera, *Nanoscale*, 2011, **3**, 2256–2260.

61 Y. A. Kim, T. Hayashi, J. H. Kim and M. Endo, *J. Energy Chem.*, 2013, **22**, 183–194.

62 C. E. Banks, M. R. Moore, T. J. Davies and R. G. Compton, *Chem. Commun.*, 2004, **10**,

1804–1805.

63 F. Liu and D. Xue, *Chem. - A Eur. J.*, 2013, **19**, 10716–10722.

64 C. M. Yoon, D. Long, S. M. Jang, W. Qiao, L. Ling, J. Miyawaki, C. K. Rhee, I. Mochida and S. H. Yoon, *Carbon N. Y.*, 2011, **49**, 96–105.

65 Y. Yi, G. Weinberg, M. Prenzel, M. Greiner, S. Heumann, S. Becker and R. Schlögl, *Catal. Today*, 2017, **295**, 32–40.

66 S. G. Bratsch, *J. Phys. Chem. Ref. Data*, 1989, **18**, 1–21.

67 T. Shimada, S. Kubota, T. Yanase and T. Nagahama, *Carbon N. Y.*, 2014, **67**, 300–303.

68 M. Wang, R. Sun, Q. Wang, L. Chen, L. Hou, Y. Chi, C. H. Lu, F. Fu and Y. Dong, *Chem. - A Eur. J.*, 2018, **24**, 4250–4254.

69 D. H. R. Barton, E. Castagnino and J. C. Jaszberenyi, *Tetrahedron Lett.*, 1994, **35**, 6057–6060.

70 P. Zimmermann, A. Weltin, G. A. Urban and J. Kieninger, *Sensors (Switzerland)*, 2018, **18**, 2404.

2.7 Supporting Information

2.7.1 Structural

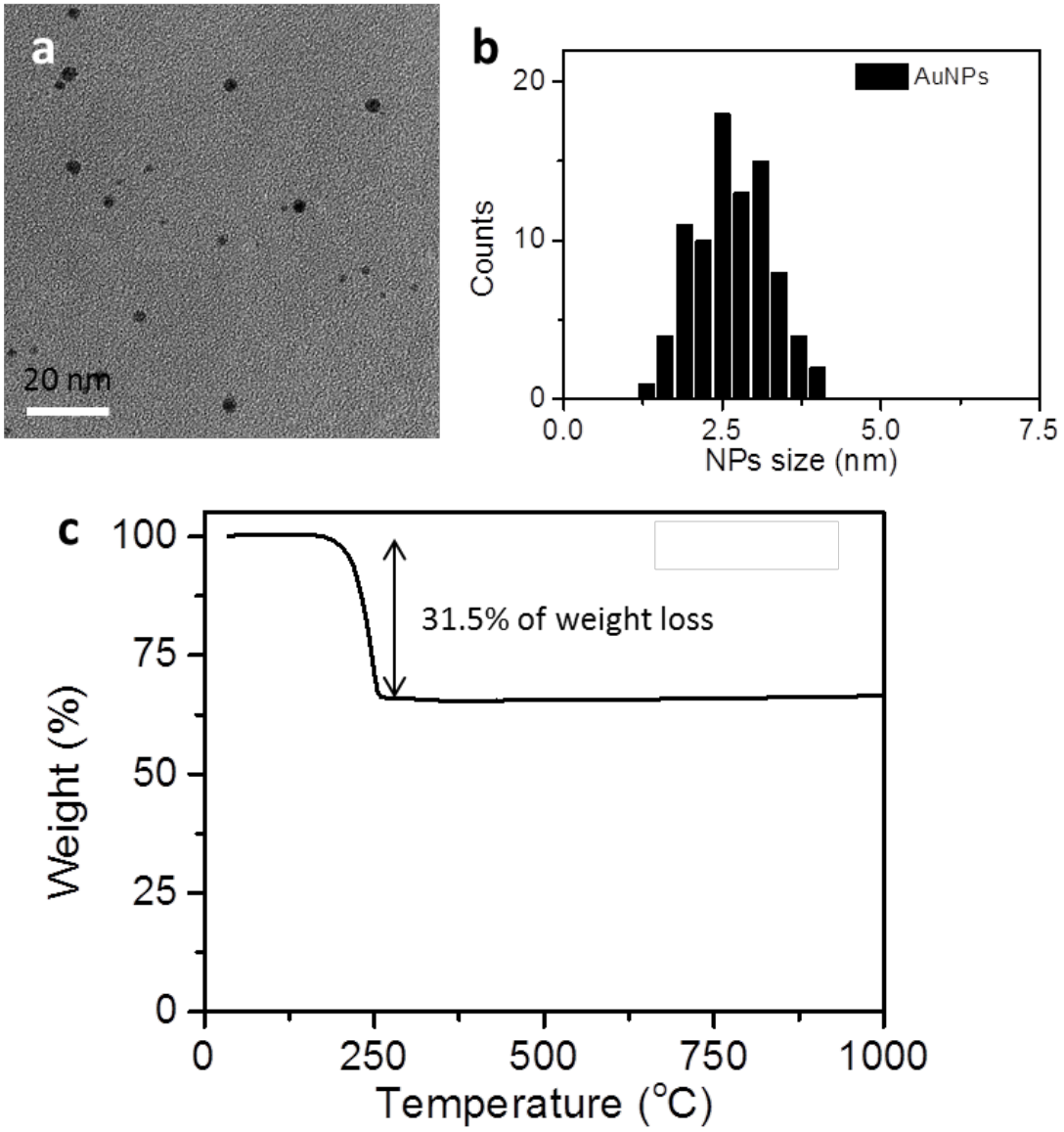

Figure S 1 (a) *HRTEM images,* ***(b)*** *size distribution measured by HRTEM (more than 80 NPs), and* ***(c)*** *TGA measurements of preformed gold nanoparticles in air show a 31.5% of surfactant and ~70% residual Au metal by weight. Scale bars is 20 nm.*

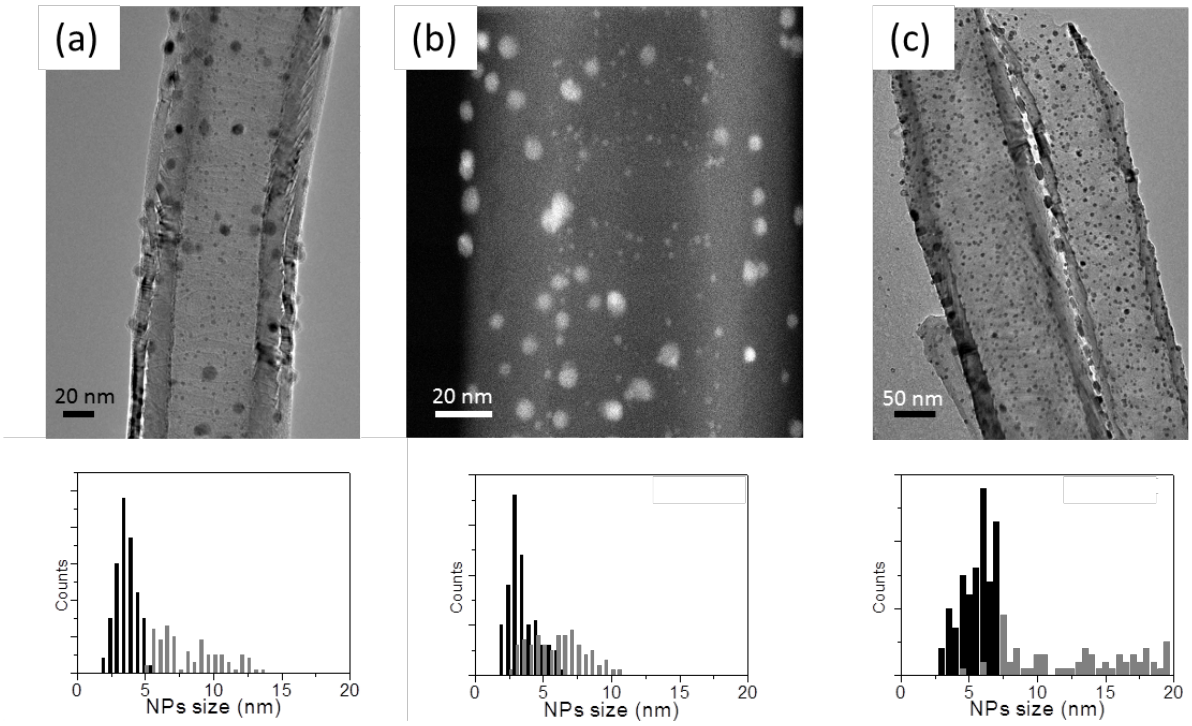

***Figure S 2**. TEM images of annealed palladium nanoparticles supported on pristine CNF and nanoparticle size histogram after annealing in vacuum (a) at 500˚C for 2 hours, **(b)** at 300˚C for 24 hours and **(c)** at 500˚C for 24 hours. Scale bars are 20, 20 and 50 nm, respectively.*

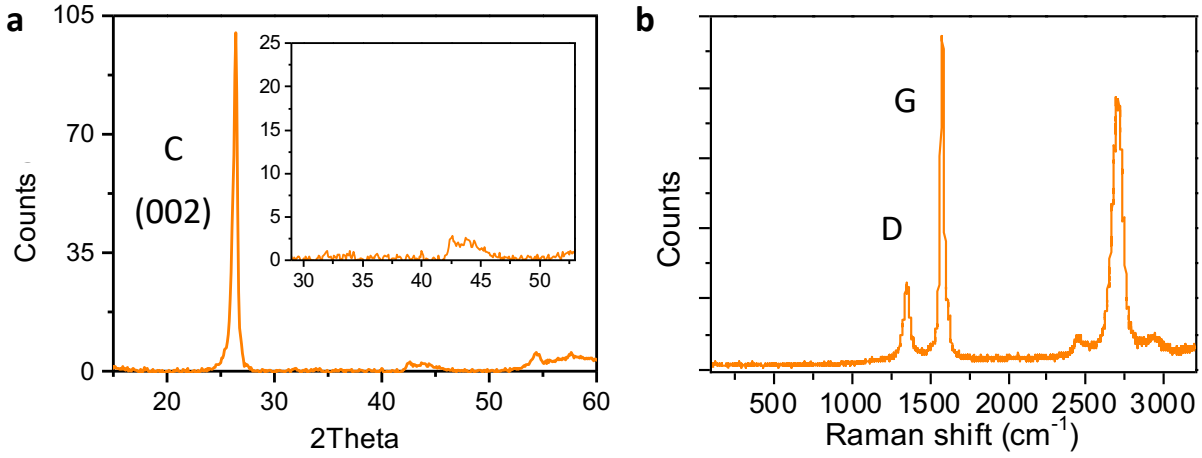

***Figure S 3**. (**a**) Powder XRD pattern for $PdS_x@CNF_m$ showing low crystallinity of very small nanoparticles. (b) Raman spectrum of $PdS_x@CNF_m$ showing D,G,and 2D bands*

2.7.2 Electrochemical

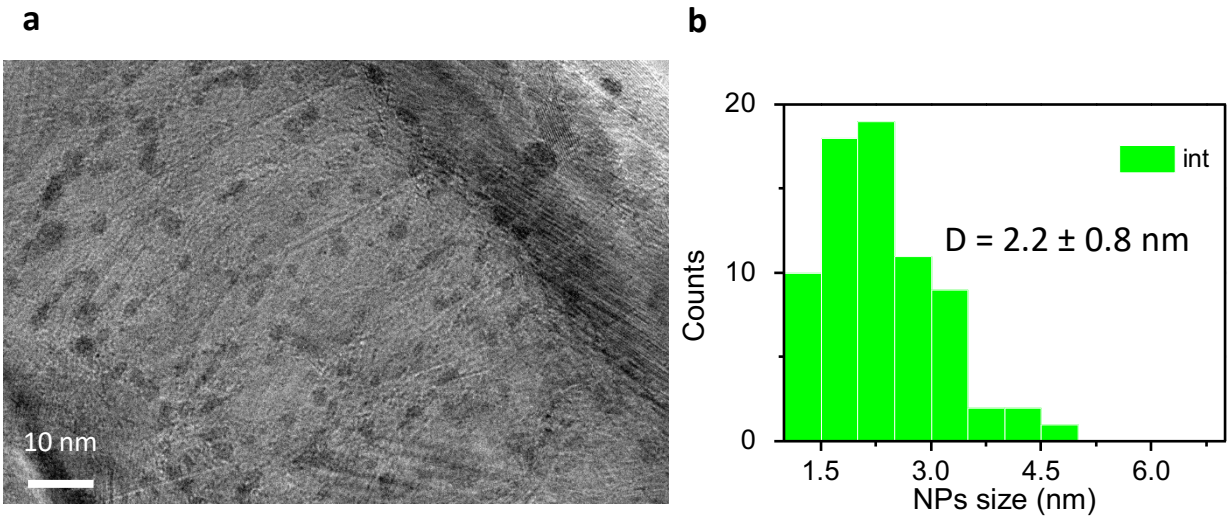

Figure S4. (a) *HRTEM image of PdS_x@CNF_m after 12625 St cycles showing internal particle size is very small due to palladium dissolution and redeposition* ***(b)*** *Particle size distribution histogram D= 2.2 ± 0.8 nm*

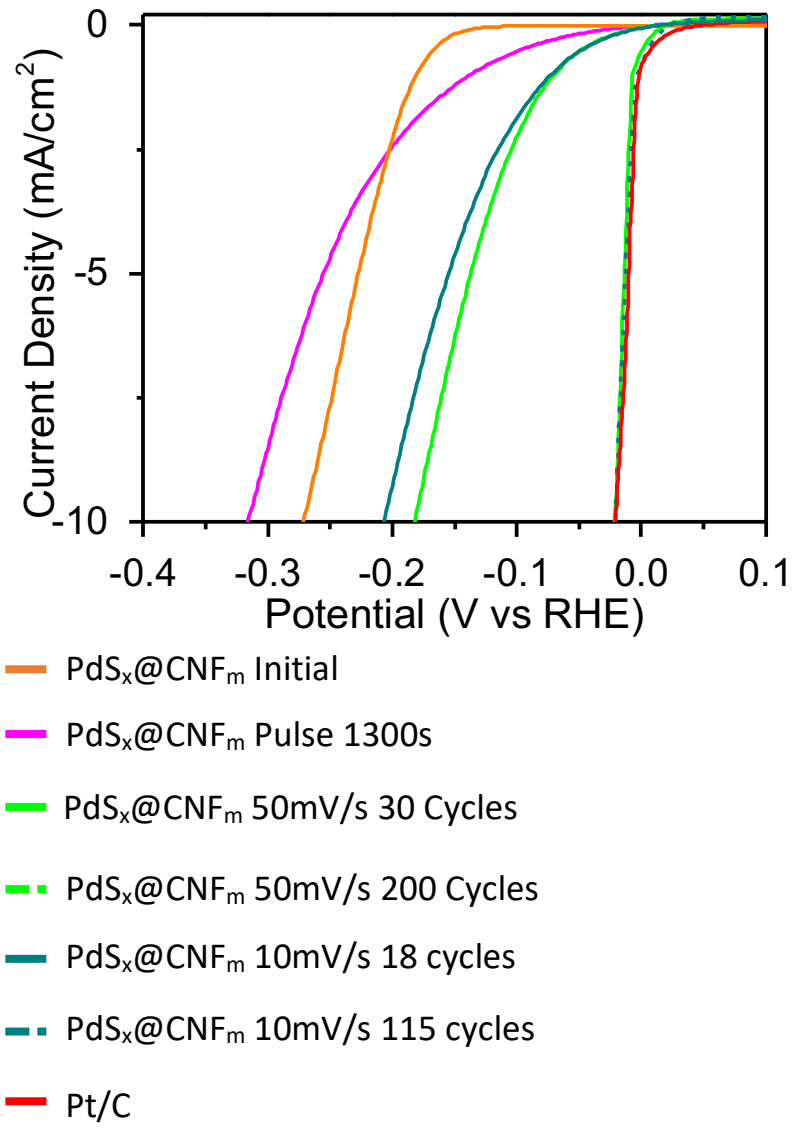

Figure S 5. *HER LSV curves for $PdS_x@CNF_m$ Initial (orange), Pulse (pink), 30 cycles 50mV/s (green), 200 Cycles 50mV/s (green dash), 18 cycles 10mV/s (dark cyan), 115 cycles 10mV/s (dark cyan dash), and Pt/C (red).*

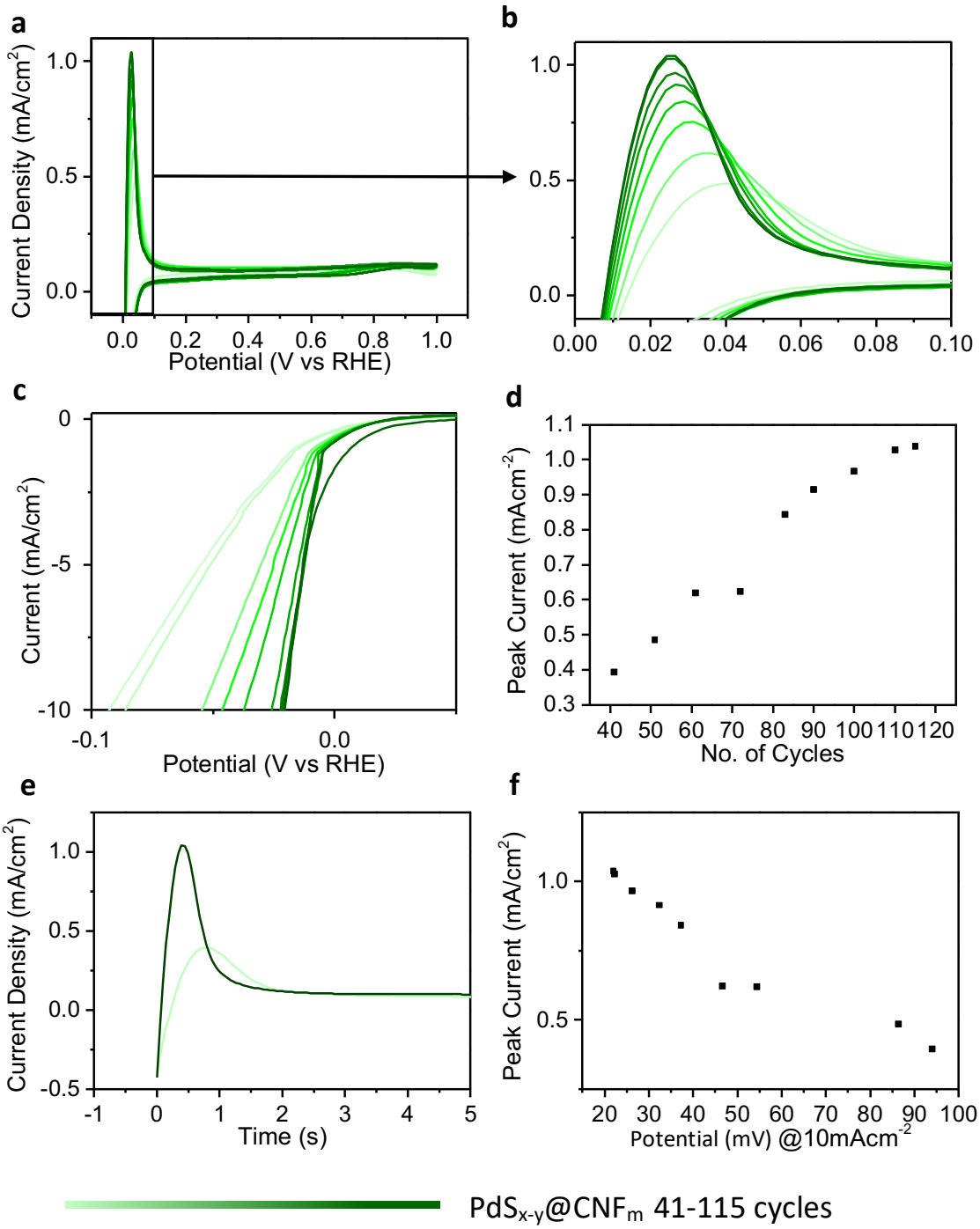

Figure S 6. (a) *CV for PdS$_x$@CNF$_m$ (green) during activation at 10mV/s showing growth of H desorption peak* ***(b)*** *magnification of a* ***(c)*** *corresponding HER LSV for PdS$_x$@CNF$_m$ during activation at 10mV/s* ***(d)*** *plot of peak current against the no. of cycles, showing no correlation between peak area and activation.* ***(e)*** *CV i vs t for PdS$_{x-y}$@CNF$_m$ at 41 (light green) and 115 cycles (black) from which the charge can be determined* ***(f)*** *plot of peak current against η@10 mAcm^{-2}*

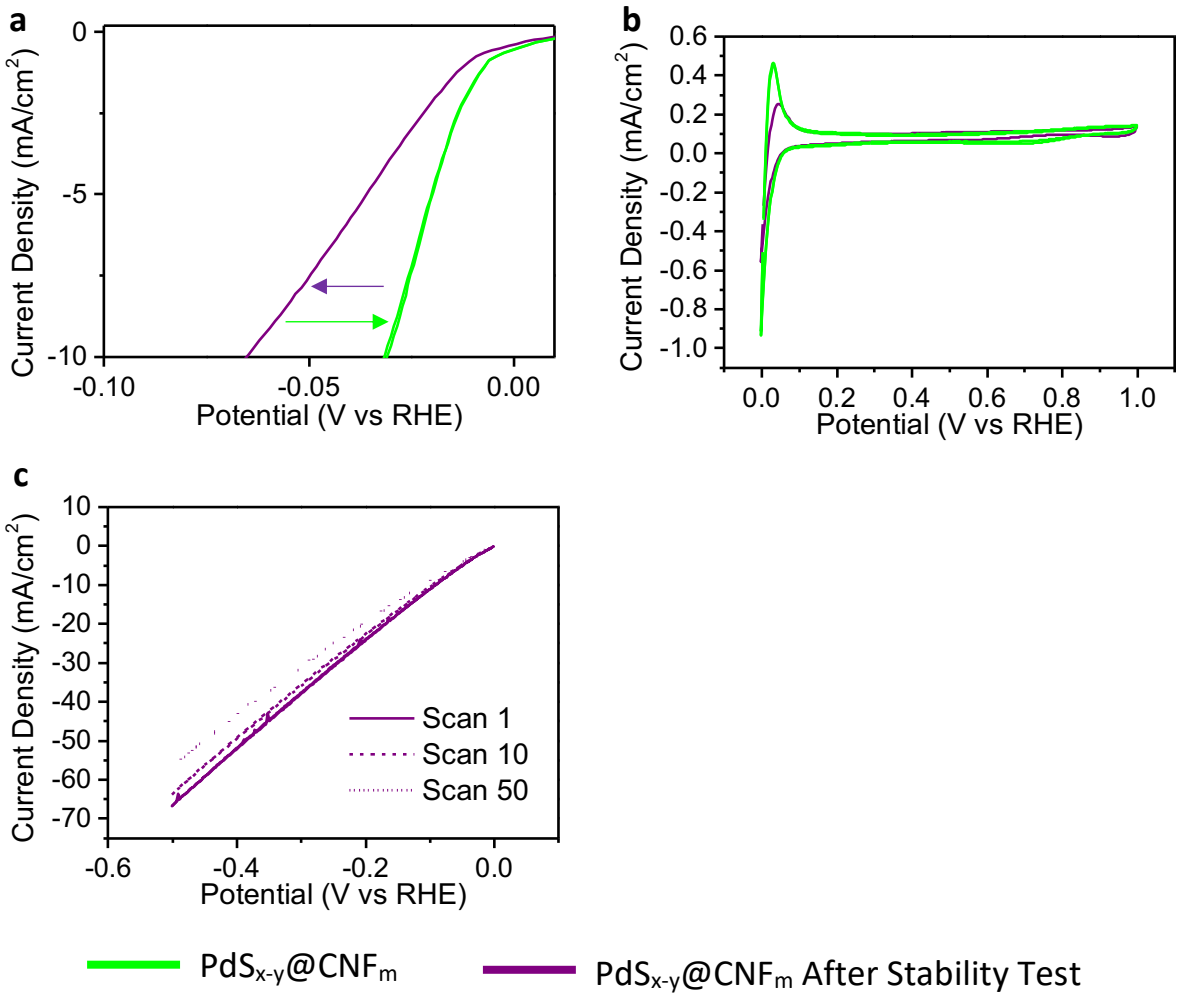

Figure S7 (a) *HER LSV for PdS$_{x-y}$@CNF$_m$ (green) and PdS$_{x-y}$@CNF$_m$ cycled from 0V to -0.5V for 50 cycles (purple)* ***(b)*** *Corresponding CV at each point* ***(c)*** *CV from 0 to -0.5V of PdS$_{x-y}$@CNF$_m$ at scan 1 (purple), scan 10 (purple dash) and scan 50 (purple dot).*

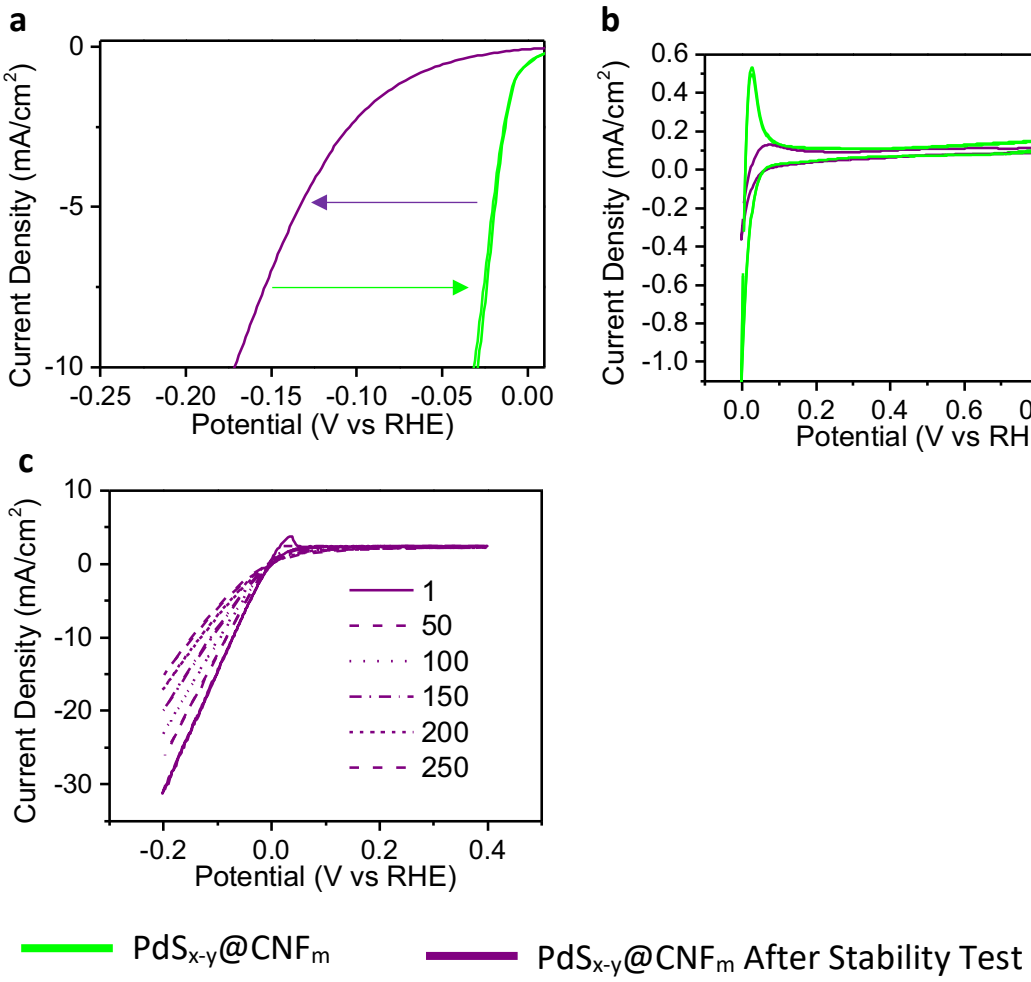

Figure S8 (a) *HER LSV for PdS$_{x-y}$@CNF$_m$ (green) and PdS$_{x-y}$@CNF$_m$ cycled from 0V to -0.5V for 50 cycles (purple)* ***(b)*** *Corresponding CV at each point* ***(c)*** *CV from 0.4 to -0.2V of PdS$_{x-y}$@CNF$_m$ at scan 1 (purple), scan 50 (purple dash) and scan 100 (purple dot), scan 150 (purple dash dot), scan 200 (purple short dash), scan 250 (purple short dash).*

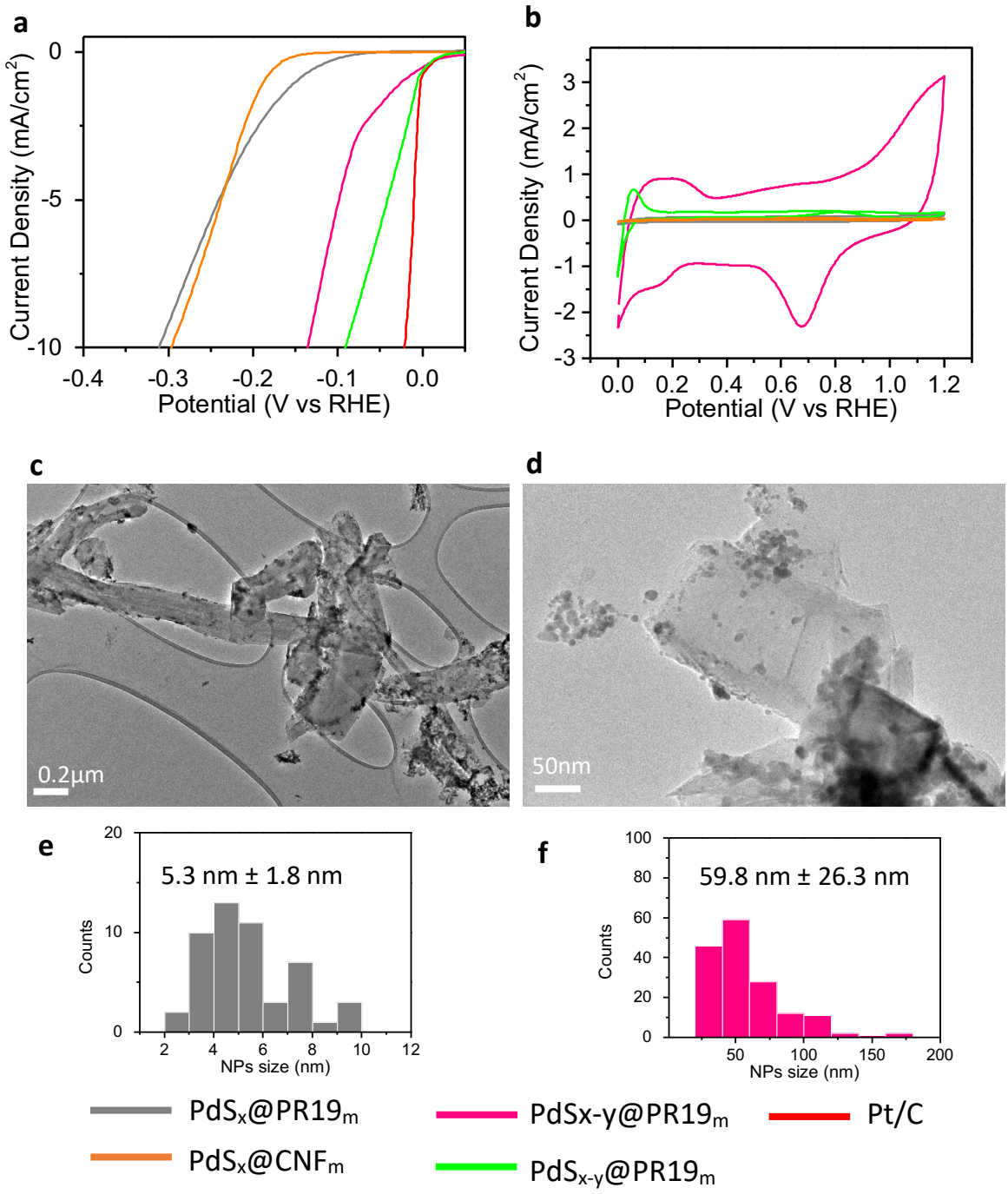

Figure S 9 a) *HER LSV for PdS_x@$PR19_m$ (grey), PdS_{x-y}@$PR19_m$ (ST = 5000) activated (pink), PdS_x@CNF_m (orange), PdS_{x-y}@CNF_m (ST = 4000) (green) and Pt/C (red)* ***(b)*** *CV for PdS_x@$PR19_m$ (grey), PdS_x@CNF_m (orange), PdS_{x-y}@CNF_m (ST = 4000) (green) and PdS_{x-y}@PR19m activated (pink) at 200 mV/s showing significant PdO reduction peaks at 0.7V for activated material* ***(c)*** *HRTEM for PdS_x@$PR19_m$ showing significant different to PdS_x@CNF_m with a much fewer tubular structures remaining intact after milling* ***(d)*** *HRTEM of activated PdS_{x-y}@$PR19_m$* ***(e)*** *Particles size distribution D (5.3 ± 1.8 nm) for PdS_x@$PR19_m$ (grey)* ***(f)*** *Particle size distribution D (59.8 ± 26. nm) for PdS_{x-y}@$PR19_m$ activated (pink) showing significant increase after activation*

Figure S9 shows the use of $PR19_m$ as a much more damaged support with less tubular structures remaining intact after milling. These "smashed" nanofibers reduce the affect of

encapsulation shown in **Figure S9 f** where the particles size distribution has greatly increased, alongside this **Figure S9 b** shows characteristic PdO reduction peaks at 0.7V in the CV at 200mV/s revealing the increased degradation of the PdS_x structure to Pd(0). LSV curves shown ing **Figure S9 a** for the activated material (pink) also have some development of Pd proton absorption peak.

Chapter 3

Synthesis of para-Functionalised m-Terphenyls Towards Immobilisation of Low Coordinate Metal Complexes

3.1 Abstract

This chapter describes the synthesis and characterisation of a set of *m*-terphenyl iodide ligands based on 2,6-$Ar_2C_6H_3I$ where Ar = 2,4,6-$Me_3C_6H_2^-$ (Mes) functionalised at the *para* position of the central aryl ring. With the aim of studying the structural influence on the catalytic or magnetic properties of low-coordinate complexes and their immobilisation on graphitised carbon surfaces. The concept is tested using a phenyl group initially followed by a pyrene moiety to exploit the non-covalent interactions between pyrene and carbon surfaces.

3.2 Introduction

The synthesis of low coordinate metal centres has been undertaken for many reasons; the search for novel compounds, the fundamental understanding of bonding and reactivity, but, more recently the high reactivity of these complexes have been exploited in the area of catalysis.[1–3] The use of 3d transition metals in these complexes has increased to avoid the use of expensive platinum group metals commonly used in catalysis. The stabilisation of low coordinate metal centres is usually achieved through the implementation of sterically demanding ligands, preventing the reactive metal centres from oligomerising with other metal centres or coordinating with Lewis basic ligands. The choice of ligand includes amides, alkyls, silyls, aryls and carbenes which have been previously reviewed.[1–4] The constriction of the coordination sphere in transition metal complexes can impart exciting catalytic and magnetic properties on the resulting complexes including single molecule magnet behaviour, small molecule activation chemistry and catalysis.[3,5–9] These low coordinate metal centres are very reactive and unstable to the presence of water and oxygen making them difficult to work with.

One such class of bulky ligands are *m*-terphenyl ligands with the general formula (C_6H_3-2,6-Ar_2^- where Ar = aryl substituent), providing a steric pocket for the stabilisation of the low coordination number.[10] A significant amount of research has been undertaken in the synthesis and functionalisation of this class of ligand (**Figure 3. 1**) at the flanking aryl R^1 to alter the steric properties, these groups can range from R^1 = H being the most simple terphenyl to more complex groups like mesityl and naphthyl. Functionalisation of the terphenyl at the R^2 buttressing position with *iso*-propyl substituents, *meta* to the complexing

carbon can alter the bite angle of the flanking groups and increase rigidity of the ligand.[11] Finally substitution at the R^3 *para* position has been used to change the electronic properties of the ligand by the inclusion of electron donating or withdrawing groups which can be seen to affect the C–M bond length in the resultant complexes.[12–14] The *para*-position is also an ideal point to add in synthetically useful groups to further extend the ligand in a linear fashion away from the metal/complexing carbon which has been exploited to generate coordination oligomers[15] and polymers.[16]

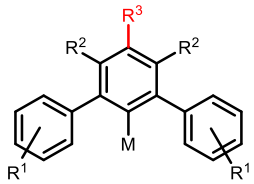

Figure 3. 1 *- m-Terphenyl ligand framework with flanking R^1 (where R^1 can be a combination of groups), buttressing R^2 and para R^3 functionalisation positions*

The R^3 position is an attractive place to functionalise the *m*-terphenyl ligand given its distance from the metal centre reducing direct interaction with the metal centre whilst maintaining the ability to influence the electronic properties of the resulting complexes. There are many methods for anchoring metal complexes to surfaces including covalent bonding, ion-pair association, physisorption (van der Waals interaction), inclusion/entrapment and hydrophobic interactions.[17] The least synthetically demanding route is through non-covalent tethering, as it does not require the full functionalisation of the substrate. One technique of improving catalytic efficiency and recyclability is at the forefront of the heterogeneous homogenous boundary, anchoring of metal complexes shows great promise in improving the effectiveness of a catalyst and has the potential to tackle industrially relevant batch catalyst issue including recoverability.[18] One such method is to exploit the strong π-π interactions between a polyaromatic pyrene unit anchoring to a carbon nanostructure,[19] this method has

been deployed throughout the literature in metal N-heterocyclic carbene complexes of copper,[20] palladium and ruthenium complexes.[21,22] This strategy as of yet has not been applied to low coordinate *m*-terphenyl complexes. Carbon surfaces have been employed as substrates in a multitude of applications, catalysis is no exception.[23] The use of a graphitic carbon substrates for catalyst immobilisation is a convenient route allowing for the use of π-interactions over covalent interactions which require treatment of the substrate surface.[21] Transition metal *m*-terphenyl complexes have recently found application in the cyclotrimerisation of isocyanates,[8] hydrophosphination of isocyanates[9] and the selective reduction and homologation of carbon monoxide.[24] The ability to anchor the Fe(2,6-$Mes_2C_6H_3)_2$ (Mes = 2,4,6-$Me_3C_6H_2$) catalyst could lead to resolving recyclability issues of the catalyst, there may also be significant interest in the magnetic properties of the immobilised materials depicted in **Scheme 3. 1**.

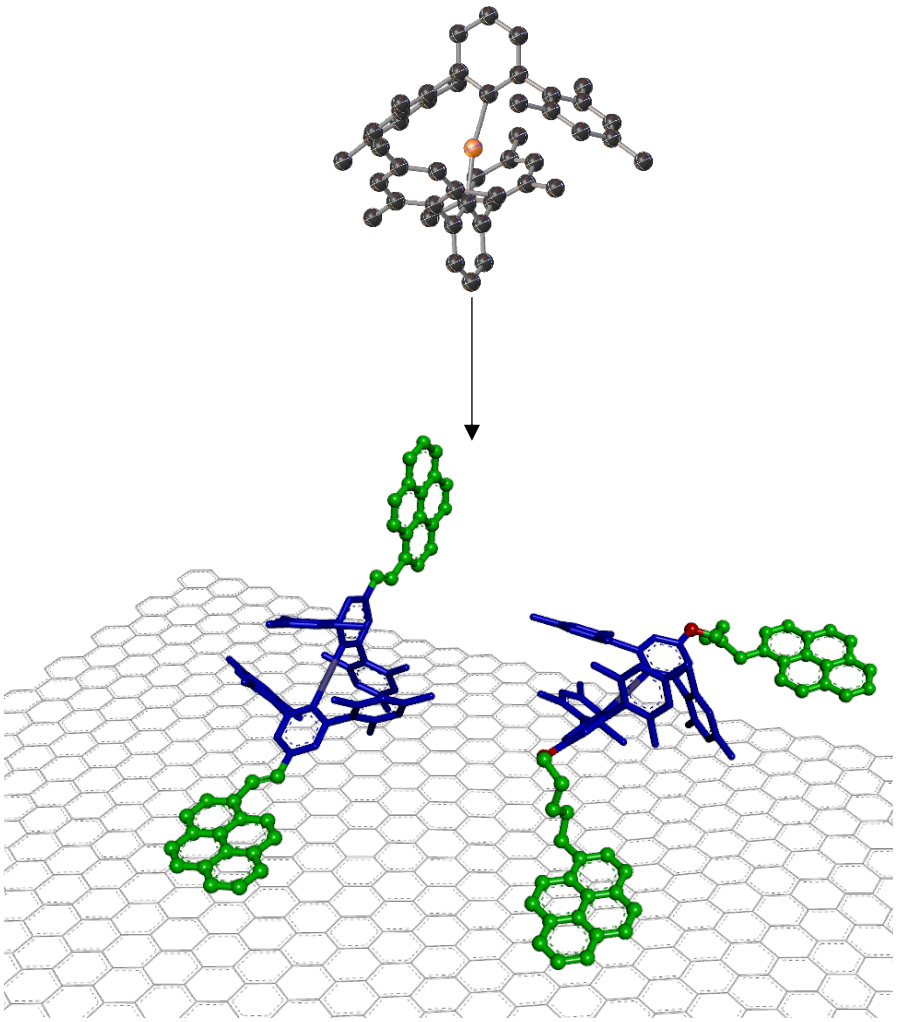

Scheme 3. 1 *Representation of the immobilisation of single molecule properties*[25] *and catalytic properties*[8,24] *of low coordinate metal centres on to carbon sp2 surfaces through π – π interactions between pyrene and graphitic carbon surfaces.*

There are many forms of carbon substrate to choose from including graphene, graphite, single walled carbon nanotubes SWCNTs, multi walled carbon nanotubes MWCNTs, graphitised carbon nanofibers (CNFs). The choice of carbon surface is often determined by the specific requirement of the application, for example the CNF_m chosen for the previous chapter were done so for their extended graphitised structure for efficient electron transfer, folded edges for superior nanoparticle anchoring and hollow structure for encapsulation effects whilst maintaining mass transport. These properties can be beneficial for the catalytic process being targeted, synergistic effects between substrate and adsorbent can increase the accentuate

the properties of the material,[26] which has subsequently been reported to increase catalytic efficacy.[20] This chapter reflects on the choice of anchor, linker group and the synthetic challenges that can be encountered when applying these concepts to the immobilisation of low coordinate metal complexes.

3.3 Experimental

All materials were used as provided unless otherwise stated, the mesityl Grignard synthesis were undertaken under anaerobic conditions using a Schlenk line under an argon atmosphere.

3.3.1 Approach 1 Grignard reaction with a dichloro stilbene/pyrene derivative

Adaptation of the Horner-Wadsworth-Emmons method to generate (*E*) stilbenes used by Protasiewicz *et al*[15] to stabilise low coordinate phosphorus compounds was used to target molecules proposed in **Figure 3. 2**.

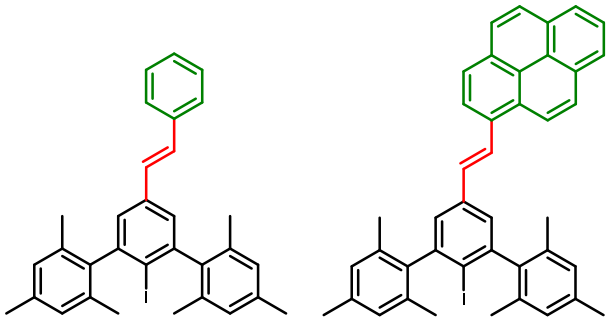

Figure 3. 2 *Stilbene linked target molecules 3,5-(Dimesityl)-4-Iodo-(E)-Stilbene and 3,5-(Dimesityl)-4-iodo-(E)-((styryl)pyrene)terphenyl*

3.3.1.1 Benzylphosphonate[27]

To a stirred solution of ZnI_2 (35.9g, 0.12 mol, 1.5 equiv) in anhydrous toluene was added $P(OEt)_3$ (38.6 mL, 75 mmol equiv) followed by benzyl alcohol (7.76 mL, 75 mmol). The reaction mixture was allowed to stir at reflux overnight (approximately 12 h). After it had cooled to

room temperature, volatiles were removed *in vacuo*. The residue then was washed with 2 M NaOH (250 mL, 0.5 mol) until the solids dissolved, extracted with diethyl ether (200 mL), dried ($MgSO_4$), and concentrated *in vacuo*. The resulting oil was purified *via* flash column chromatography on silica gel to afford the desired diethyl phosphonate (13.3g, 77.7%).

^{1}H NMR (400 MHz, $CDCl_3$) δ_H 1.17 (6 H, td, *J* = 7.0 Hz, 0.6 Hz, **7**), 3.08 (2 H, d, *J* = 21.6 Hz, **5**), 3.94 (4 H, *m*, **6**), 7.14 – 7.25 (5 H, m, **Bz**). ^{13}C NMR (101 MHz, $CDCl_3$) δ_C 16.3 (d, *J* = 5.9 Hz, CH_3 **7**), 33.7 (d, J_{CP} 138.0 Hz, P-CH_2 **5**), 62.0 (d, J_{CP} 6.6 Hz, O-CH_2 **6**), 126.8 (d, J_{CP} 3.7 Hz, CH_{Ar} **1**), 128.4 (d, J_{CP} 3.1 Hz, 2 CH_{Ar} **2**), 129.7 (d, J_{CP} 6.6 Hz, 2 CH_{Ar} **3**), 131.5 (d, J_{CP} 8.9 Hz, C_q **4**) ppm. ^{31}P NMR (162 MHz, $CDCl_3$) δ_P 26.4 ppm. ESI-MS m/z M+H 229.0978.

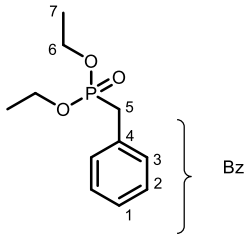

3.3.1.2 (E)-3,5-Dichlorostilbene (1)

To a suspension of potassium tert-butoxide (5.31 g, 46.9 mmol) and 18-crown-6 (*ca* 0.13 g, 0.49 mmol) in THF (75 mL) was added dropwise over 30 minutes a solution of diethyl(benzyl)phosphonate (9.8 g, 43 mmol) and 3,5-dichlorobenzaldehyde (7.5 g, 43 mmol) in THF (75 mL). The mixture was then stirred for 24 h at room temperature, after which time the reaction was quenched by pouring into 10 % methanolic HCl (250 mL). The mixture was filtered and diethyl ether (150mL) and water (150 mL) were added to the filtrate. The organic layer that separated was washed with water (2 $\times$ 150 mL aliquots), neutralized (determined using pH paper) by addition of 5 % sodium hydrogen carbonate solution then rinsed with water (150 mL). Removal of volatiles from the organic solution yielded a sticky yellow solid.

Triturating this solid in hexanes followed by filtration and drying of the solid in vacuo yielded **1** as a pale-yellow powder (5.26 g, 49 %).

^{1}H NMR (400 MHz, $CDCl_3$) δ_H 6.96 (1 H, d, *J* 16.3, **3**), 7.11 (1 H, d, *J* 16.3, **5**), 7.24 (1 H, t, *J* 1.9, **1**), 7.28 – 7.34 (1 H, m, **Bz**), 7.35 – 7.41 (4 H, m), 7.47 – 7.53 (2 H, m) ppm. ^{13}C NMR (101 MHz, $CDCl_3$) δ_C 124.9 (CH, **3**), 126.0 (CH, **5**), 126.9 (2 CH_{Ar}, **Bz**), 127.4 (CH_{Ar}, **1**), 128.6 (CH_{Ar}, **10**), 129.0 (CH_{Ar}, **Bz**), 131.6 (CH, **6**), 135.4 (C_q, **2**), 136.5 (C_q, **4**), 140.5 (C_q, **7**) ppm. ESI-MS m/z M+2H 251.0807.

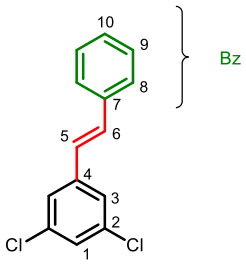

3.3.1.3 3,5-(Dimesityl)-4-Iodo-(E)-Stilbene (2)

Under anaerobic conditions on a Schlenk line a solution of (*E*)-3,5-dichlorostilbene (3.74 g, 15 mmol) in THF (50 mL) was cooled to -78 °C whereupon *n*-BuLi (6 mL, 2.5 m in hexanes, 15 mmol) was added dropwise *via* cannula turning the solution dark red. After 1 hour of stirring at −78 °C, a solution of mesitylmagnesium bromide [prepared by the reaction of 2-bromomesitylene (6.27 g, 31.5 mmol) and Mg turnings (0.92 g, 37.8 mmol) in THF (150 mL)] was added dropwise *via* cannula at −78 °C. After warming to room temperature over a 3 hour period, the solution was stirred under reflux for an additional 10 hours whereupon the reaction mixture became purple. After cooling to room temperature, the flask was placed in an ice bath and iodine (7.6 g, 30 mmol) was added in small portions, additional iodine was

added (5 g, 19.7 mmol). After the exothermic reaction was complete and the characteristic iodine colour persisted in solution for 15 minutes, 5 % Na_2SO_3 (250 mL) was added to quench excess iodine and the solution became yellow. The organic layer was extracted with diethyl ether (250 mL), rinsed with water (2 x 250 mL) and brine. The volatiles were removed to yield an orange oil. The oil was dissolved in hexane and run down a silica plug using hexane to yield two fractions of impurity. The silica was then stripped with EtOAc and **2** was recrystallised from minimum volume of hexane (2.25 g, 27 %).

^{1}H NMR (400 MHz, $CDCl_3$) δ_H 2.07 (12 H, s, **15**), 2.40 (6 H, s, **16**), 7.02 (4 H, s, **13**), 7.08 (1 H, d, *J* 16.3, **5**), 7.19 (1 H, d, *J* 16.3, **6**), 7.29 (2 H, s, **3**), 7.48 – 7.54 (2 H, m) ppm. ^{13}C NMR (101 MHz, $CDCl_3$) δ_C 20.5 (4 CH_3, **15**), 21.4 (2 CH_3, **16**), 106.2 (C^{ipso}, **1**), 125.8 (2 CH_{Ar}, **3**), 126.7 (2 CH_{Ar}, **Bz**), 127.6 (CH, **5**), 128.0 (CH_{Ar}, **Bz**), 128.3 (4 CH_{Ar}, **13**), 128.9 (2 CH_{Ar}, **Bz**), 129.8 (CH, **6**), 135.6 (4 C_q, **1**), 137.1 (C_q, **4**), 137.5 (2 C_q, **14**), 138.2 (C_q, **7**), 141.9 (2 C_q, **11**) 147.6 (2 C_q, **2**) ppm. ESI-MS m/z M+Na 565.1375.

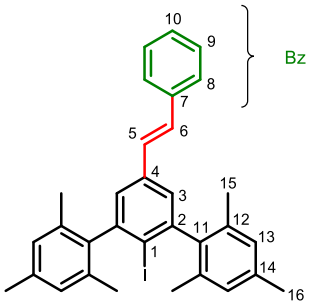

3.3.1.4 3,5-(Dimesityl)-4-Li-(E)-Stilbene (3)

(2.25 g, 4.15 mmol) of **2** was dried *in vacuo*. Hexane (50 mL) was added and the opaque white mixture cooled to –78 °C, *n*BuLi (2.16 mL of 2. 5M in hexanes, 5.4 mmol) was added dropwise with vigorous stirring then left to warm to room temperature. The pale-yellow solution was

filtered and the resulting beige solid of pure product was washed with hexane (20 mL) then dried *in vacuo* affording **3** as a beige solid (1.37 g, 78 %).

^{1}H NMR (400 MHz, C_6D_6) δ_H 1.86 (12 H, s), 2.23 (6 H, s), 6.89 (4 H, s), 7.00 (2 H, s), 7.02 – 7.15 (5 H, m), 7.32 – 7.38 (2 H, m) ppm. ^{7}Li NMR (156 MHz, C_6D_6) δ_{Li} 1.61 ppm.

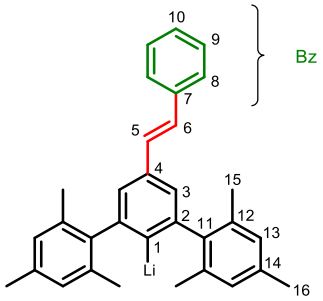

3.3.1.5 Diethyl(3,5-dichlorobenzyl)phosphonate (4)

To a stirred solution of ZnI_2 (3.6g, 11.2 mmol 1.5 equiv) in anhydrous toluene was added $P(OEt)_3$ (3.9 mL, 22.8 mmol, 3 equiv.) followed by 3,5-dichlorobenzylmethanol (1.33 g, 7.5 mmol). The reaction mixture was allowed to stir at reflux overnight (approximately 12 h). After it had cooled to room temperature, volatiles were removed *in vacuo* the residue then was washed with 2 N NaOH until the solids dissolved, extracted with diethyl ether (3 x 200 mL), dried over $MgSO_4$ and dried *in vacuo*. The resulting oil was purified *via* distillation to afford **4** (3.08 g, 13 %)

^{1}H NMR (400 MHz, $CDCl_3$) δ_H 1.27 (6 H, t, *J* 7.1, **7**), 3.07 (2 H, d, *J* 21.7, **5**), 4.05 (4 H, dq, *J* 8.3, 7.0, **6**), 7.18 (2 H, t, *J* 2.6, 1.9, **3**), 7.25 (1 H, d, *J* 2.0, **1**) ppm. ^{13}C (101 MHz, $CDCl_3$) δ_C 16.5 (d, *J* 6.2, 2 CH_3, **7**), 33.5 (d, *J* 138.8, CH_2, **5**), 62.5 (d, *J* 7.0, 2 CH_2, **6**), 127.3 (d, *J* 3.6, CH_{Ar}, **1**), 128.4 (d, *J* 6.5, 2 CH_{Ar}, **3**), 135.0 (d, *J* 3.4, 2 C_q, **2**), 135.3 (d, *J* 9.3, C_q, **4**) ppm. ^{31}P (162 MHz, $CDCl_3$) δ_P 24.5 ppm. ESI-MS m/z M+H 297.0206.

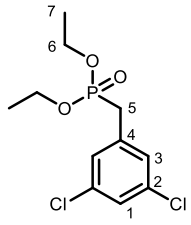

3.3.1.6 (E)-1-(3,5-Dichlorostyryl)pyrene (5)

To a suspension of potassium *tert*-butoxide (1.23 g, 10.9 mmol) and 18-crown-6 (*ca*. 0.03 g, 0.11 mmol) in THF (10 mL) was added dropwise over 30 minutes a solution of di-ethyl(3,5-dichlorobenzyl)phosphonate (2.97 g, 10 mmol) and 1-pyrenecarboxaldehyde (2.30 g, 10 mmol) in THF (10 mL), with additional THF added to aid mixing (ca. 100 mL). The mixture was then stirred for 24 h at room temperature, after which time the reaction was quenched by pouring into 10 % methanolic HCl (50 mL). The mixture was filtered and diethyl ether (300 mL) and water (300 mL) were added to the filtrate. The organic layer that separated was washed with water (2 $\times$ 300 mL), neutralized (determined using pH paper) by addition of 5 % sodium hydrogen carbonate solution then rinsed with water (300 mL). Removal of volatiles from the organic solution yielded a sticky yellow solid. Triturating this solid in hexanes followed by filtration and drying of the solid *in vacuo* yielded the product as a bright yellow powder (1.46 g, 39.2%).

^{1}H NMR (400 MHz, $CDCl_3$) δ_H 7.19 (1 H, d, *J* 16.0, **5**), 7.30 (1 H, t, *J* 1.9, **1**), 7.53 (2 H, d, *J* 1.8, **3**), 7.99 – 8.29 (10 H, m, **Py**), 8.46 (1 H, d, *J* 9.3, **6**) ppm. ^{13}C NMR (101 MHz, $CDCl_3$) δ_C 122.9 (CH_{Ar}, **Py**), 123.8 (CH_{Ar}, **Py**), 125.0 (C_q, **Py**), 125.1 (2 CH_{Ar}, **3**), 125.2 (C_q, **Py**), 125.3 (CH_{Ar}, **Py**), 125.5 (CH_{Ar}, **Py**), 125.7 (CH_{Ar}, **Py**), 126.3 (CH_{Ar}, **Py**), 127.5 (CH, **6**), 127.6 (CH_{Ar}, **1**), 127.9 (CH_{Ar}, **Py**), 128.2 (CH_{Ar}, **Py**), 128.7 (CH_{Ar}, **Py**), 128.9 (C_q, **Py**), 129.0 (CH, **5**), 130.8 (C_q, **Py**), 131.0 (C_q, **Py**), 131.6 (C_q, **Py**), 131.6 (C_q, **Py**), 135.5 (2 C_q-Cl, **2**), 140.9 (C_q, **Py 7**) ppm.

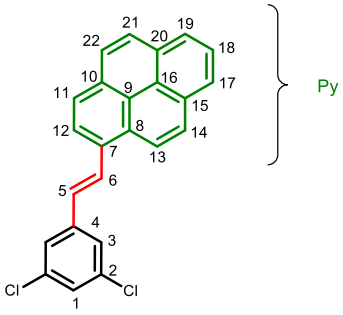

3.3.1.7 3,5-(Dimesityl)-4-iodo-(E)-((styryl)pyrene)terphenyl (6)

A solution of (*E*)-1-(3,5-dichlorostyryl)pyrene (1.86 g, 5 mmol) in THF (50 mL) was cooled to -78 °C whereupon *n*-BuLi (2 mL, 2.5 M in hexanes, 5 mmol) was added dropwise. After 1 hour of stirring at −78 °C, a solution of mesitylmagnesium bromide [prepared by the reaction of 2-bromomesitylene (2.09 g, 10.5 mmol) and Mg turnings (0.31 g, 12.6 mmol) in THF (50 mL)] was added dropwise at −78 °C. After warming to room temperature over a 3 h period, the solution was heated to reflux for an additional 10 h. After cooling to room temperature, the flask was placed in an ice bath and iodine (2.5 g, 10 mmol) was added in 0.5 g portions. After the exothermic reaction was complete and the characteristic iodine colour persisted in solution for 15 minutes, 5 % Na_2SO_3 (250 mL) was added to quench excess iodine and the solution became yellow. The organic layer was extracted with diethyl ether (250 mL), rinsed with water (2 × 250 mL aliquots) and volatiles removed to yield a sticky solid. (0.244 g, 7.3%). The solid was dissolved in boiling hexanes and precipitated at –7 °C to yield the product as a yellow powder.

^{1}H NMR (400 MHz, $CDCl_3$) δ_H 2.10 (12H, s, CH_3, **27**), 2.40 (6 H, s, CH_3, **28**) 6.80 (1 H, d, *J* 6.7 Hz, **Py**), 7.03 (4 H, s, **25**), 7.32 (5 H, d, *J* 16.1 Hz, **Py**), 7.44 (2 H, s, **3**), 7.97 – 8.21 (44 H, m, **Py**), 8.27 (1 H, d, *J* 16.1, **6**), 8.33 (5 H, d, *J* 8.1 Hz), 8.46 (5 H, d, *J* 9.3 Hz) ppm. ^{13}C NMR (101 MHz, $CDCl_3$) δ_C 20.54 (4 CH_3, **27**), 21.43 (2 CH_3, **28**), 106.57 (C_{ipso}, **1**), 123.07 (CH_{Ar}, **Py**), 123.58 (CH_{Ar}, **Py**),

125.1 , 125.2, 125.3, 125.3 , 125.5, 126.0 (2 CH_{Ar}, **3**), 126.2 (CH_{Ar}, **Py**), 126.5 (CH, **6**), 127.6 (CH_{Ar}, **Py**), 127.6, 127.9 (CH_{Ar}, **Py**), 128.3 (4 CH_{Ar}, **25**), 128.7, 129.2 (CH_{Ar}, **Py**), 130.1, 130.5 (CH, **5**), 131.1 (C_q, **Py**), 131.2 (C_q, **Py**), 131.5 (C_q, Py), 131.7 (C_q, **Py**), 135.7 (4 C_q, **24**), 137.6 (2 C_q, **26**), 138.6 (C_q, **7**), 142.0 (2 C, **23**), 147.8 (2 C_q, **2**) ppm.

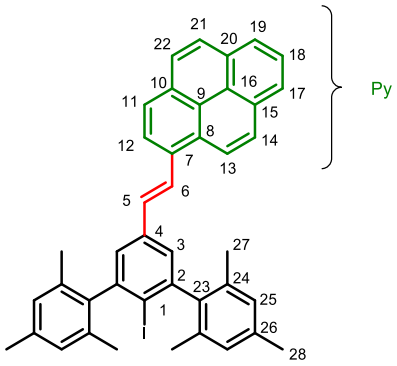

3.3.2 Approach 2 – Ether linkage

Simple S_N2 reactions were used to target ether linked molecules shown in **Figure 3. 3** due to their known stability to Grignard conditions and added flexibility when compared to rigid stilbene double bonds.

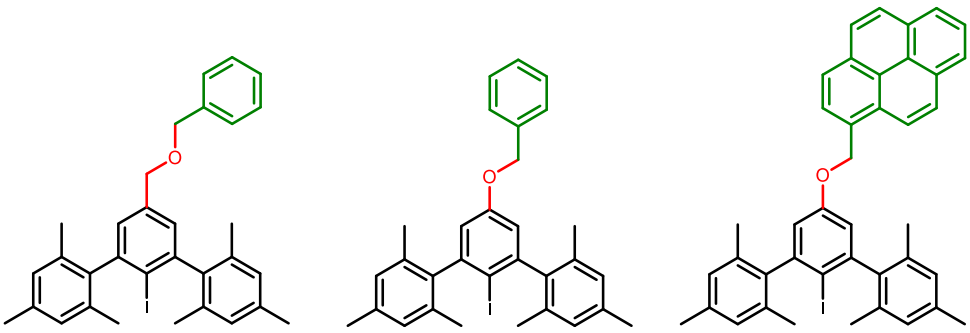

Figure 3. 3 *Ether linked target molecules.*

3.3.2.1 1-((Benzyloxy)methyl)-3,5-dichlorobenzene (7)

3,5-dichlorobenzyl alcohol (1.00 g, 5.65 mmol) was added to a flame dried Schlenck flask under an inert atmosphere. THF was added (20 ml) followed by sodium hydride (0.35 g, 5.65

mmol). The reaction was cooled to 0 °C. After 30 minutes, benzyl bromide (0.67 ml, 5.65 mmol) was added and stirred for 24 h. The reaction was monitored by TLC (90:10 hexane: ethyl acetate). Reaction was quenched with water (25 ml) and extracted with diethyl ether (3 x 25 ml). The organic extracts were washed with brine (25 ml) and dried over $MgSO_4$, filtered and dried *in vacuo*. A brown oil was obtained (0.97 g, 65%). ^{1}H NMR δ_H (400 MHz, $CDCl_3$) δ_H 4.50 (2 H, q, *J* 0.7, **5**), 4.58 (2 H, s, **6**), 7.26 (1 H, d, *J* 1.8, 0.8, **3**), 7.29 (1 H, t, *J* 1.9, **1**), 7.29 – 7.41 (5 H, m, **Bz**) ppm. ^{13}C NMR (101 MHz, $CDCl_3$) δ_C 70.7 (CH_2, **5**), 72.8 (CH_2, **6**), 125.9 (CH_{Ar}, **3**), 127.8 (CH_{Ar}, **1**), 128.0 (2 CH_{Ar}, **Bz**), 128.1 (CH_{Ar}, **Bz-10**) 128.7 (2 CH_{Ar}, **Bz**), 135.1 (2 C_q, **2**), 137.7 (C_q, **7**), 142.0 (C_q, **4**) ppm. ESI-MS m/z M+Na 289.0162.

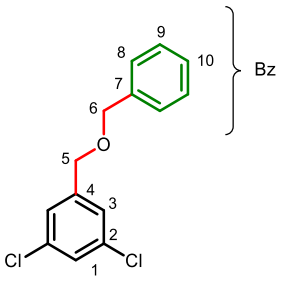

3.3.2.2 5'((benzyloxy)methyl)-4-iodo-(3,5-dimesityl)terphenyl (8)

A solution of 1-((benzyloxy)methyl)-3,5-dichlorobenzene (1.49 g, 5.5 mmol) in THF (50 ml) was cooled (–78 °C). *n*-BuLi (3 ml, 2 M in hexanes, 7.5 mmol) was added dropwise by cannula under an inert atmosphere. After stirring for 1 h MesMgBr (4.36 g, 19.6 mmol) was added dropwise to the reaction mixture. The reaction was left to heat to room temperature for three h, the solution was then stirred at reflux for 10 h. The reaction mixture was then cooled to room temperature, the flask was cooled to 0 °C and iodine added (7.5 g, 30 mmol) in 2.5 g portions. The solution was a dark red, after addition of iodine turned slightly green. 5% Na_2SO_3 (100 mL) was added to the reaction flask, whereupon the solution became bright yellow. Diethyl ether was added (3 × 50 mL) and washed with water (3 x 50 ml). All volatiles were

removed *in vacuo*. A yellow oil was obtained. This was dissolved in boiling hexane and left to crystallise overnight. Crystals formed, but quickly returned back to an oil at room temperature. The oil was eluted through a silica column using 90:10 hexane:ethyl acetate. No product was isolated.

3.3.2.3 (3,5-Dichlorophenoxy)trimethylsilane (9)

3,5-dichlorophenol (8.15 g, 50 mmol) and imidazole (10.2 g, 150 mmol) were dissolved in dichloromethane (200 mL) to produce a yellow solution. The solution was cooled to 0 °C and chlorotrimethylsilane (9.6 mL, 75 mmol) was added, upon addition the reaction mixture a white solid formed. The reaction mixture was stirred for 30 min. The reaction was diluted with diethyl ether and washed with H_2O and brine. The organic extracts were dried with $MgSO_4$, filtered and dried *in vacuo* to yield **9** (7.15 g, 86%). ^{1}H NMR (400 MHz, $CDCl_3$) δ_H 0.40 (9 H, *s,* **5**), 6.87 (2 H, t, *J* 1.7, **3**), 7.10 (1 H, d, *J* 2.0, **1**) ppm. ^{13}C NMR (101 MHz, $CDCl_3$) δ_C 0.2 (2 CH_3, **5**) 119.2 (3 CH_{Ar}, **3**), 122.0 (CH_{Ar}, **1**), 135.2 (C_q, **2**), 156.7 (C_q, **4**) ppm.

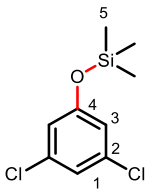

3.3.2.4 4-Iodo (3,5-dimesityl)trimethylsilane (10)

Compound **9** (4.68 g, 20 mmol) was dissolved in THF (200 ml) and cooled to –78 °C and *n*-BuLi (13 ml, 2.5 M in hexanes, 32.5 mmol) was added dropwise. The reaction mixture was stirred at–78 °C for 1 hour. Mesityl magnesium bromide in THF (14.40 g, 65 mmol) was added dropwise at –78 °C for 2 h. After the addition was complete, the reaction mixture was allowed to warm slowly to room temperature. The solution was then stirred at reflux (90 °C) for two

h. Iodine (11.7 g, 45 mmol) was then added at 0 °C and the reaction mixture was refluxed for a further two h. Water was added and excess iodine was quenched with Na_2SO_4. The organic layer was separated and dried over anhydrous $MgSO_4$, filtered and volatiles removed *in vacuo*. Diethyl ether (50 ml) was added to the orange oil and left to slowly recrystallize to produce white crystals. (0.53 g, 5%). ^{1}H NMR (400 MHz, $CDCl_3$) δ_H 2.00 (12 H, s, **9**), 2.34 (6 H, s, **10**), 4.95 (1 H, s, **OH**), 6.64 (2 H, s, **3**), 6.95 (4 H, s, **7**) ppm. ^{13}C NMR (101 MHz, $CDCl_3$) δ_C 20.3 (4 CH_3, **9**), 21.4 (2 CH_3, **10**), 96.6 (C^{ipso}, **1**), 115.8 (2 CH_{Ar}, **3**), 128.2 (4 CH_3, **7**), 135.4 (C_q, **6**), 137.4 (C_q, **8**), 141.7 (C_q, **2**), 148.4 (C_q, **5**), 156.4 (C_q, **4**) ppm.

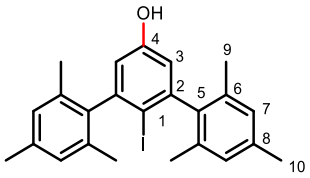

3.3.2.5 (3,5-Dichlorophenoxy)triisopropylsilane (11)

3,5-dichlorophenol (8.15 g, 50 mmol) and imidazole (7.50 g, 110 mmol) were dissolved in DMF (100 mL) to produce a yellow solution. Triisopropylchlorosilane (11.8 ml, 55 mmol) was added dropwise whereupon the reaction mixture turned cream. The reaction mixture was stirred overnight. The reaction was diluted with diethyl ether (200 mL) and washed with H_2O (100 mL) and brine (100 mL). The organic extracts were dried with $MgSO_4$, filtered and volatiles were removed *in vacuo*. Products were then dissolved in petroleum ether and separated using a silicon plug affording **11** (10.6 g, 66.6%).

^{1}H NMR (400 MHz, $CDCl_3$) δ_H 1.11 (18 H, d, *J* 7.2, **6**), 1.20 – 1.31 (3 H, m, **5**), 6.77 (2 H, d, *J* 1.9, **3**), 6.95 (1 H, t, *J* 1.8, **1**) ppm. ^{13}C NMR (101 MHz, $CDCl_3$) δ_C 12.7 (3 CH_2, **5**), 18.0 (6 CH_3, **6**),

119.0 (2 CH_{Ar}, **3**), 121.6 (CH_{Ar}, **1**), 135.2 (2 C_q, **2**), 157.4 (C_q, **4**) ppm. ^{29}Si NMR (79 MHz, $CDCl_3$) δ_{Si} 22.3 ppm.

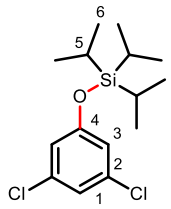

3.3.2.6 4-Iodo (3,5-dimesityl)triisopropylsilane (12)

Compound **11** (4.68 g, 20 mmol) was dissolved in THF (200 ml) and cooled to –78 °C and *n*-BuLi was added dropwise (13 ml, 32.5 mmol), whereupon the reaction mixture was stirred at –78 °C for 1 hour. Mesityl magnesium bromide in THF 30 mL (14.40 g, 65 mmol) was added dropwise at –78 °C for 2 h. After the complete addition, the reaction mixture was allowed to warm slowly to room temperature. The solution was then stirred at reflux (90 °C) for two h. Iodine (11.7 g, 45 mmol) was then added at 0 °C and the reaction mixture was refluxed for a further two h. Water was added and excess iodine was quenched with Na_2SO_4. The organic layer was separated and dried over anhydrous $MgSO_4$, filtered and dried under vacuum. A white powder was obtained (1.517 g, 35.9%)

^{1}H NMR (400 MHz, $CDCl_3$) δ_H 1.08 (18 H, d, *J* 7.0, **6**), 1.16 – 1.28 (3 H, m, **5**), 2.00 (12 H, s, **11**), 2.35 (6 H, s, **12**), 6.70 (2 H, s, **3**), 6.95 (4 H, s, **9**) ppm. ^{13}C NMR (101 MHz, $CDCl_3$) δ_C 12.7 (3 CH, **5**), 18.0 (6 CH_3, **6**), 20.3 (4 CH_3, **11**), 21.4 (2 CH_3, **12**), 97.4 (C_{ipso}, **1**), 120.2 (2 CH_{Ar}, 3), 128.2 (4 CH_{Ar}, **9**) , 135.5 (4 C_q, 8), 137.3 (2 C_q, **10**), 142.0 (2 C_q, **2**), 148.1 (2 C_q, **7**), 157.1 (C_q, **4**) ppm. ESI-MS m/z M+H (613.2328).

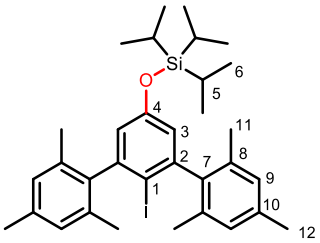

3.4 Discussion

Three routes to a *para*-functionalised *m*-terphenyl iodide ligands were explored with the aim of generating a simple synthetic approach to obtaining these compounds regardless of the anchoring group required in future studies. The criteria set for the synthetic routes are determined by the conditions of the ligand synthesis of the low coordinate *m*-terphenyl complexes. The linker groups must be stable to lithiation and Grignard conditions.

The synthetic pathways were initially tested using a phenyl moiety as a proof of concept with the aim of advancing to a pyrene group as an anchoring group. Previously explored synthetic approaches were incorporated from the literature and expanded upon to generate the new ligands.[15] Purity was confirmed for all ligands *via* ^{1}H and ^{13}C{H} NMR spectroscopy. Route A shown in **Scheme 6** uses a modified version of previously published route by Protasiewicz and co-workers[15] to obtain an alkene linkage with various extended π systems.

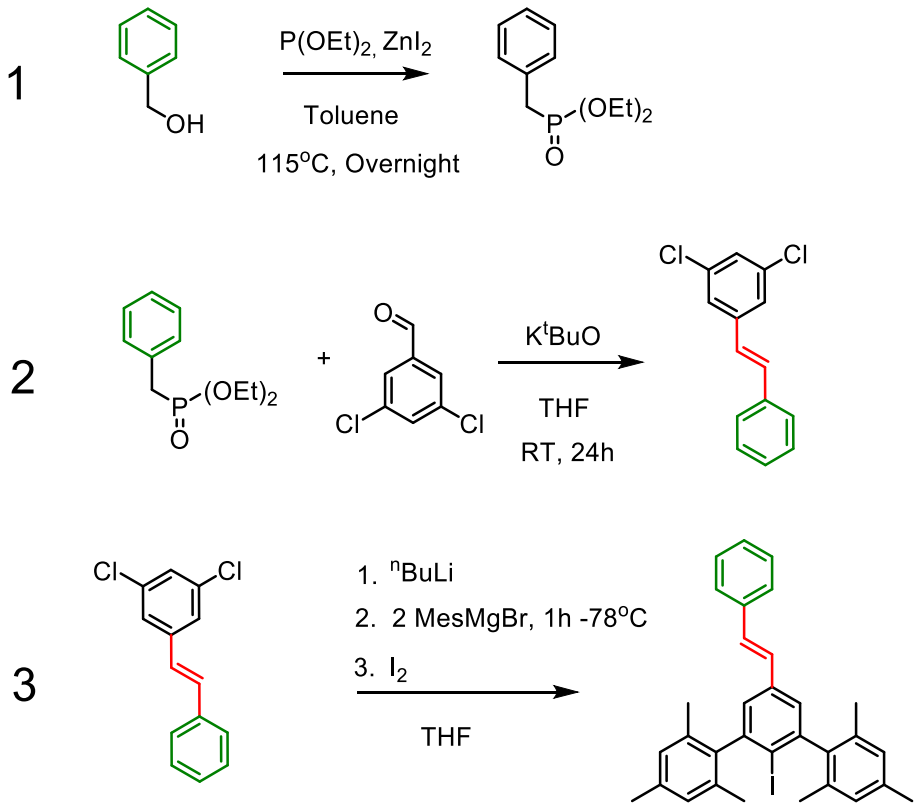

Scheme 3. 2 *Synthesis of alkene linked para functionalised m-terphenyl through steps (**1**) Zn mediated benzyl phosphonate (**2**) Horner-Wadsworth- Emmons reaction of phosphonate and aldehyde (**3**) Modified Hart and co-workers m-terphenyl synthesis*[28]

The synthesis involved the formation of a stabilised phosphonate and subsequent reaction with an aldehyde to form **1**. Compound **1** was then reacted by the modified Hart and co-workers *m*-terphenyl synthesis to produce the *para*-substituted *m*-terphenyl. Synthetic Route **A** was successfully employed for both the phenyl (**Scheme 3. 2**) and pyrene (**Scheme 3. 3**) moieties. The pyrene derivative was difficult to purify resulting in the final compound having a 1-iodomesityl impurity. The pyrene functionalised ligand offers rigidity due to the rotational constraint of the C=C double bond and the potential for electrochemically and photochemically accessible states due to its conjugation. The extended conjugated system may also present some interesting communication of electronic effects from the metal centre once complexed. Further work to synthesise and characterise metal complexes using these ligands is still required.

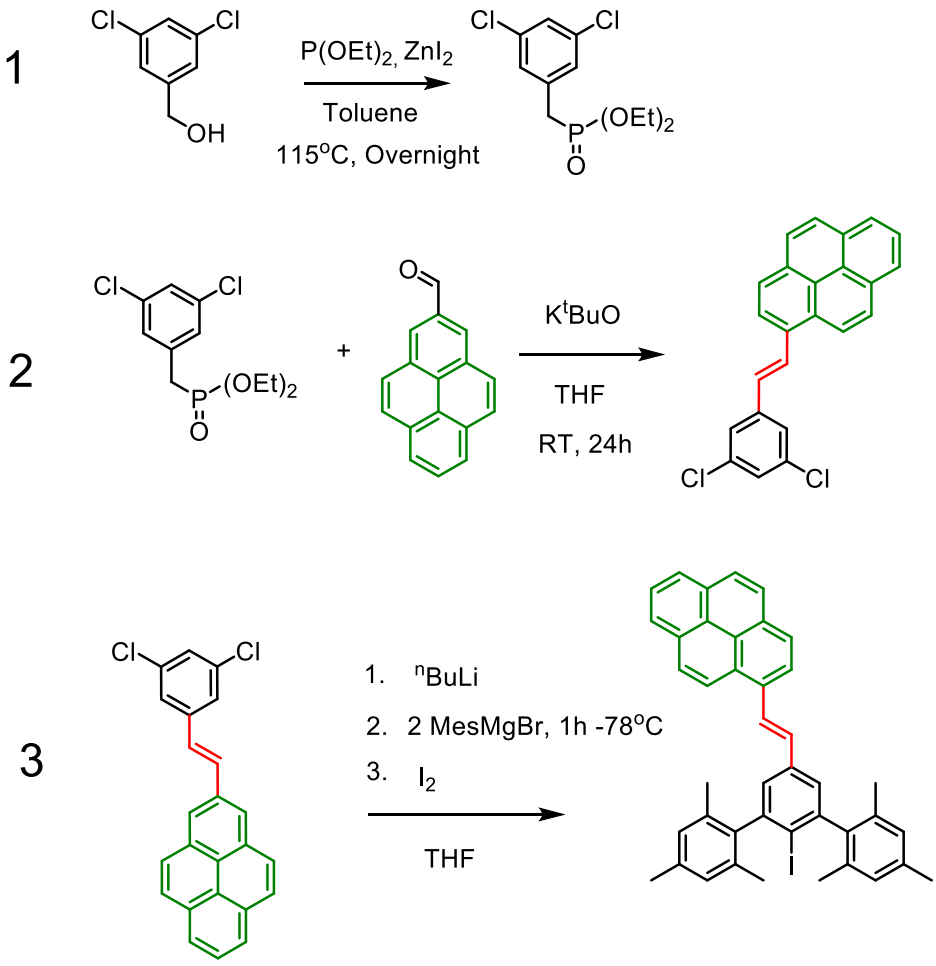

Scheme 3. 3 *Synthetic route A for para substituted m-terphenyl using pyrene moiety (**1**) Zn mediated phosphonate synthesis (**2**)Horner-Wadsworth- Emmons reaction with pyrenecarboxaldehyde (**3**) Modified Hart and co-workers m-terphenyl synthesis*[28]

Synthetic Route **B** (**Scheme 3. 4**) was proposed due to the known stability of ether groups to Grignard conditions and the flexibility of the linker group in contrast with the rigidity of the previous alkene derivative. The low number of steps in the synthesis made it an excellent candidate, however it was not possible to obtain any *m*-terphenyl ligand precursor from the reaction, this is thought to be due to the increased acidity of the benzylic protons adjacent to the ether group.[29] The reaction yielded an insoluble solid and showed no presence of precursor compounds or products in the NMR spectra.

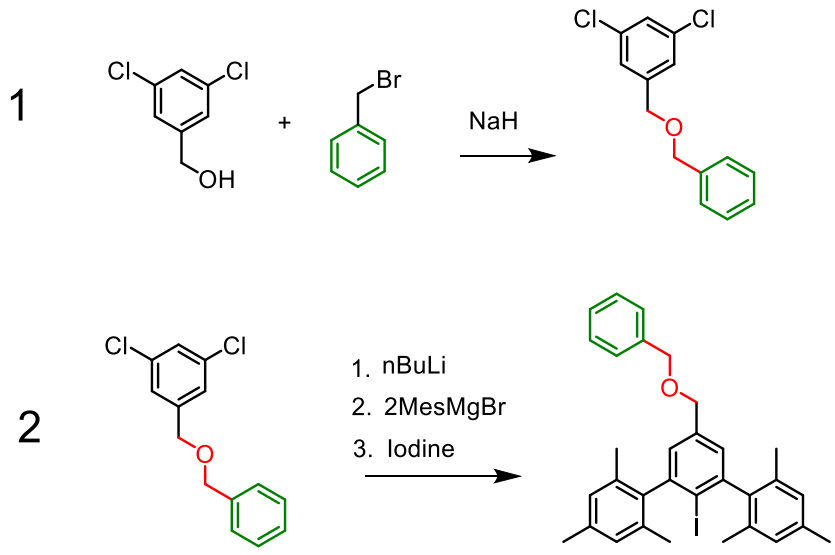

Scheme 3. 4 *Synthetic Route* ***B*** *(**1**)* S_N2 *reaction between alkyl bromide and primary alcohol to form an ether linkage (**2**) Modified Hart and co-workers m-terphenyl synthesis.*[28] *This route was unsuccessful*

The ether linkage remains an attractive candidate to achieve the goals set out in this chapter. A route to the ether linked compound without any benzylic ether protons (Ar-CH_2-O) would be provided by the synthetic Route **C** (**Scheme 3. 5**) utilising the protection of 3,5-dichlorophenol with trialkylsilyl protecting groups (-$SiMe_3$ and -Si^iPr_3). The protected dichlorophenol would then undergo the modified Hart and co-workers *m*-terphenyl synthesis to afford in the case of the trimethylsilyl ether the deprotected para functionalised *m*-terphenyl. The $SiMe_3$ moiety is cleaved by hydrolysis in the reaction mixture during the purification step yielding the unprotected alcohol compound **10**.[13] When using the tri-*iso*-propyl silyl protecting group the desired product is afforded in good yield, the increased steric bulk of the tri-*iso*-propyl group is known to slow down reactions at the silicon and selectively protect primary alcohols in the presence of secondary.[30]

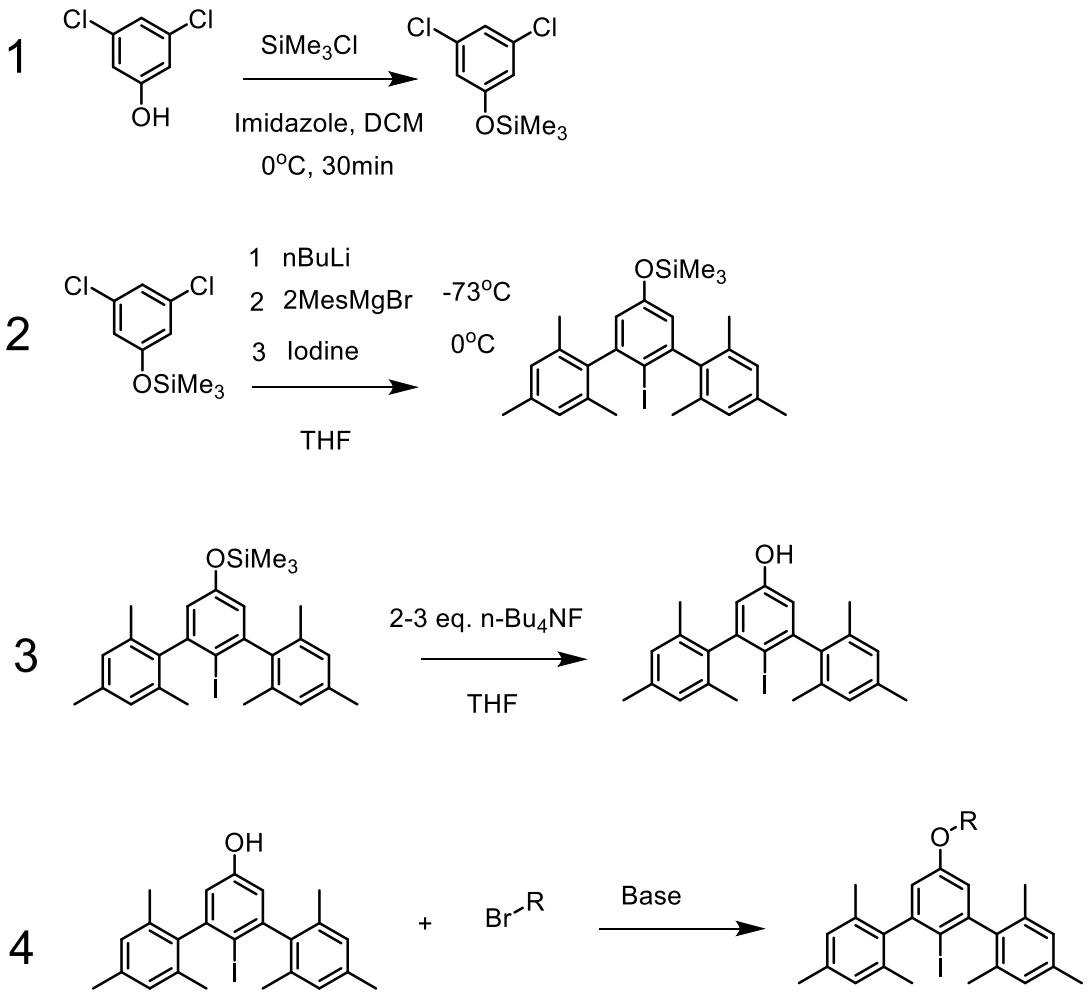

Scheme 3. 5 *Synthetic Route* ***C*** *(**1**) Tertiary silyl ether protection of 3,5-dichlorophenol[30] (**2**) Modified Hart and co-workers m-terphenyl synthesis[28] (**3**) Deprotection of silyl ether m-terphenyl[31] (4) S_N2 reaction between para phenol m-terphenyl and alkyl halide*

3.3.1 NMR Spectroscopic Analysis

All compounds were analysed for purity by ^{1}H and $^{13}C\{^{1}H\}$ NMR spectroscopy. Two distinct singlets are seen in the 1H NMR for mesityl functionalised *m*-terphenyl compounds which can be seen in the spectra for compounds **3**,**6**,**10** and **12,** characteristic doublet and triplets of the *meta* and *para* hydrogens are not observed due to functionalisation at the *para* position. Of interest are the alkene linked *m*-terphenyls compounds **3** and **6** which exhibit these singlets at **3** 2.07 2.40 and **6** 2.10 and 2.40 ppm respectively, both alkene containing compounds have

distinctive shelfed doublets at **3** 7.08, 7.19 which is similar to that reported for the methylstilbene derivative[15] and **6** 7.32**,** 8.27ppm showing the extension of the conjugated system in the form of a pyrene unit has a significant effect on the chemical shift of the alkene. Some further functionalisation of the pyrene or the progress of the ether linked pyrene molecules may provide a better handle to aid in the assignment of these complex NMRs. Compound **10** has two singlets at 2.00 and 2.34 ppm for the two methyl environments on the flanking aryl group, a singlet for the *ortho* hydrogens 6.64 ppm and a singlet for the primary alcohol *para* to the iodine at 4.95 ppm this peak was confirmed to be the alcohol through addition of deuterated water to the NMR sample where proton exchange can then occur and the peak is removed from the spectra. Compound **12** provided a much simpler NMR spectrum due to the unambiguous tri-*iso*-propyl group having a distinct doublet at 1.08 ppm and multiplet at 1.16-1.28 ppm. The two mesityl singlets appear at 2.00 and 2.35ppm with the *ortho* hydrogens at 6.70 ppm. The m-terphenyl iodides exhibit characteristic $^{13}C\{^{1}H\}$ NMR spectroscopic resonances associated with the C^{ipso} C–I bond, **3** 106.27 ppm, **6** 106.57 ppm, **10** - 96.64 ppm, **12** - 97.42 ppm when compared with literature 107.6 ppm for unsubstituted 2,6-dimesityl-iodobenzene the OH and OSiTIP has an electron withdrawing effect causing the C–I bond to be de-shielded compared with the alkene derivatives.

3.3.2 Crystallographic Analysis

Where possible, single crystal X-ray diffraction was used to characterise newly synthesised compounds. Some interesting deductions can be made about the conformation of the pyrene group when compared to the phenyl group. In the solid state, **2** (**Figure 3. 4**) exhibits a planar structure with offset π-π interactions between phenyl rings, centroid-centroid distance of 3.927 Å. Compound **3** crystalises with two molecules in the asymmetric unit cell only one is

shown in **Figure 3. 4**, unlike **2** there are no π-π interactions as this is disrupted by the bulky Mes groups. **3** exhibits a C–I bond length of 2.084(4) Å. Which is similar to the literature values.[32,33]

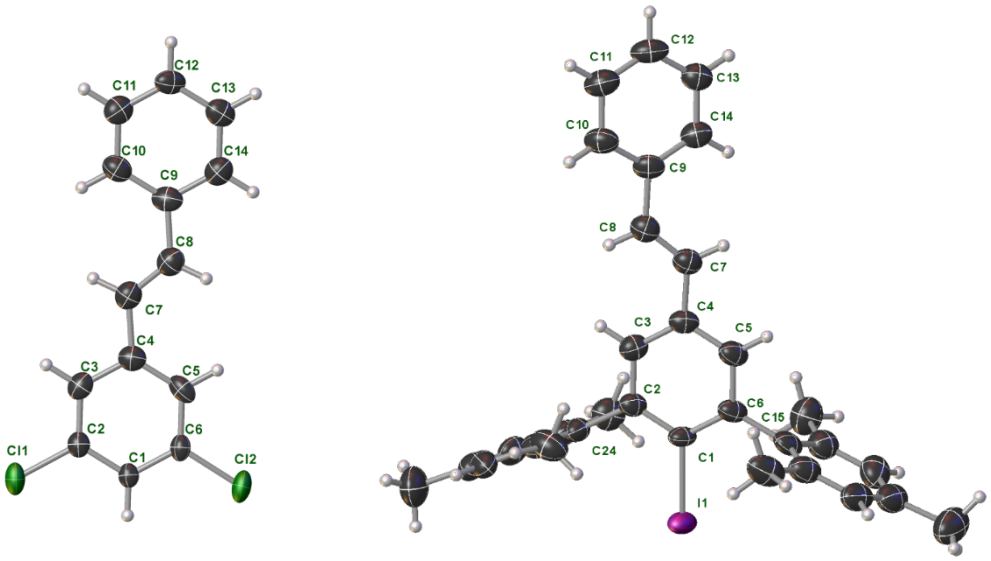

Figure 3. 4 *Single crystal structure of a) dichlorostilbene and b) m-terphenyl with ellipsoids set to 50% thermal probability where C (black), Cl (green), H (white) and I (pink)*

In contrast to **2**, **3** is no longer planar, with a rotation around the C8–C9 bond of 24.5° comparing C9 ring with C1 ring. Compound **5** (**Figure 3. 5a**) has two molecules A and B in the asymmetric unit cell molecule A is essentially planar with a plane-plane torsion angle of 3.7° and B has a plane-plane torsion angle of 25.2° shown in (**Figure 3. 5d**). Both molecules A and B exhibit π-π stacking between benzene and pyrene moieties within the molecules (**Figure 3. 5c**) with centroid-centroid distances of 3.870 Å however the individual molecules are stacked in different conformations molecule A exhibits a graphite like stacking and molecule B exhibits slip stacking shown in **Figure 3. 5b** and **e** respectively.[34]

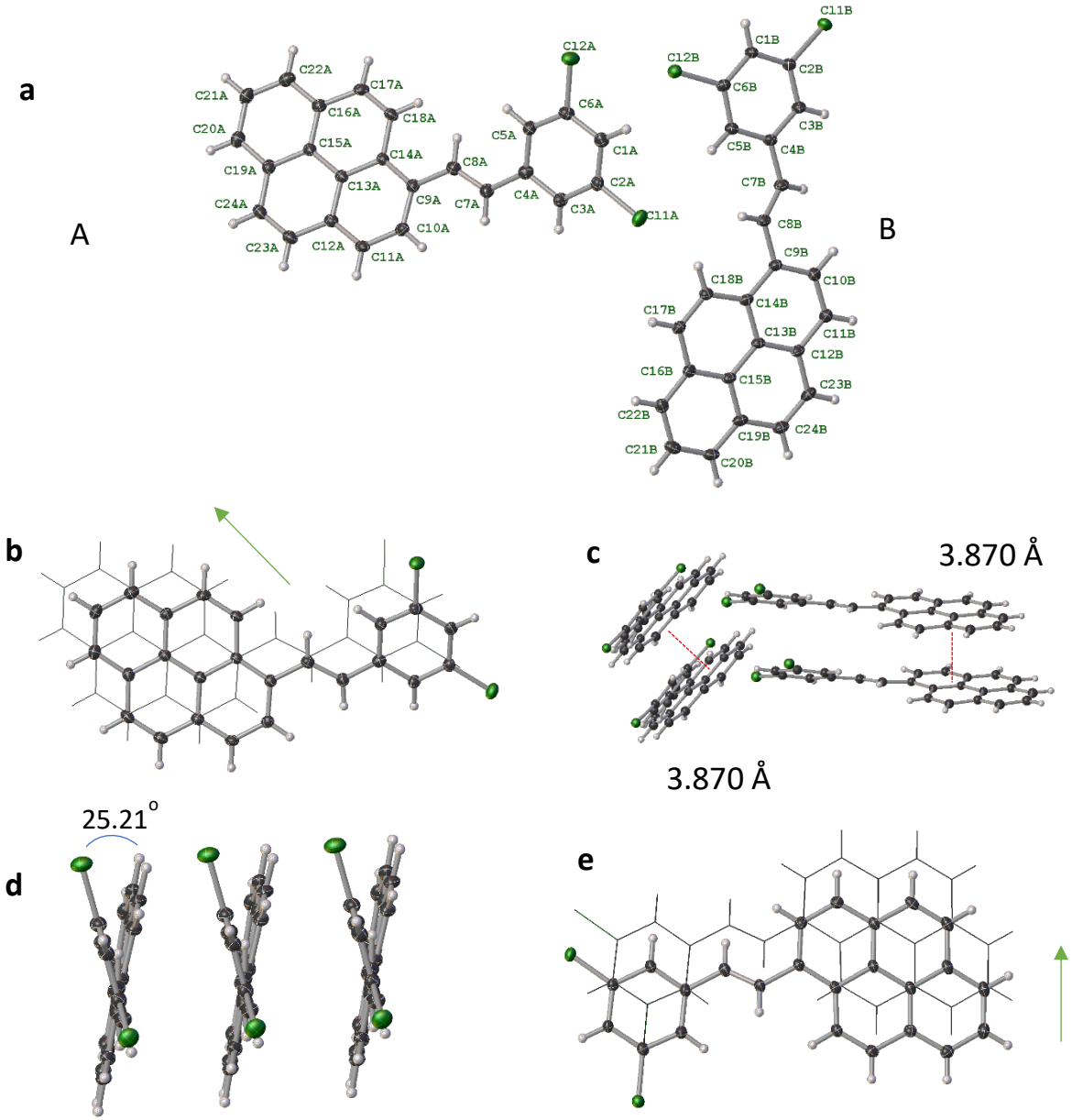

***Figure 3. 5 a**) Asymmetric unit cell for compound **5** viewed 100 plane (**b**) π-π stacking of molecule A showing graphite like conformation (**c**) π-π stacking of A and B with intermolecular distance of 3.870 A (**d**) Molecule A viewed along the pyrene plane showing torsion angle of 25.21°(**e**) π-π stacking showing wire*

Compound **6** has π-π stacking interactions between pyrene groups (**Figure 3. 6**), the π-π stacking interactions are shown in **Figure 3. 6c** in the 100 plane between the pyrene units. If the pyrene is considered as a functionalised aromatic then the conformation can be considered to be T-shaped stacking exhibited by toluene.[35] C–I bond length is 2.103(3) which is consistent with that reported for 2,6-dimesityl-1-iodobenzene 2.102(5).[36]

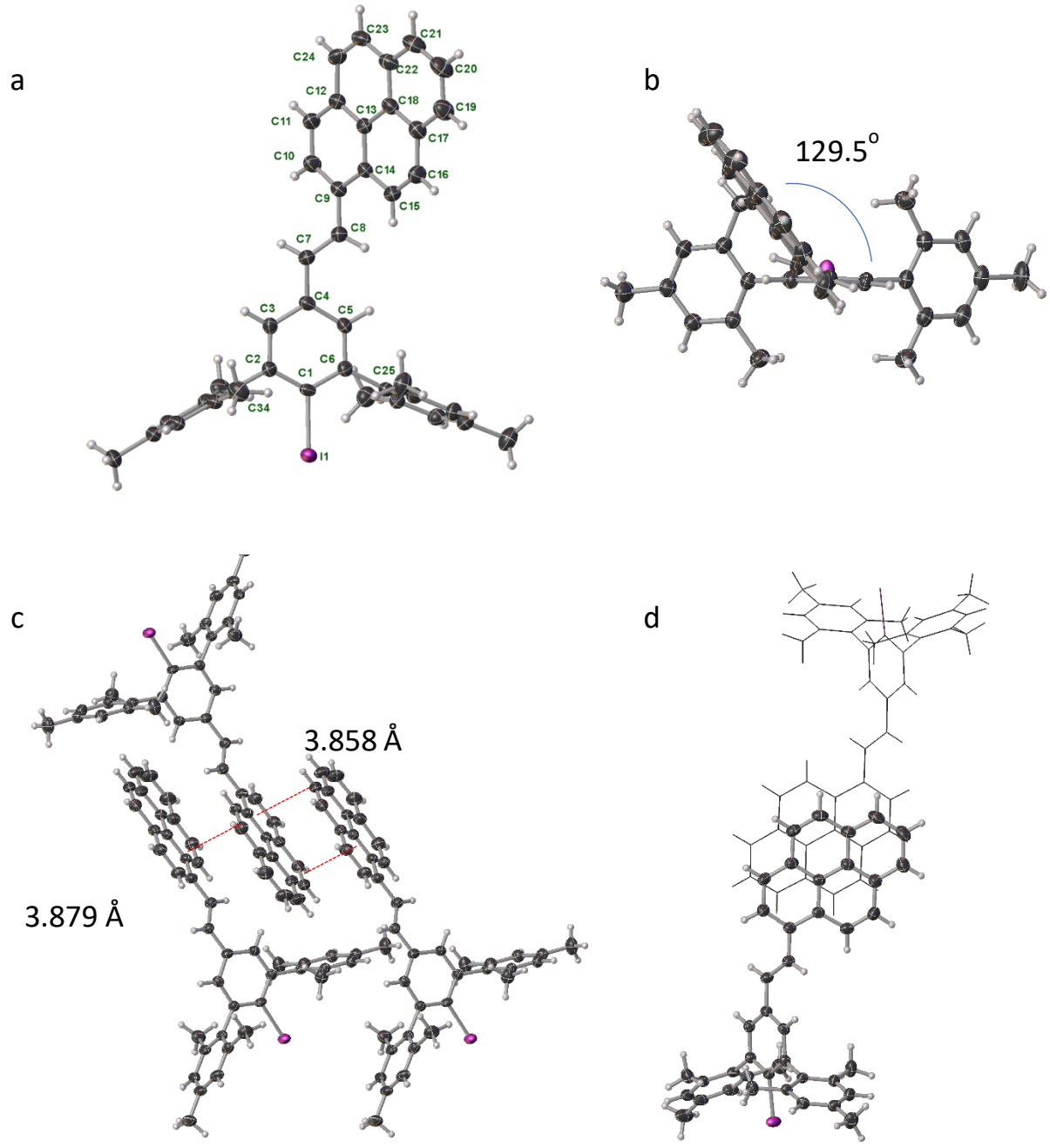

***Figure 3. 6 a**) Asymmetric unit cell of compound **6** (**b**) Torsion angle of the pyrene molecule with respect to the central phenyl group (**c**) Packing diagram of **6** showing the crystallographic 100 plane with π-π interactions shown in red (**d**) π-π interactions viewed down the plane of the pyrene molecule showing the offset conformation.*

The packing conformations shown in **Figure 3. 6c** and **d** are consistent with the literature and depending on the functionalisation of the compounds affect the packing in the solid state for example in a study by *Sharif et al.* where a range of similar 1-(arylalkenyl)pyrenes were synthesised showed that the rotation is caused by steric effects and does not affect the

conjugation of the system.[37] The crystal structures in the paper also show distortion of the π-π stacking dependant on the substituents present.

3.5 Conclusion

It has been possible to successfully synthesise pyrene functionalised *m*-terphenyl iodides through previously reported methods using an alkene linker. The yield for this synthetic route needs some improvement, however it has the potential to move forward to lithiation which was shown by the phenyl derivative and to be complexed with a range of transition metals to afford low coordinate metal centres. Route C utilising silyl ether protecting groups to afford a phenol *m*-terphenyl is very promising for further functionalisation as the link is established after the *m*-terphenyl is synthesised. This will open up a large variety of potential anchoring groups which could be formed from for example alkyl bromides and dibromides used to extend the length of the linker group as shown in previous chapters for tetracarboxylates. The triisopropyl silyl ether protected phenol is stable through the entire *m*-terphenyl synthesis and will require deprotection to afford the phenol. Further work is required to prove the interactions between ligand and carbon nanomaterial, this is a simple next step with the use of UV/Vis and Raman spectroscopy.

3.6 Future Work

This work has produced two successful synthetic routes to para functionalised *m*-terphenyl iodides, moving forward this is a basis to synthesise and investigate a range of bidentate metal complexes. These complexes will have the potential to be tethered to a range of substrates, more specifically graphitic carbon nanostructures. The introduction of two different linker

groups allows for comparative studies based around the flexibility of linker groups and the influence of an extended aromatic system in the form of the stilbene.

3.7 Analytical Techniques

3.6.1 Nuclear Magnetic Resonance Spectroscopy

NMR spectroscopy samples were prepared using standard techniques. For air sensitive materials this included the use of an N_2 atmosphere using J. Youngs tap modified borosilicate glass NMR tubes. All NMR data were collected on Bruker DPX400, AV400, AV(III)400 spectrometers. Chemical shifts are quoted in ppm relative to neat TMS (^{1}H, $^{13}C\{^{1}H\}$, $^{29}Si\{^{1}H\}$, $^{31}P\{^{1}H\}$ and $^{7}Li\{^{1}H\}$).

3.6.2 Mass Spectrometry

ESI-MS measurements were recorded by Dr Mick Cooper (University of Nottingham) on a Bruker Apex4 FTMS using a heptacosafluorotributylamine calibrant.

3.6.3 Single crystal X-ray Diffraction

Single crystals of each material were mounted in Fomblin™ (YR-1800 perfluoropolyether oil) on a MiTeGen MicroMount^{TM}, crystals of **1**,**2** and **6** were frozen in a stream of cold nitrogen using an Oxford Cryosystems open flow cryostat and kept at 120(2) K during data collection. Single crystal x-ray diffraction data were collected on an Agilent SuperNova diffractiometer (mirror-monochromated Cu-Kα radiation source; λ=1.5418; ω scans), equipment with either an Atlas, Atlas S2 or Titan S2 detector. Cell parameters were refined from the observed positions of all strong reflections in each data set and absorption corrections were applied using an Gaussian numerical method with beam profile correction (CrysAlisPro).[38] Using

Olex2, the structure was solved with the ShelXS[39] structure solution program using Direct Methods and refined with the ShelXL[40] refinement package using Least Squares minimisation. Structures were CIF-checked in conjunction with Dr Stephen Argent.

Single crystal x-ray diffraction data of **5** were collected at The diamond light source synchrotron at 100 k beamline I19 (λ=0.6889).[41]

3.6.4 Solvent Preparation

Anhydrous solvents were taken directly from University stills. Prior to use, all solvents were degassed *in vacuo* using standard Schlenk line techniques and then stored over a potassium mirror (diethyl ether) or 4Å molecular sieves (THF).

C_6D_6 were dried over potassium in a sealed tube at 90 ^oC for five days before vacuum-transfer to an ampoule containing a potassium mirror.

3.8 Appendices

3.7.1 Crystallographic data

	2	3	5	6
Internal Code	OGMALB2	OGMALD7	OGALMN	OGMALF
Formula	$C_{14}H_{10}Cl_2$	$C_{32}H_{31}I$	$C_{24}H_{14}Cl_2$	$C_{42}H_{35}I$
M_w	249.12	542.47	373.28	666.60
Crystal system	monoclinic	tetragonal	orthorhombic	triclinic
Space group	$P2_1/n$	$I4_1$	$P2_12_12_1$	P-1
Crystal size/mm^3	1.174 × 0.14 × 0.058	0.117 × 0.093 × 0.043	Na	0.284 × 0.167 × 0.036
a/Å	17.0261(12)	27.1304(5)	3.86991(7)	8.2182(2)
b/Å	3.9271(3)	27.1304(5)	15.0908(2)	8.6968(2)
c/Å	17.4777(13)	14.9712(4)	56.9013(10)	22.8331(6)
α/°	90	90	90	99.742(2)
β/°	94.721(7)	90	90	93.905(2)
γ/°	90	90	90	98.759(2)
V/$Å^3$	1164.65(15)	11019.7(5)	3323.04(10)	1582.24(7)
Z	4	16	15	2
T	120(2)	120(2)	100(2)	120(2)
$\rho_{calc}g/cm^3$	1.421	1.308	1.492	1.399
μ/mm^{-1}	4.721	9.234	0.365	8.153
F_{000}	512.0	4416.0	1536.0	680.0
Radiation	CuKα (λ = 1.54184)	Cu Kα (λ = 1.54184)	Synchrotron (λ = 0.6889)	CuKα (λ = 1.54184)
2Θ range for data collection/°	6.968 to 147.08	6.516 to 147.222	2.962 to 58.93	10.468 to 146.838

Index ranges	-20 ≤ h ≤ 21, -3 ≤ k ≤ 4, -21 ≤ l ≤ 19	-33 ≤ h ≤ 28, -32 ≤ k ≤ 32, -18 ≤ l ≤ 18	-5 ≤ h ≤ 5, -21 ≤ k ≤ 21, -81 ≤ l ≤ 81	-10 ≤ h ≤ 10, -10 ≤ k ≤ 6, -28 ≤ l ≤ 27
Reflections collected	3917	25116	57581	13439
Independent reflections	2254 [R_{int} = 0.0365, R_{sigma} = 0.0368]	10819 [R_{int} = 0.0374, R_{sigma} = 0.0430]	10169 [R_{int} = 0.1242, R_{sigma} = 0.0786]	6016 [R_{int} = 0.0595, R_{sigma} = 0.0531]
Data/restraints/parameters	2254/0/121	10819/1999/899	10169/0/209	6016/0/394
Goodness-of-fit on F^2	2.014	1.056	1.193	1.033
Final R indexes [I>=2σ (I)]	R_1 = 0.1377, wR_2 = 0.4356	R_1 = 0.0349, wR_2 = 0.0792	R_1 = 0.0759, wR_2 = 0.1853	R_1 = 0.0443, wR_2 = 0.1121
Final R indexes [all data]	R_1 = 0.1446, wR_2 = 0.4476	R_1 = 0.0409, wR_2 = 0.0834	R_1 = 0.0994, wR_2 = 0.2249	R_1 = 0.0537, wR_2 = 0.1159
Largest diff. peak/hole / e $Å^{-3}$	2.52/-0.81	0.38/-0.31	0.95/-1.08	0.89/-1.58

3.8 References

1 P. P. Power, *J. Organomet. Chem.*, 2004, **689**, 3904–3919.

2 D. L. Kays, *Dalton Trans.*, 2011, **40**, 769–778.

3 L. J. Taylor and D. L. Kays, *Dalton Trans.*, 2019, **48**, 12365–12381.

4 D. L. Kays, *Chem. Soc. Rev.*, 2016, **45**, 1004–1018.

5 D. E. Freedman, W. H. Harman, T. D. Harris, G. J. Long, C. J. Chang and J. R. Long, *J. Am. Chem. Soc.*, 2010, **132**, 1224–1225.

6 M. S. Fataftah, J. M. Zadrozny, D. M. Rogers and D. E. Freedman, *Inorg. Chem.*, 2014, **53**, 10716–10721.

7 E. Bill, *Nat. Chem.*, 2013, **5**, 556–557.

8 H. R. Sharpe, A. M. Geer, H. E. L. Williams, T. J. Blundell, W. Lewis, A. J. Blake and D. L. Kays, *Chem. Commun.*, 2017, **53**, 937–940.

9 H. R. Sharpe, A. M. Geer, W. Lewis, A. J. Blake and D. L. Kays, *Angew. Chem. Int. Ed.*, 2017, **56**, 4845–4848.

10 T. J. Blundell, F. R. Hastings, B. M. Gridley, G. J. Moxey, W. Lewis, A. J. Blake and D. L. Kays, *Dalton Trans.*, 2014, **43**, 14257–14264.

11 B. D. Rekken, T. M. Brown, J. C. Fettinger, F. Lips, H. M. Tuononen, R. H. Herber and P. P. Power, *J. Am. Chem. Soc.*, 2013, **135**, 10134–10148.

12 P. Wilfling, K. Schittelkopf, M. Flock, R. H. Herber, P. P. Power and R. C. Fischer, *Organometallics*, 2015, **34**, 2222–2232.

13 E. Rivard, R. C. Fischer, R. Wolf, Y. Peng, W. A. Merrill, N. D. Schley, Z. Zhu, L. Pu, J. C. Fettinger, S. J. Teat, I. Nowik, R. H. Herber, N. Takagi, S. Nagase and P. P. Power, *J. Am. Chem. Soc.*, 2007, **129**, 16197–16208.

14 A. Falceto, K. H. Theopold and S. Alvarez, *Inorg. Chem.*, 2015, **54**, 10966–10977.

15 R. C. Smith and J. D. Protasiewicz, *Eur. J. Inorg. Chem.*, 2004, 998–1006.

16 R. C. Smith and J. D. Protasiewicz, *J. Am. Chem. Soc.*, 2004, **126**, 2268–2269.

17 J. M. Fraile, J. I. García and J. A. Mayoral, *Chem. Rev.*, 2009, 109, 360–417.

18 S. Hübner, J. G. De Vries and V. Farina, *Adv. Synth. Catal.*, 2016, **358**, 3–25.

19 V. Georgakilas, M. Otyepka, A. B. Bourlinos, V. Chandra, N. Kim, K. C. Kemp, P. Hobza, R. Zboril and K. S. Kim, *Chem. Rev.*, 2012, **112**, 6156–6214.

20 P. Ballestin, D. Ventura-Espinosa, S. Martín, A. Caballero, J. A. Mata and P. J. Pérez, *Chem. Eur. J.*, 2019, **25**, 9534–9539.

21 S. Sabater, J. A. Mata and E. Peris, *Organometallics*, 2015, **34**, 1186–1190.

22 D. Ventura-Espinosa, C. Vicent, M. Baya and J. A. Mata, *Catal. Sci. Technol.*, 2016, **6**, 8024–8035.

23 A. Schaetz, M. Zeltner and W. J. Stark, *ACS Catal.*, 2012, **2**, 1267–1284.

24 H. R. Sharpe, A. M. Geer, L. J. Taylor, B. M. Gridley, T. J. Blundell, A. J. Blake, E. S. Davies, W. Lewis, J. McMaster, D. Robinson and D. L. Kays, *Nat. Commun.*, 2018, **9**, 1–8.

25 J. M. Zadrozny, D. J. Xiao, M. Atanasov, G. J. Long, F. Grandjean, F. Neese and J. R. Long, *Nat. Chem.*, 2013, **5**, 577–581.

26 J. Lee, E. Hwang, E. Lee, S. Seo and H. Lee, *Chem. Eur. J.*, 2012, **18**, 5155–5159.

27 R. J. Barney, R. M. Richardson and D. F. Wiemer, *J. Org. Chem.*, 2011, **76**, 2875–2879.

28 C. J. F. Du, H. Hart and K. K. D. Ng, *J. Org. Chem.*, 1986, **51**, 3162–3165.

29 H. Gilman, A. H. Haubein and H. Hartzfeld, *J. Org. Chem.*, 1954, **19**, 1034–1040.

30 C. Rücker, *Chem. Rev.*, 1995, **95**, 1009–1064.

31 R. A. Fernandes, S. P. Gholap and S. V. Mulay, *RSC Adv.*, 2014, **4**, 16438–16443.

32 M. Niemeyer, *Organometallics*, 1998, **17**, 4649–4656.

33 N. J. H. and P. P. P. Brendan Twamley, *Acta Crys.*, 2000, **56**, e514–e515.

34 E. M. Cabaleiro-Lago and J. Rodríguez-Otero, *ACS Omega*, 2018, **3**, 9348–9359.

35 C. R. Martinez and B. L. Iverson, *Chem. Sci.*, 2012, **3**, 2191–2201.

36 J. D. P. L.N.Zakharov, A.L.Rheingold, *CSD Commun.*, 2003.

37 M. Sharif, S. Reimann, K. Wittler, L. R. Knöpke, A. E. Surkus, C. Roth, A. Villinger, R. Ludwig and P. Langer, *European J. Org. Chem.*, 2011, 5261–5271.

38 Agilent, 2014, CrysAlis PRO. Agilent Technologies Ltd, Yarnton, O.

39 G. M. Sheldrick, *Acta Crystallogr. Sect. A*, 2008, **64**, 112–122.

40 G. M. Sheldrick, *Acta Crystallogr. Sect. C*, 2015, **71**, 3–8.

41 H. Nowell, S. A. Barnett, K. E. Christensen, S. J. Teat and D. R. Allan, *J. Synchrotron Radiat.*, 2012, **19**, 435–441.

Chapter 4

Magneto-Structural Correlation in Porous Hydrogen Bonded Networks of $Fe(3\text{-}Bpp)^{2+}$ and High Charge Tetracarboxylate Anions

4.1 Abstract

This chapter investigates a range of spin crossover (SCO) materials with large and flexible high charge tetracarboxylate anions (TCA) in the form $[Fe(3\text{-}Bpp)_2]_2[TCA].xH_2O$ (3-Bpp = 2,6-bis(pyrazol-3-yl)pyridine). TCA molecules are synthesised with varying length linker moieties ethyl, pentyl, decyl and *p*-xylyl. The final materials are synthesised through a double metathesis reaction between $[Fe(3\text{-}Bpp)][SO_4]$ and the barium salt of the TCA. The resulting materials are characterised through X-ray crystallography and magnetic measurements in order to deduce a structure-function relationship.

4.2 Introduction

Materials with switchable properties are highly desirable in bringing about technological advancement in photonic, mechanical, electronic and spintronic devices as well as sensing applications.[1,2] The ability to store information is based on the ability to switch between two or more distinct and distinguishable states. [3–6]

One set of materials that show great promise in this area are spin crossover materials, these are restricted to the first-row transition metal complexes with d^4-d^7 electronic configuration due to higher d-orbital splitting in second and third row transition metals. Complexes of these first-row transition metals have been extensively investigated with varying ligand environments.[1,7–11] Due to the nature of the d orbital splitting into the t_{2g} and e_g sets by a ligand field these materials can exhibit either low spin (LS) or high spin (HS) states.[7] A transition between the LS and HS states can be promoted by an external perturbation most commonly temperature,[12] light irradiation,[12,13] potential or pressure.[14–16] but can include applied magnetic field[17] and x-ray irradiation.[18,19]

The most common spin crossover species are that of iron(II) d^6 with $t_{2g}^4e_g^2$ configuration in which a transition occurs between the diamagnetic LS $^1A_1$ where (S = 0) and the paramagnetic HS $^5T_2$ where (S = 2), the phenomenon is most easily described by the crystal field splitting diagram **Figure 4. 1**. The energy or temperature range in which the spin transition occurs can be tuned by the strength of the ligand field, a strong ligand field favours the HS and a weak ligand field favours the LS. When the ligand field force coincides with the electron pairing energy the $\Delta E_{LS\text{-}HS}$ is small enough to be overcome by an external perturbation. The energy

range or temperature at which a transition will occur can be tuned by the ligand environment which is a combination of M-L σ- and π-bonding interactions.[20]

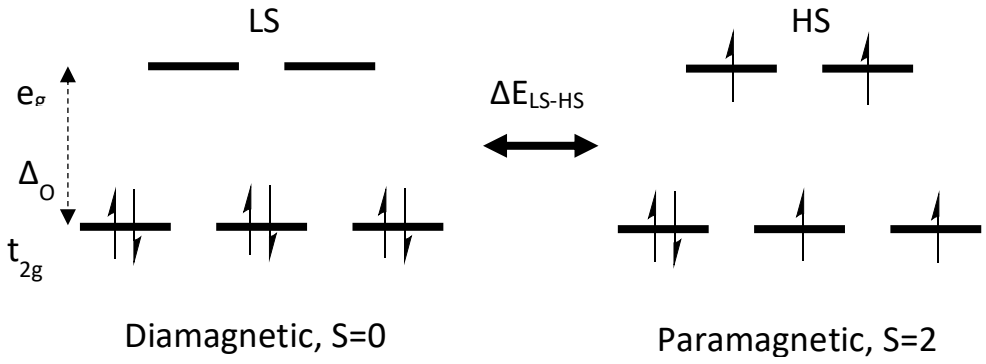

Figure 4. 1 *Crystal splitting diagram showing a spin transition in octahedral Fe(II) d^6 compound*

In the solution phase spin transitions tend to be non-cooperative and occur over a wide temperature range, so each individual complex is exhibiting no influence on other complexes.[8] However in the solid state Iron (II) spin crossover complexes have shown a wide range of temperature dependant transitions which can range from a gradual change over a wide temperature range similar to that of a solution phase, multistep where distinct metal centres transition at different temperatures, abrupt transitions over 0-10 degrees change which can exhibit hysteresis shown in (**Figure 4. 2**). The factors affecting spin crossover behaviours of metal complexes are well known, however cooperativity and the isolation of the long range and short range interaction is an area of continued interest.[21]

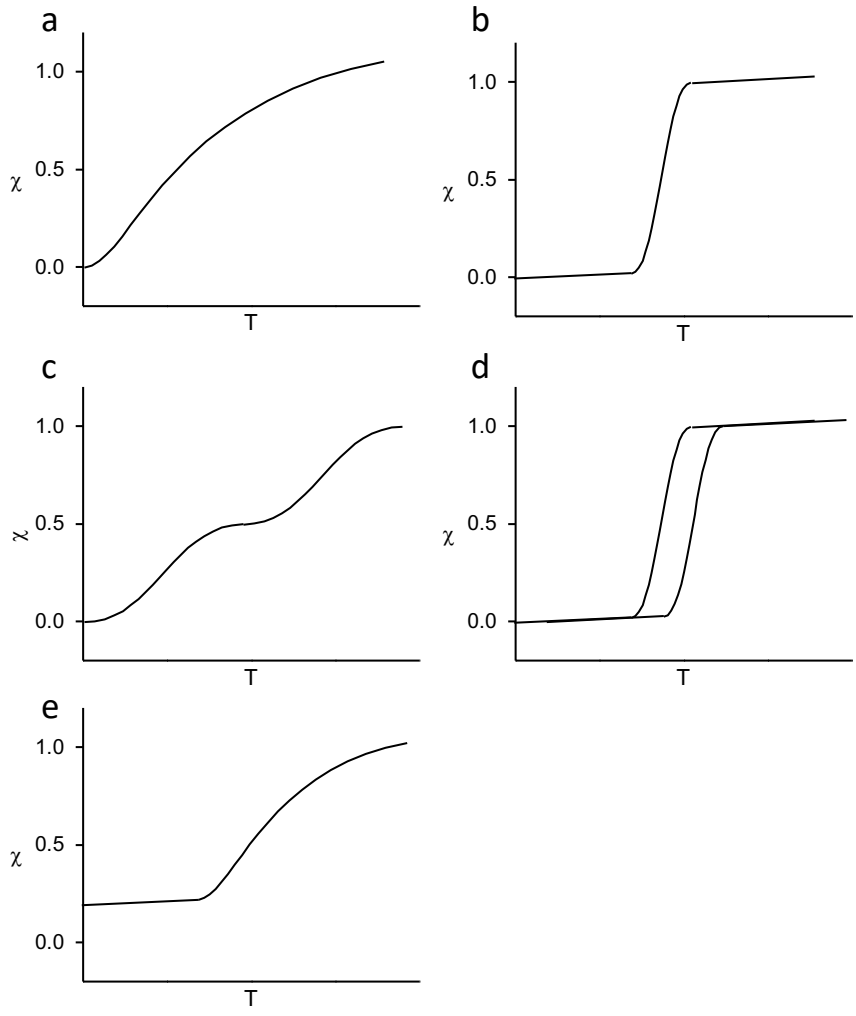

Figure 4. 2 *Schematic representation of different spin crossover behaviours (**a**) gradual (**b**) sharp (**c**) hysteretic (**d**) multi step and (**e**) incomplete, adapted from.*[12]

They include tuning the ligand donor properties, introducing intermolecular interactions into the crystal lattice in order to aid cooperativity and the second coordination sphere interactions. Systems in which a sharp hysteretic spin transition occurs near to room temperature are most interesting due to their technological importance, the magnetic bistability of spin crossover materials lends itself well to the requirements of memory storage devices with easily accessible distinct and discernible states. In the solid-state systems with a sharp transition will exhibit some form of intermolecular interactions, including hydrogen bonding and π-π interactions as these are crystal lattice properties are the basis for

cooperativity. The basis of the cooperative spin crossover transition has been investigated experimentally and computationally, it is based on the volume difference between the LS and HS state inducing local elastic distortions.[22,23]

The investigations of the isomeric 2,6-bis(pyrazol-1-yl)pyridine (1-Bpp) and 2,6-bis(pyrazol--3-yl)pyridine (3-Bpp) constitute a large effort in the literature dominated by the more synthetically versatile 1-Bpp.[24–26] This chapter will focus on the synthesis and characterisation of iron(II) bis(pyrazol-3-yl)pyridine complexes $[Fe(3\text{-}Bpp)_2]^{2+}$.[27,28] The 3-Bpp ligand offers a well-defined and investigated system in which the planar tridentate structure of 3-Bpp creates a highly cooperative transition which is centred around the level of hydration in the material.[28]

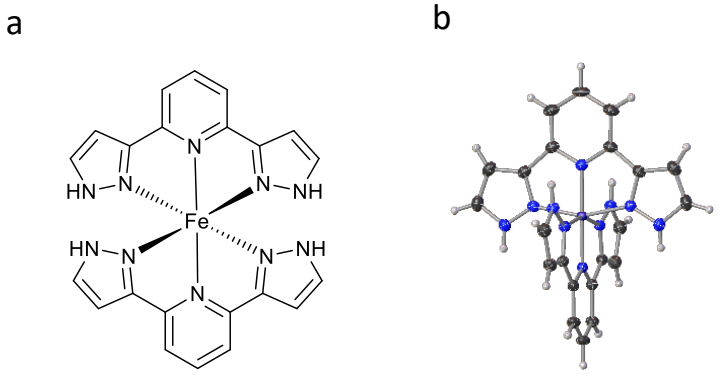

Figure 4. 3 *(**a**) Schematic $[Fe(3\text{-}Bpp)_2]^{2+}$ complex (**b**) Crystal structure of $[Fe(3\text{-}Bpp)_2][NO_3].2H_20$ with solvent and counterion removed for clarity, thermal ellipsoids at 50% where C (grey), H (white), N (blue), Fe (purple).*

The coordinating pyrazolyl nitrogen are weaker σ-donors than that of pyridine, reducing the energy gap between the LS and the HS configuration when compared to terpyridine. The 3-Bpp structure has two unbound secondary amine groups per ligand which are capable of hydrogen bonding interactions with counterions and solvent in the second coordination sphere in contrast to the isomeric 1-Bpp with no free NH groups. Cooperativity which is common with Bpp complexes and their derivatives can be attributed to the terpyridine

embrace packing motif which is commonly seen in octahedral metal-terpyridine complexes.[21,29]

Hydrogen bonding from either the solvated molecules or counterion to the non-coordinating NH on the pyrazolyl increases electron density on the coordinating nitrogen and therefore stabilises the LS state.[30] Thus, strong hydrogen bond accepting moieties such as hydroxy groups and chloride anions stabilise LS state to the greatest degree.[27,30] The spin crossover behaviour of the $[Fe(3\text{-}Bpp)_2]^{2+}$ complex was shown to be intricately linked to the size/charge ratio of the counterion being employed and the resultant packing of these materials in the solid state.[31]

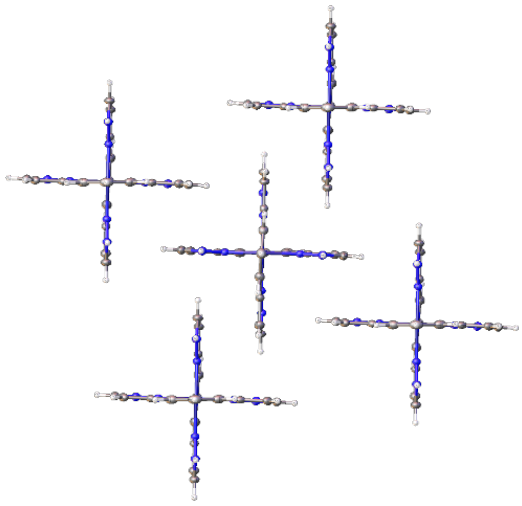

Figure 4. 4 *Terpyridine embrace showing central complex with eight edge to face and four offset face to face interactions.*

By exchanging discrete counterions such as NO_3^-, SO_4^{2-}, or X^- (where X is a halide) with larger counterions, it is possible to disrupt the normal crystal packing motif of the material generating interesting structures with various spin crossover properties. One such method involves the exchange of sulphate counterions with larger organic carboxylate anions through a metathesis reaction between the barium salt of the carboxylate compound and the sulphate anion of $[Fe(3\text{-}Bpp)_2][SO_4]$. Previous work in this area has introduced di and tricarboxylate

anions forming porous hydrogen bonded networks.[32,33] Until now no counterions with such high charge and size have been seen.

4.3 Aims and Objectives

The aim of the chapter is to show the successful synthesis of a series of tetracarboxylate counterions with varying size and flexibility to form porous hydrogen bonded networks with $[Fe(3\text{-}Bpp)_2]^{2+}$ and investigate by single crystal X-ray diffraction (SCXRD), thermogravimetric analysis (TGA) and magnetic measurements the magneto-structural correlation.

4.4 Results and Discussion

4.4.1 Synthesis

The use of a metathesis reaction with $[Fe(3\text{-}Bpp)_2][SO_4]$ and a barium salt is a proven method for the synthesis of porous spin crossover materials.[32] This method has been tried and tested for various carboxylates, it allows the removal of smaller discrete counterions that would compete to hydrogen bond with the iron complexes. It is therefore a useful method for increasing the size to charge ratio of the counterion which has been shown to have an impact on the spin crossover behaviour of the resulting materials.[31] The tetracarboxylate counterions shown in (**Scheme 4. 1**), have been designed to incorporate hydrogen bonding moieties in the form of the two isopthalate units and a flexible alkyl chain linker of varying length. Ethyl (TCA-2C), pentyl (TCA-5C), decyl (TCA-10C) and *p*-xylyl (TCA-*p*) The inclusion of a *p*-xylyl linker provided increased rigidity and the potential for π-π interactions between π systems present in other *p*-xylyl linked anions and the planar tridentate 3-Bpp ligand $[Fe(3\text{-}Bpp)_2]^{2+}$ complexes.

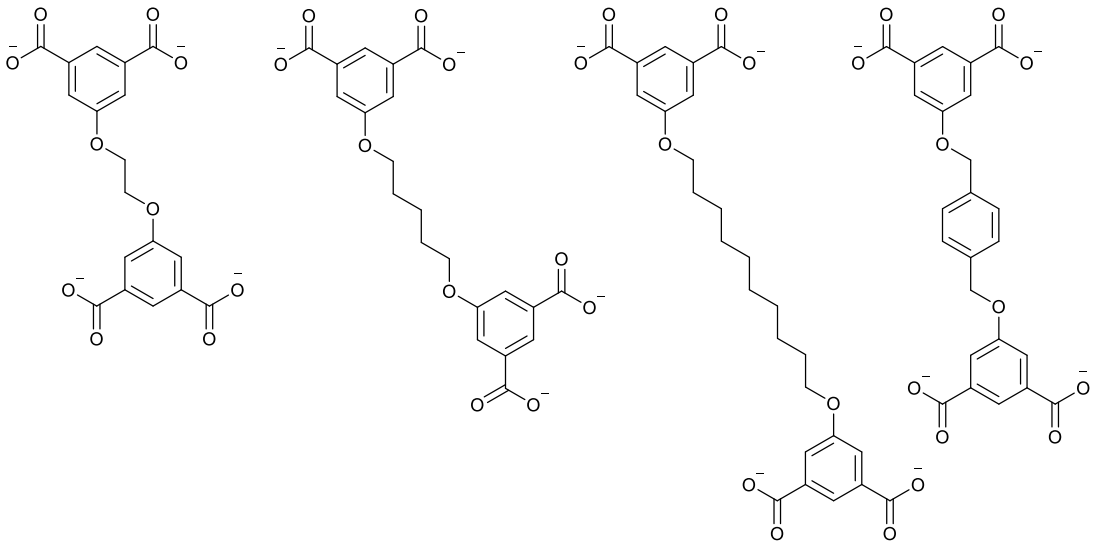

Scheme 4. 1 *Tetracarboxylate counterions with differing length linkers ethyl (TCA-2C), pentyl (TCA-5C), decyl (TCA-10C), and p-xylyl (TCA-p) respectively*

The hydrated materials were successfully synthesised **Scheme 4. 2** and isolated as plate like crystals in the form $[Fe(3\text{-}Bpp)_2]_2(TCA).xH_2O$. These materials were characterised by single crystal X-ray diffraction techniques, thermogravimetric studies and magnetic measurements at varying temperatures by SQUID-magnetometry.

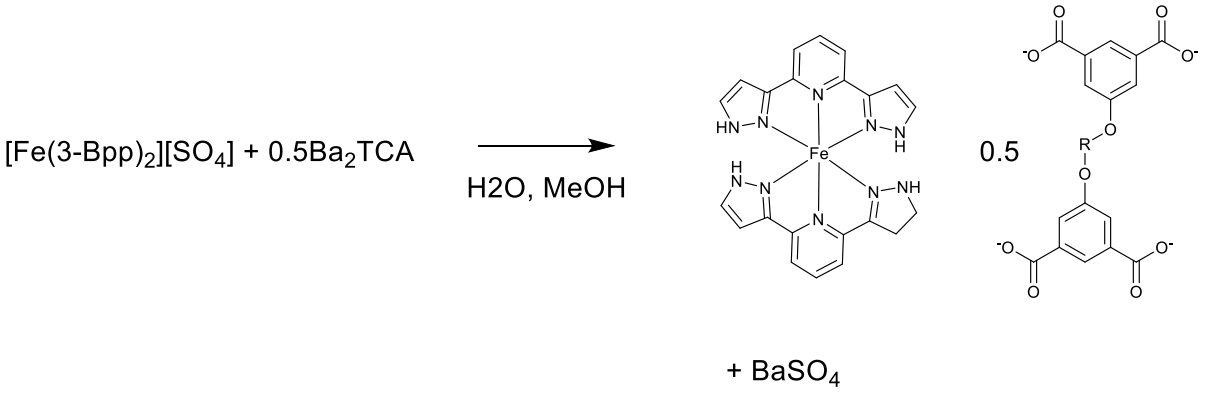

Scheme 4. 2 *Metathesis reaction of [Fe(3-Bpp)2][SO4] with a Ba_2(TCA) salt to form $[Fe(3\text{-}Bpp)2]_2[TCA]\cdot xH_2O + BaSO_4$*

4.4.2 Thermal Analysis

TGA analysis was carried out on each material to determine the thermal behaviour before magnetic measurements. The analysis shows the best temperature range for solvatomagnetism experiments, as the spin state of the $[Fe(3\text{-}Bpp)]^{2+}$ complexes are linked to the solvent, understanding when these will be removed from the structure is key to understanding whether a transition has been induced by this loss. The crystals of $[Fe(3\text{-}Bpp)_2]_2(TCA\text{-}2C)\cdot 20H_2O$ ($Fe(3\text{-}Bpp)_2TCA\text{-}2C$) were of low yield and unstable with respect to solvent loss and crumbled once removed from the supernatant therefore are not analysed by TGA. For $[Fe(3\text{-}Bpp)_2]_2(TCA\text{-}5C)\cdot 15H_2O$ ($Fe(3\text{-}Bpp)_2TCA\text{-}5C$), the TGA (**Figure 4. 5**) shows only one step correlating to approximately 8% weight loss that correspond to the loss of 7 H_2O molecules, this does not correlate to the exact number of molecules in the crystal structure which is thought to be due to an excess of 3-Bpp which is hard to separate from the crystalline

materials. These water molecules are those which are hydrogen bonded in the second coordination sphere. Water molecules which are hydrogen bonded outside of these interactions may be lost in air during the mounting process in the TGA. At 260°C there is a percentage weight loss of 66.5% followed by a drop of 13.7% at 295°C these correspond with the loss of organic ligands and counterions.

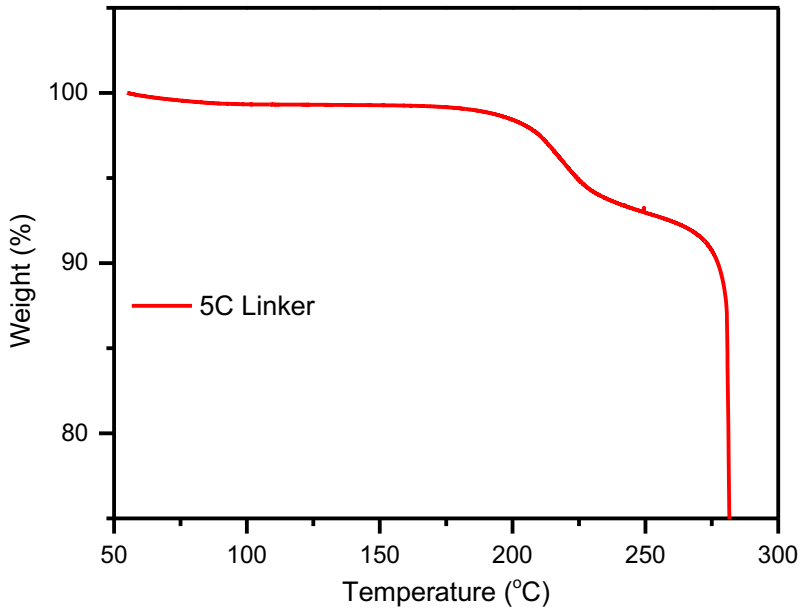

Figure 4. 5 *Thermogravimetric analysis of $Fe(3\text{-}Bpp)_2TCA\text{-}5C$ ramp rate of 5°/min in an argon atmosphere*

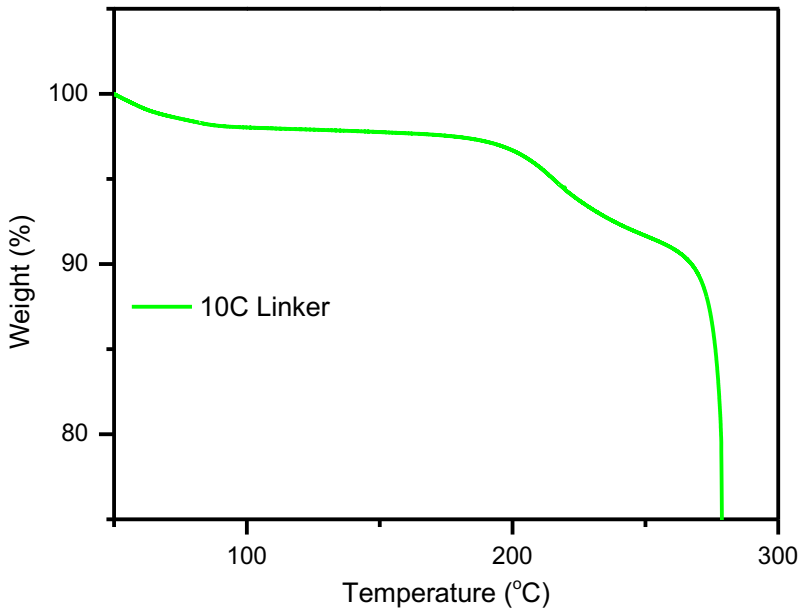

Figure 4. 6 *Thermogravimetric analysis of Material Fe(3-Bpp)$_2$TCA-10C ramp rate of 5°/min in an argon atmosphere*

For [Fe(3-Bpp)$_2$]$_2$(TCA-10C)·9H$_2$O (Fe(3-Bpp)$_2$TCA-10C) with a longer and more flexible 10C linker (**Figure 4. 6**) the TGA showed a gradual decrease below 100 °C, potentially due to water not bound to the crystal structure. Between 180 and 250 °C there is a loss of 9% correlating to 10 H$_2$O molecules. At 260 °C there is a percentage weight loss of 76.5% correlating with the loss of remaining organics.

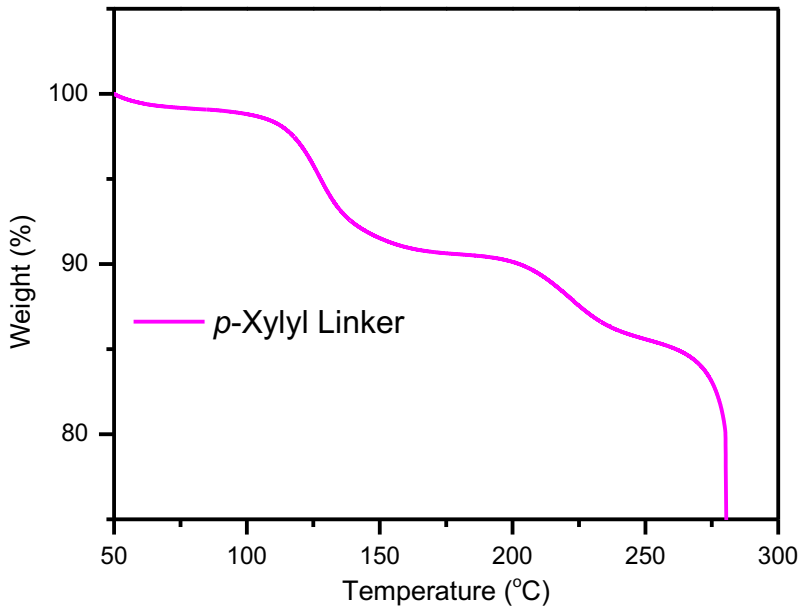

Figure 4. 7 *Thermogravimetric analysis of Material Fe(3-Bpp)$_2$TCA-p ramp rate of 5°/min in an argon atmosphere*

For [Fe(3-Bpp)$_2$]$_2$(TCA-*p*)·2H$_2$O·2MeOH (Fe(3-Bpp)$_2$TCA-*p*) (**Figure 4. 7**), the first weight loss occurring between 100 and 150 °C was a percentage loss of around 10% corresponding to two MeOH molecules followed by a second step at 200-250 °C of 5% corresponding to two H$_2$0 molecules. This is in agreement with the crystal structure obtained for Fe(3-Bpp)$_2$TCA-*p*. At 260° There is a weight loss of 75% correlating to the loss of all organics.

4.4.3 Crystallographic Analysis

4.4.3.1 1st and 2nd Coordination Sphere

Materials Fe(3-Bpp)$_2$TCA-2C,5C,10C and *p* all have the same general first coordination sphere in which the 3-bpp ligands are coordinated to the metal in meridional positions with pseudo C_{2v} symmetry, as expected for Fe(3-Bpp)$_2$]$^{2+}$. The Fe–N bond lengths shown by Fe(3-Bpp)$_2$]$^{2+}$ complexes are indicative of their spin state.[11] Hydrated crystal structures tend to show shorter Fe–N bond lengths below 2 Å, whereas dehydrated complexes featuring no hydrogen

bonding interaction with the non-coordinating nitrogen will exhibit a more distorted first coordination sphere and longer Fe–N bond lengths above 2 Å.[34]

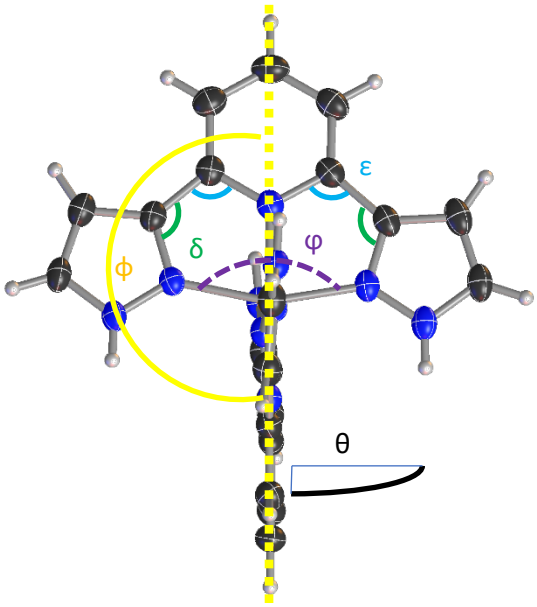

Figure 4. 8 *Schematic showing the relevant angles in octahedral distortion of $Fe(3\text{-}Bpp)_2]^{2+}$ in the solid state.*

The distortion (**Figure 4. 8**) seen can be illustrated in two ways, the ideal θ = 90° and ϕ = 180° angles. The internal δ, ε and φ angles which are associated with the contraction of the octahedral geometry to prismatic via the bailar twist, distortion is exhibited in both LS and HS but is more pronounced in the HS state.[27] Fe(1) exhibits almost ideal angles whereas Fe(2) has a slightly reduced ϕ = 173.6°.

Table 4. 1 *Table of $Fe(3\text{-}Bpp)_2TCA\text{-}2C$ distortion angles ϕ, δ, ε, ϑ and φ*

	Fe-1 Bond Angle/°		Fe-2 Bond Angle/°	
φ	N2-Fe-N	159.1(5)	N-Fe2-N	158.9(6)
		159.6(5)		159.6(6)
δ	N-C-C	114.6(11)	N-C-C	115.1(13)
		108.4(11)		110.1(15)
		109.0(11)		111.0(14)
		114.6(11)		112.8(12)
ε	N-C-C	114.0(11)	N-C-C	115.9(14)
		109.5(11)		111.2(14)
		111.5(12)		110.0(14)
		113.3(12)		112.6(13)
θ	89.25(18)		91.8(2)	
ϕ	177.9(2)		173.6(3)	

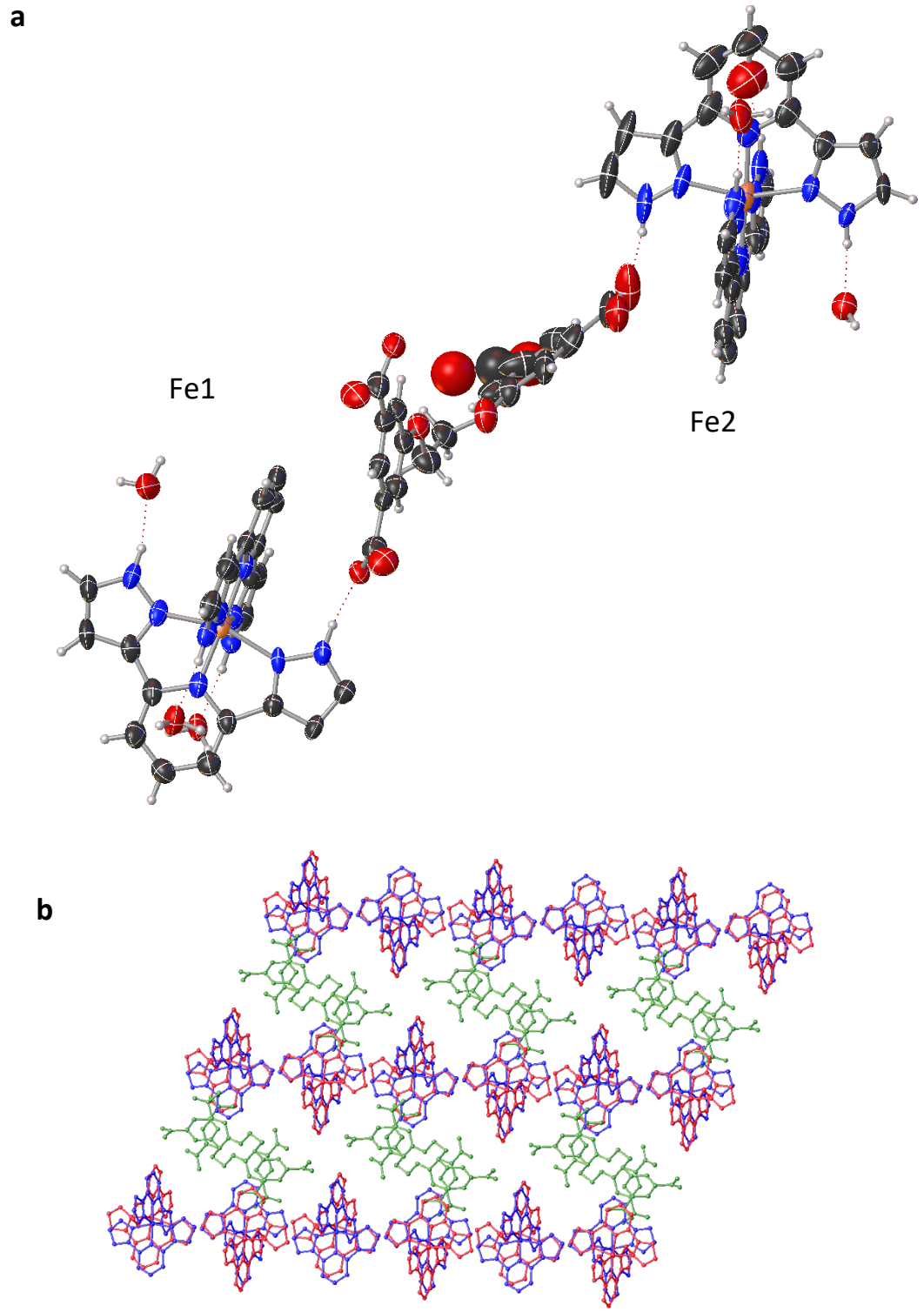

Figure 4. 9 *(**a**) Second coordination sphere for Fe1 Fe(3-Bpp)$_2$TCA-2C, Fe(3-Bpp)$_2$]$^{2+}$ is hydrogen bonded to three water molecules and one TCA-2C molecule. Fe (orange), C (black), O (red), H (white) ellipsoids at 50% thermal probability. Second coordination sphere for Fe2 Fe(3-Bpp)$_2$TCA-2C, Fe(3-Bpp)$_2$]$^{2+}$ is hydrogen bonded to three water molecules and 1 TCA-2C molecule. Fe (purple), C (black), O (red), H (white) ellipsoids at 50% thermal probability. (**b**) Crystallographic 010 plane showing ball and stick representation of extended layered structure with hydrogens omitted for clarity Fe(1) (red), Fe(2) (blue) and TCA-2C (green). Interlayer Fe-Fe distance is 16 Å.*

Fe(3-Bpp)$_2$TCA-2C crystallizes in the triclinic space group $P\overline{1}$, the crystal structure contains two crystallographically unique iron centres Fe(1) and Fe(2) with average Fe-N bond lengths of 1.894(10) – 1.949(10) Å which is characteristic of the LS state. This is consistent with literature as the hydrated $[Fe(3\text{-}Bpp)_2]^{2+}$ is most commonly found in the LS state.[35,36] Both Fe centres in Fe(3-Bpp)$_2$TCA-2C have the same second coordination sphere, each complex is hydrogen bonded through the pyrazolyl NH to three water molecules and one carboxylate group from the counterion. Values for hydrogen bond length and angles are given in **Table 4. 2**. The complexes demonstrated hydrogen bonding interaction to each end of the TCA-2C molecule shown in **Figure 4. 9a**, this orientation is expected to increase interaction between the positive charge and the negative carboxylate groups of the counter ion, along with maximising the hydrogen bonding interactions. Hydrogen bonding between the counterion and the pyrazolyl NH forms the link between 2D layers of terpyridine embraced cations which gives rise to the porous structure. The 2D layers contain alternating iron centres of Fe1 and Fe2 with an interlayer separation of approximately 16 Å. The pores were analysed using Olex 2.1.3 using the olex solvent mask and shows solvent accessible void as 616 Å^3, 190 e^- correlating to approximately 10 H_2O per asymmetric unit cell.

Table 4. 2 *Selected hydrogen bond lengths and bond angles for Fe(3-Bpp)$_2$TCA-2C*

H – Bond	dÅ	Bond Angle/^{o}
N1–O1s	2.755(16)	172.3
N5–O2s	2.746(13)	175.0
N6–O5s	2.735(15)	160.0
N10–O9	2.647(13)	162(15)
N11–O10s	2.755(16)	170.1
N15–O2	2.746(13)	164.6
N16–O4s	2.735(15)	168.6
N20–O3s	2.647(13)	163.4

Fe(3-Bpp)$_2$TCA-5C crystallizes in the triclinic space group $P\bar{1}$ and features two Fe centres with average Fe-N bond lengths ranging from Fe1 1.924(3) – 1.986(3) Å and Fe2 1.917(3) – 1.973(3) Å. The longer bond lengths in Fe1 indicate that it has more HS character, this increase in bond length can be seen in the distortion of the first coordination sphere illustrated in **Figure 4. 10a**. Pores were analysed showing solvent accessible void as 495 Å^3, 127 e$^-$ correlating to approximately 7.5 H_2O per asymmetric unit cell, showing that the structure is penetrable along the a axis for spheres with a radii of 1.60 Å^3.

Table 4. 3 *Table of Fe(3-Bpp)$_2$TCA-5C distortion angles ϕ, δ, ε, ϑ and φ*

	Fe-1 Bond Angle/°		Fe-2 Bond Angle/°	
φ	N-Fe-N	157.94(9)	N-Fe2-N	159.43(9)
		158.59(9)		158.85(9)
δ	N-C-C	113.8(2)	N14-C31-C30	114.2(2)
		111.3(2)	C31-C30-N13	110.1(2)
		111.0(2)	N13-C26-C25	109.9(2)
		114.4(2)	N12-C25-C26	114.1(2)
ε	N-C-C	113.95(19)	N17-C36-C37	113.9(2)
		110.3(2)	N18-C41-C42	110.5(2)
		110.5(2)	N18-C37-C36	110.4(2)
		114.03(19)	C41-C42-N19	113.9(2)
θ	90.99(6)		90.74(6)	
ϕ	172.32(9)		173.57(9)	

The difference in Fe-N bond lengths between the two iron centres can be rationalised by the second coordination sphere, where Fe(1) (**Figure 4. 10a**) is bound to three TCA-5C anions and one water molecule whereas the Fe(2) centre is bound to two TCA-5C and two water molecules (**Figure 4. 10b**). The increase in steric bulk surrounding the complex in Fe(1) causes a disruption to the packing of the molecules in order to incorporate the counterion. No real difference is seen in the distortion angles comparing Fe(1) and Fe(2) **Table 4. 3**.

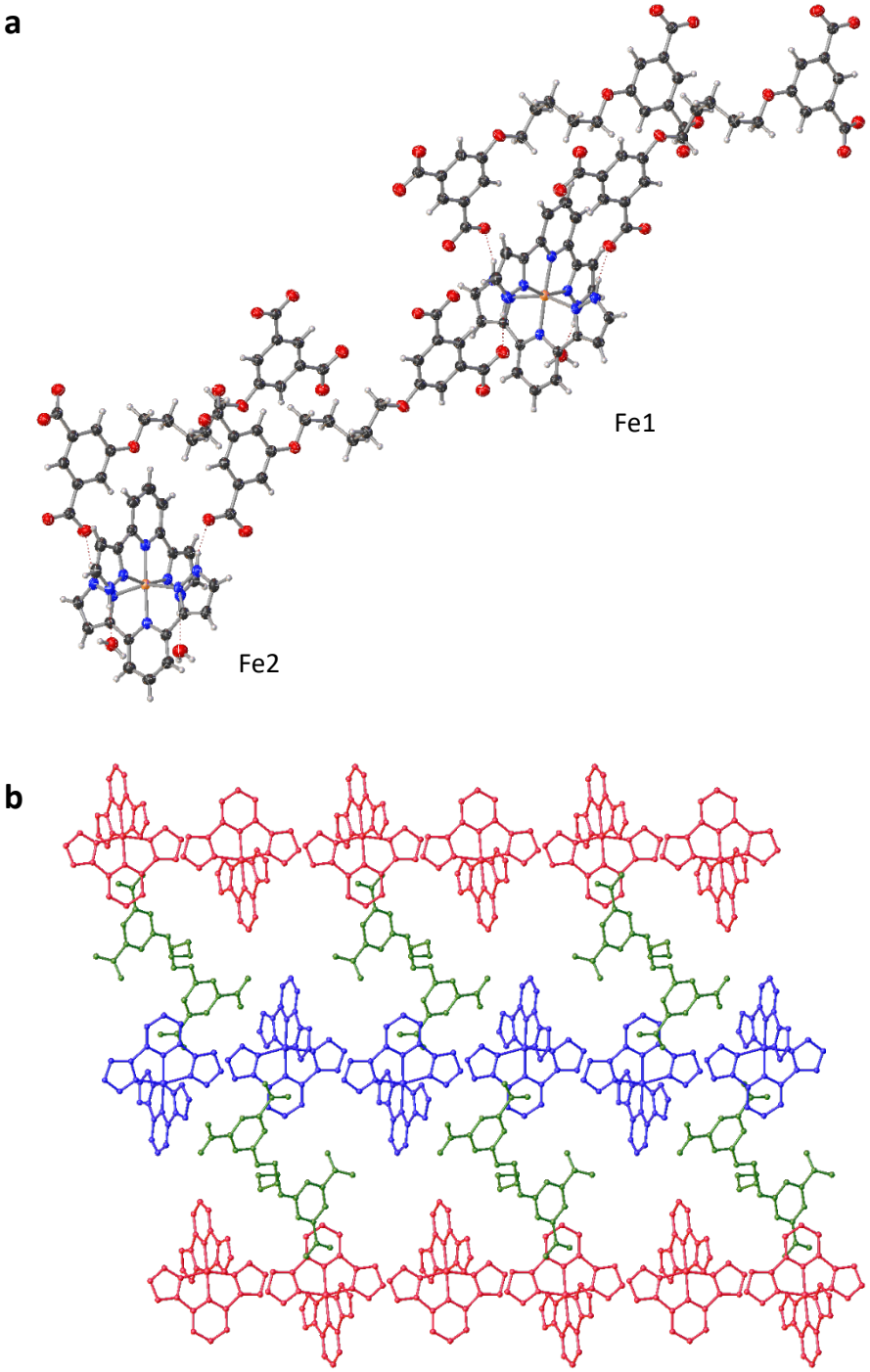

***Figure 4. 10 a**) Second coordination sphere for Fe(3-Bpp)$_2$TCA-5C Fe1 3 TCA and 1 H_2O and Fe2- 2 TCA and 2 H_2O showing hydrogen bonds between carboxylate anions and pyrazol groups of $[Fe(3\text{-}Bpp)_2]^{2+}$ (**b**) Packing diagram with hydrogens and solvent molecules removed for clarity showing the alternating layer structure and porous structure.*

Table 4. 4 *Selected hydrogen bond lengths and bond angles for Fe(3-Bpp)$_2$TCA-5C*

H – Bond	dÅ	Bond Angle/^{o}
N1–O7	2.636(4)	172.2
N5–O8s	2.667(3)	158.5
N6–O6	2.681(4)	169.2
N10–O12s	2.681(4)	155.2
N11–O1s	2.779(4)	170.5
N15–O10s	2.714(4)	176.9
N16–O4	2.621(4)	176.8
N20–O3	2.656(4)	163.8

Fe(3-Bpp)$_2$TCA-10C crystalizes in the monoclinic P2/c space group, it exhibits one Fe centre with Fe-N bond lengths below 2Å indicating a LS state. The complex is hydrogen bonded to one counterion and three solvent molecules (**Figure 4. 11a**). Due to poor diffraction data attributed to the increased flexibility of the linker and the weak data, alkyl chains bond lengths and angles have been idealised. This still allows for identification and packing investigations, but angles and bond lengths are not available. The packing diagram **Figure 4. 11b** shows a change in the packing structure compared to Fe(3-Bpp)$_2$TCA-2C and Fe(3-Bpp)$_2$TCA-5C due to the increased importance of Van der Waals interactions with an increased alkyl chain this favours the close contact of the chains forming layers.

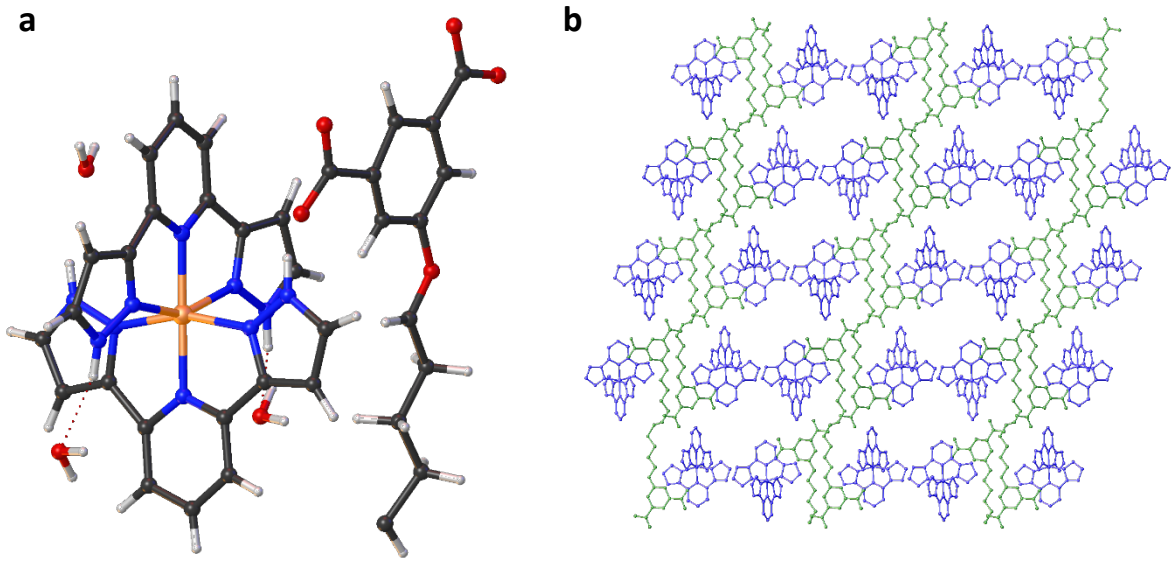

***Figure 4. 11 a**) Second coordination sphere of $[Fe(3\text{-}Bpp)_2]^{2+}$ in $Fe(3\text{-}Bpp)_2TCA\text{-}10C$ modelled ball and stick **b**) Layered structure for $Fe(3\text{-}Bpp)_2TCA\text{-}10C$ showing layers of counterion (green) disrupting the terpyridine embrace (blue).*

$Fe(3\text{-}Bpp)_2TCA$-*p* crystallizes in the monoclinic space group P $2_1/c$ with one Fe centre in the LS state, confirmed by the Fe-N bond lengths ranging from 1.943(15) - 1.999(16) Å. The iron complex is hydrogen bonded to three TCA and one methanol molecule with water molecules hydrogen bonded in pockets and one methanol molecule interacting with the *p*-xylyl π-system through the methyl CH σ-π interaction 2.791 Å.[37] The first coordination sphere, due to the higher number of counterions bonded in the second coordination sphere, is distorted away from the C_{2v} symmetry (**Table 4. 5**, **Figure 4. 12c**).

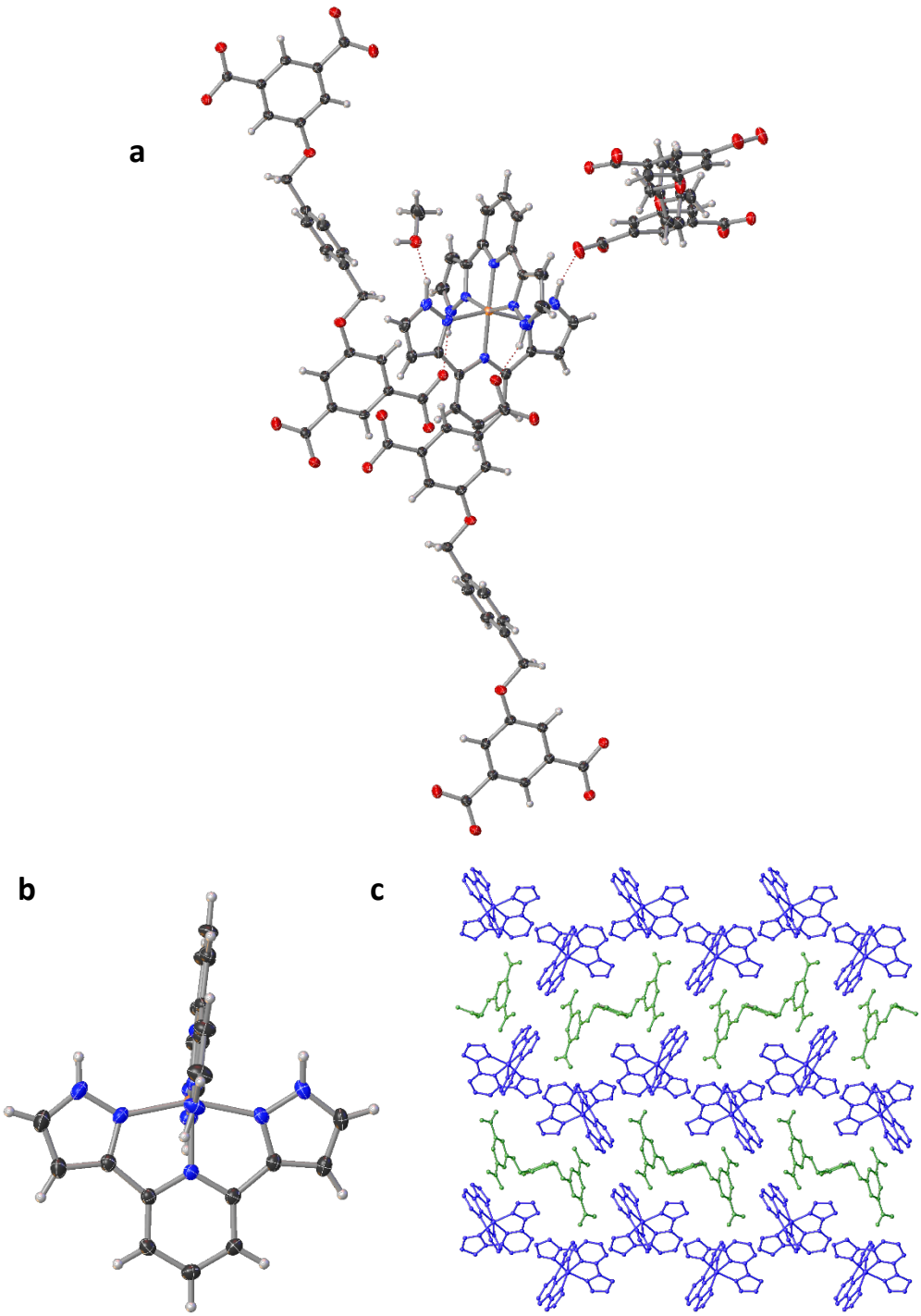

Figure 4. 12 *a) Composition of the second coordination sphere for Fe(3-Bpp)$_2$TCA-p* showing hydrogen bonds to 3 counterions and 1 water molecule. b) Crystal packing diagram of *Fe(3-Bpp)$_2$TCA-p* showing the chain like structure.

Table 4. 5 *Table of Fe(3-Bpp)$_2$TCA-p distortion angles ϕ, δ, ε, ϑ and φ*

	Fe-1 Bond Angle/°	
φ	N-Fe-N	157.27(6)
		157.23(6)
δ	N-C-C	114.28(16)
		111.06(15)
		110.93(14)
		114.58(15)
ε	N-C-C	113.92(14)
		110.40(15)
		110.57(15)
		114.59(15)
θ	86.42(3)	
ϕ	172.80(4)	

Although the first coordination spheres for all these materials are similar and exhibit low spin iron centres at the temperature used for crystallographic data collection (120 K) the second coordination spheres show different compositions creating a variety of structures in the solid state. The analysis of Fe-N bond length has shown that hydrogen bonding with the high charge tetracarboxylate anions along with solvent interactions is stabilising the low spin state in these systems which is in line with the literature.

Table 4. 6 *Comparative Fe–N bond lengths , Fe-Fe interlayer distances and Fe-Fe intralayer distances for Fe(3-Bpp)$_2$TCA-2C,5C,10C and p*

Material	Second Coordination Sphere	Fe-N Å	Fe-Fe interlayer Å	Fe-Fe Intralayer Å	
1	3 H_2O, 1TCA	Fe(1) 1.893(11) – 1.968(10)	Plane-plane shortest distance 13.758(4)	Fe(1)	Fe(2)
		Fe(2) 1.899(14) – 1.989(11)		8.337(4)	8.157(3)
				8.157(3)	8.266(4)
				8.459(3)	8.063(3)
				8.063(3)	8.459(3)
2	3 H_2O, 1TCA	Fe(1) 1.924(3) – 1.986(3)	Fe(1)-Fe(2)	Fe(1)	Fe(2)
	2 H_2O, 2TCA	Fe(2) 1.918(3) – 1.973(2)	13.000(8)	8.5028(10)	8.1047(10)
				8.0638(1)	8.0638(1)
				8.1896(10)	8.0638(1)
				8.0638(1)	8.2113(10
3	3 H_2O, 1TCA	N/a	12.407(3)	8.45(1)	
			12.893(10)	7.8571(14)	
4	3 TCA, 1 MeOH	1.9435(14) – 1.9989(15)	9.5707(1)	8.1550(3)	

4.4.3.2 Packing Effects

The common packing motif for $[Fe(3\text{-}Bpp)_2]^{2+}$ is the terpyridine embrace, which is stabilised by 8 edge-face and 4 offset face-face interaction per iron complex. With discrete counterions alternating up and down facing 3-Bpp ligands form channels which the next layer sits in forming an A-B-A' pattern shown in (**Figure 4. 13**) taken from the crystal structure of $[Fe(3\text{-}Bpp)_2][NO_3]$. The terpyridine embrace and hydrogen bonds which stabilise the packing motif are also the basis for the propagation of the spin transition throughout the material.

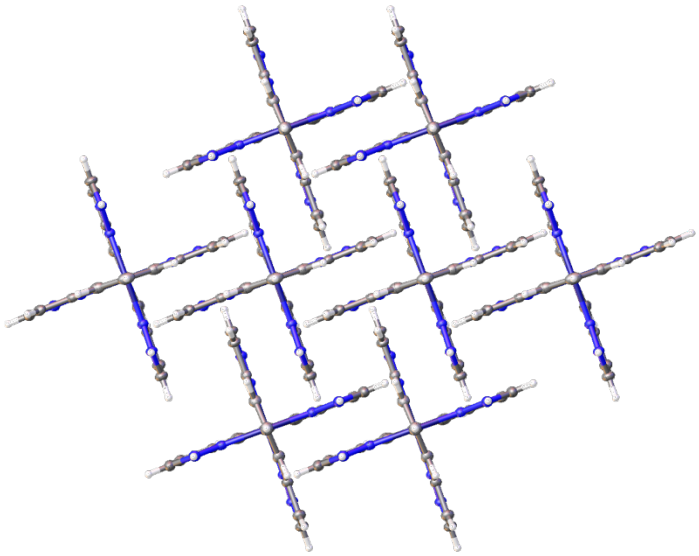

Figure 4. 13 *[Fe(3-Bpp)$_2$][NO$_3$] with counterions removed to show the terpyridine embrace packing motif*

The interlayer interactions are disrupted by the introduction of the bulky TCA anions which causes the separation of layers allowing the formation of pores which are occupied by a hydrogen bonded network of solvent, in the case of Fe(3-Bpp)$_2$TCA-2C,5C and 10C these are water molecules. Fe(3-Bpp)$_2$TCA-2C and 10C both exhibit 2D layers of interdigitated iron complexes separated by hydrogen bonded counterions (**Figure 4. 14a**). The interlayer distances are 13.8 and 13 Å, respectively compared to 10 Å for the nitrate complex. The crystallographically unique centres in Fe(3-Bpp)$_2$TCA-2C occupy the same layer, whereas in Fe(3-Bpp)$_2$TCA-5C the iron centres occupy alternating layers shown in (**Figure 4. 14b**). Despite the larger size of the TCA-5C anion, conformationally I am suggesting that the increased flexibility allows the interlayer distance to be reduced, the increased length of TCA-5C is offset by the angle at which it links the layers. Increasing the length of the alkyl chain from pentyl to decyl further disrupts the terpyridine embrace motif, the porous structure which is generated has layers of counterions separated by “pillars” of iron complex show in (**Figure 4. 14c**).

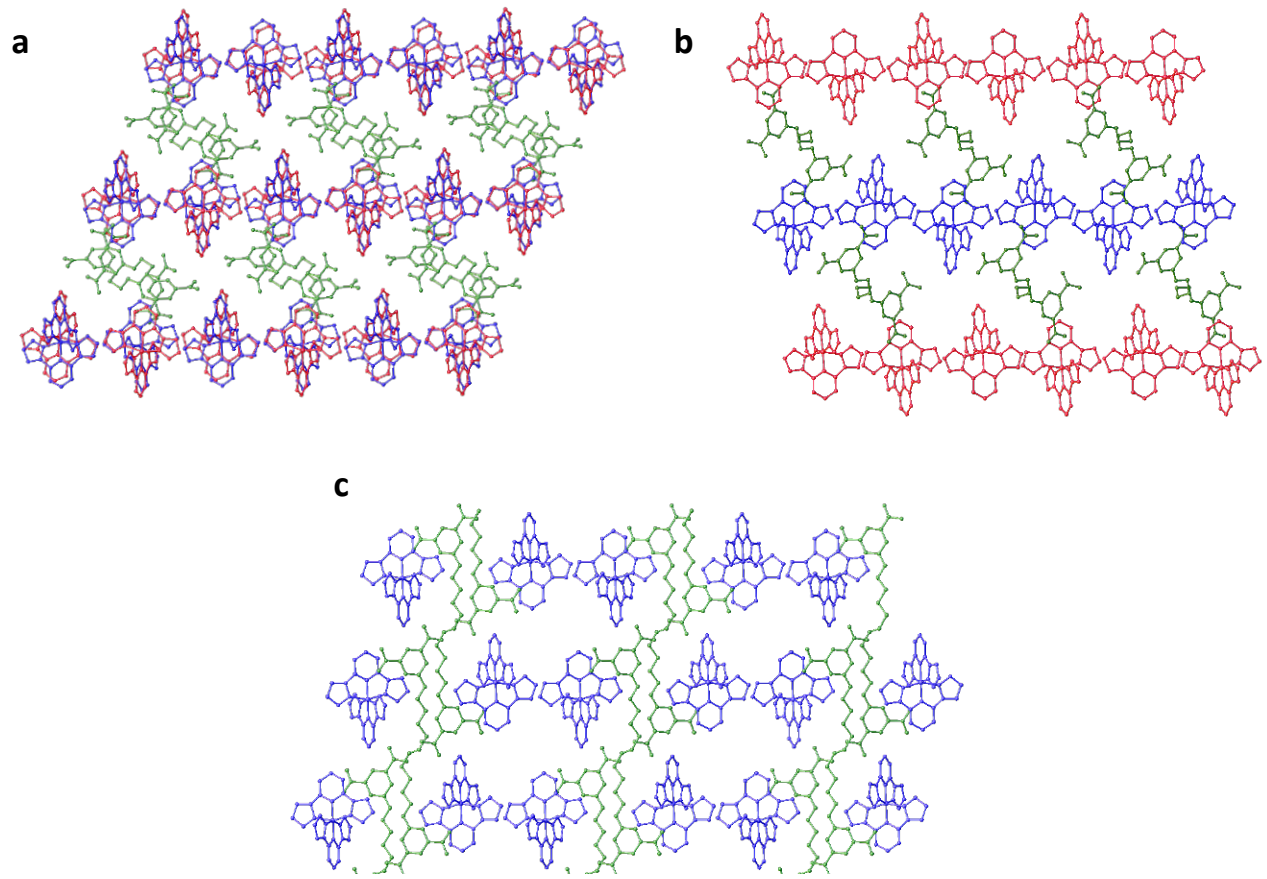

Figure 4. 14 *Side by side comparison of* ***a****) Packing diagram for Fe(3-Bpp)$_2$TCA-2C (****b****) packing diagram for Fe(3-Bpp)$_2$TCA-5C and (****c****) packing diagram for Fe(3-Bpp)$_2$TCA-10C*

By introducing a *p*-xylyl unit as the linker, the flexibility of the anion is decreased whilst steric bulk is increased with the additional opportunity for aryl-aryl interactions in the solid state. The terpyridine embrace motif in Fe(3-Bpp)$_2$TCA-*p* is completely disrupted and shows a zigzag like structure with discrete pockets containing the TCA-*p* anion (**Figure 4. 15a,b**).

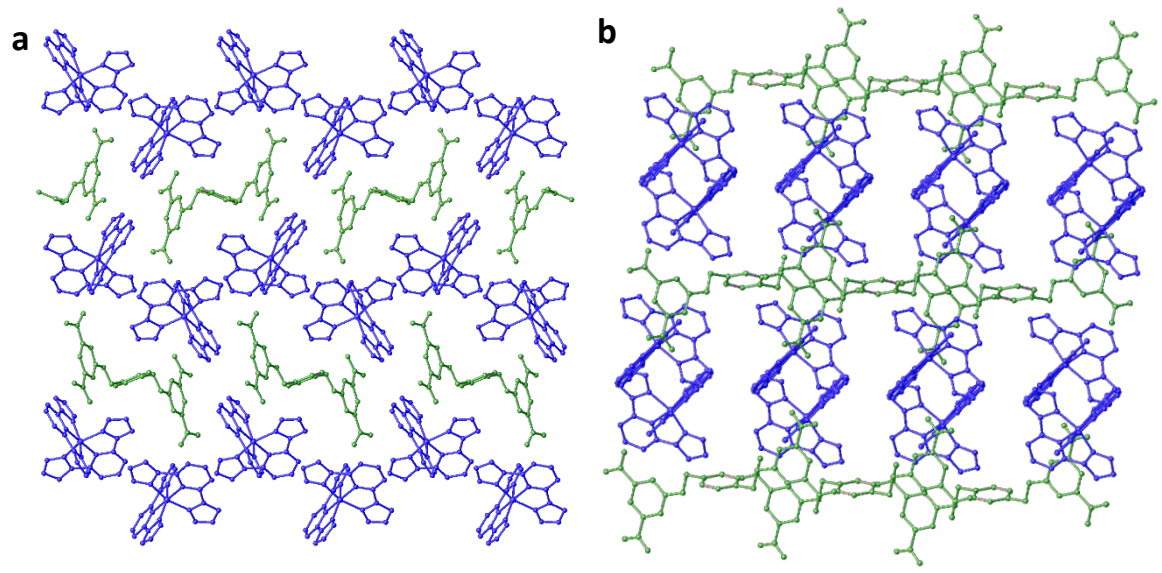

***Figure 4. 15 a**) Fe(3-Bpp)$_2$TCA-p packing diagram showing the 011 plane. With zigzag like [Fe(3-Bpp)$_2$]$^{2+}$ (**b**) Packing diagram showing 010 plane pairwise interaction*

4.4 Magnetic Properties

Magnetic measurements have not been performed on material 1 due to the low yield of the synthesis. Fe(3-Bpp)$_2$TCA-5C and Fe(3-Bpp)$_2$TCA-10C exhibit typical temperature dependent spin crossover properties for hydrated Fe(3-Bpp)$_2$]$^{2+}$ on increasing temperature from 5-400K.

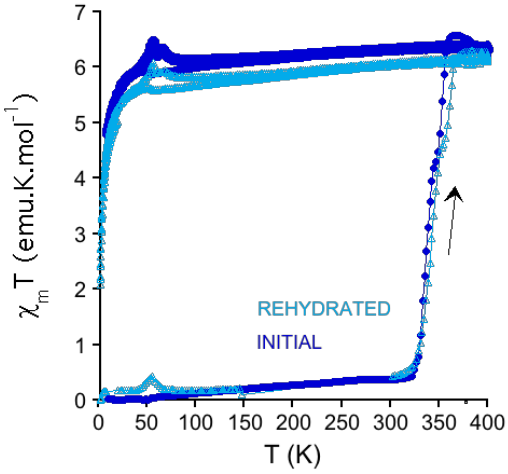

***Figure 4. 16** Magnetic susceptabillity measurements for Fe(3-Bpp)$_2$TCA-5C from synthesis (blue) and rehydrated (cyan)*

The magnetic measurements for Fe(3-Bpp)$_2$TCA-5C (**Figure 4. 16**) show that there is a multistep transition at 330K due to the loss of solvent from the two independent iron centres

which induces a sharp transition from LS to HS. The loss of solvent can be seen by TGA and also visually during temperature dependant imaging (**Figure 4. 17a and b)**.

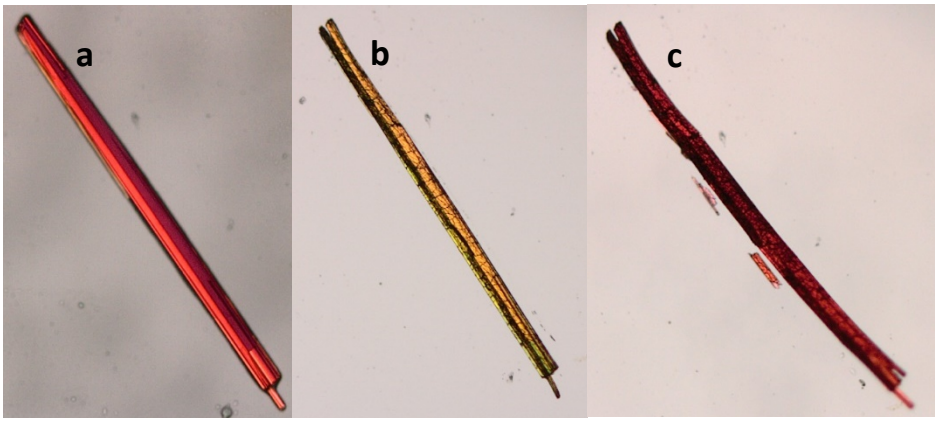

***Figure 4. 17 a**) Image showing solvated Fe(3-Bpp)$_2$TCA-5C crystals (**b**) Image after desolvation by heating showing colour change and cracking of the crystal (**c**) Image after rehydration with by water condensation showing colour change (crystal remains cracked).*

On return cycling back to low temperature it is not possible to regain the diamagnetic LS state, so the dehydrated materials are trapped in the HS state. On rehydration the magnetic properties of the material are recovered, and the same behaviour can be recovered shown by the cyan curve in (**Figure 4. 18**) and visually in (**Figure 43c)**.

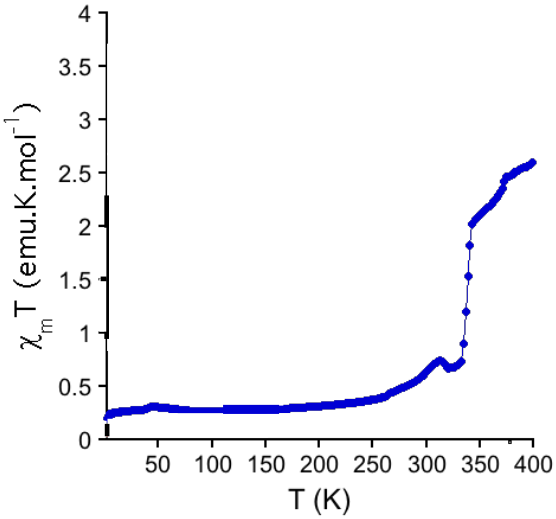

***Figure 4. 18** Magnetic susceptibility measurements from 0 to 400K for Fe(3-Bpp)$_2$TCA-10C*

Fe(3-Bpp)$_2$TCA-10C exhibits a sharp transition from LS to HS at 330K (**Figure 4. 19**) showing similar behaviour to Fe(3-Bpp)$_2$TCA-5C, however only one temperature ramp was possible on this sample.

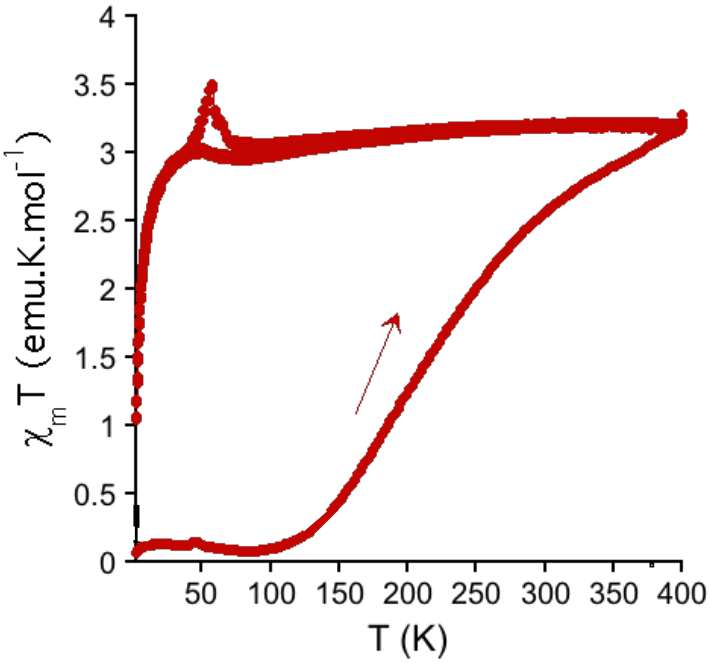

Figure 4. 19 *Magnetic susceptibility measurements from 0 to 400 K for Fe(3-Bpp)$_2$TCA-p*

Fe(3-Bpp)$_2$TCA-*p* exhibits a gradual spin transition from LS to HS with respect to increasing temperature. There is no sharp transition due to the loss of solvent despite it being coordinated with the iron centre (**Figure 4. 19**). The TGA shows multistep loss of solvent at elevated temperatures above that of the magnetic measurement, the material does not return LS therefore the transition can be considered as irreversible.

4.5 Magneto-Structural correlation

Recent literature has shown that in materials with a hydrated [Fe(3-Bpp)2]$^{2+}$ centres exhibiting a terpyridine embraced packing motif and high charge-size ratio counterions stabilise the sharp LS-HS transition seen by Fe(3-Bpp)$_2$TCA-5C and 10C.[31] Due to the loss of

crystallinity in these materials caused by the removal of solvent from the crystal structures it has not been possible obtain a crystal structure analysis of the rehydrated materials. Rehydration of Fe(3-Bpp)$_2$TCA-5C allowed full recovery of the magnetic behaviour however it is not possible to determine whether the porous structure is recovered fully or if there is just coordination to the empty second coordination sphere site, however the uptake of water does imply that the open porous structure has been retained to some degree. The gradual spin transition behaviour of the TCA-*p* material can be rationalised by the distortion of its terpyridine embrace structure, reducing the cooperativity within the system. This packing motif also exhibits a hydrogen bonded structure in which the solvent is tightly bound reducing the likelihood of bulk solvent loss which is explained by the multiple step solvent loss in the TGA at high temperatures.

4.6 Characterisation Techniques

4.6.1 Crystal Structure Determination

Single crystals of each material were mounted in Fomblin™ on a Micromount. Suitable crystals were run on a diffractometer. (YR-1800 perfluoropolyether oil) on a MiTeGen MicroMount^{TM}, crystals of Fe(3-Bpp)$_2$TCA-2C and Fe(3-Bpp)$_2$TCA-*p* were frozen in a stream of cold nitrogen using an Oxford Cryosystems open flow cryostat and kept at 120(2) K during data collection. Single crystal x-ray diffraction data were collected on an Agilent SuperNova diffractiometer (mirror-monochromated Cu-Kα radiation source; λ=1.5418; ω scans), equipment with either an Atlas, Atlas S2 or Titan S2 detector. Cell parameters were refined from the observed positions of all strong reflections in each data set and absorption corrections were applied using an Gaussian numerical method with beam profile correction (CrysAlisPro).[38] Using Olex2, the structure was solved with the ShelXS[39] structure solution

program using Direct Methods and refined with the ShelXL[40] refinement package using Least Squares minimisation. Structures were CIF-checked in conjunction with Dr Stephen Argent and Dr William Lewis.

Crystals of Fe(3-Bpp)$_2$TCA-5C and Fe(3-Bpp)$_2$TCA-10C were collected at the diamond light source synchrotron (λ=0.6889).

4.6.2 Magnetic Measurements

Magnetic susceptibility measurements were performed on polycrystalline samples using a magnetometer equipped with a SQUID sensor. Variable temperature measurements were carried out in the temperature range 2–400 K in a magnetic field of 0.1 T. The temperature sweeping rate was the same for the experiments performed on the original and rehydrated samples: 0.5 K min^{-1} (2–20 K), 2 K min^{-1} (20–200 K), 1 K min^{-1} (200–400 K). Dehydrated samples for magnetic measurements were obtained in-situ by maintaining the sample in the SQUID at 400 K for 100 min (until a constant magnetic signal was obtained). All measurements were performed on plastic capsules perforated to favour solvent loss. Rehydrated samples were cooled to 100 K before applying a vacuum in the SQUID pre-chamber.

4.7 Experimental Section

Ligands, complexes and TCA counterions were synthesised by previously published procedures.[41,42]

4.7.1 3-Bpp Synthesis

Synthesis of the 2,6-bis(pyrazol-3-yl) pyridine ligand that is used in complexation with $FeSO_4.7H_2O$. A suspension of 2,6-diacetylpyridine (2.5g, 15.3 mmol) in *N,N*-

dimethylformamide dimethyl acetal (DMF-DMA) (5ml, excess) was heated at reflux (105°C) for 10h. After cooling the excess DMF-DMA excess was removed under vacuum affording a crude orange powder of 1,1-((2,6-pyridyl)bis-3-dimethylamino)-2-propen-1-one (1.61 g, 4.86 mmol, 31.8%).

δ_H (400 MHz, Chloroform-*d*) 2.99 (6 H, s, **7**/**8**), 3.18 (6 H, s, **7**/**8**), 6.61 (2 H, d, *J* 12.9, **5**), 7.89 (1 H, t, *J* 7.7, **1**), 7.92 (2 H, d, *J* 12.8, **6**), 8.21 (2 H, d, *J* 7.8 **2**). δ_C (101 MHz, $CDCl_3$) 37.23 (2 CH_3, **7**/**8**), 45.24 (2 CH_3, **7**/**8**), 91.59 (2 CH, **5**), 123.78 (2 CH_{Ar}, **2**), 137.52 (CH_{Ar}, **1**), 154.56 (2 CH, **6**), 154.72 (2 C_q, **3**), 186.92 (2 C_q, **4**). ESI-MS m/z = 274.1552 ($C_{15}H_{20}N_3O_2^+$, M+H)

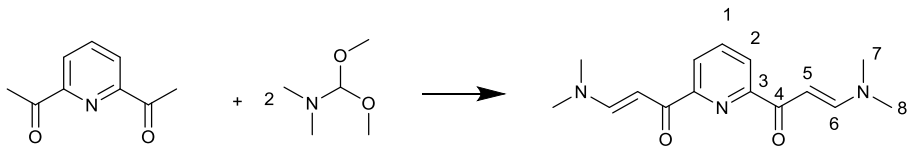

Scheme 4. 3 *Claisen-Schmidt condensation of 2,6-diacetly pyridine in DMF-DMA*

A suspension of crude 1,1-(2,6-pyridyl)bis-3-dimethylamino)-2-propen-1-one (1.61 g, 5.9 mmol) in absolute ethanol (10 mL) and hydrazine monohydrate (2 mL) were stirred at room temperature for 3h. After the initial formation of a precipitate, the reaction product was fully precipitated out using water (5 mL). The product was collected by filtration, washed with water and isolated as a white powder was collected (0.83 g, 66%).

δ_H (400 MHz, DMSO-d_6) 6.98 (2 H, s), 7.54 – 8.17 (5 H, m), 13.29 (2 H, d, *J* 185.4). ESI-MS m/z = 212 ($C_{11}H_9N_5H^+$, M+H)

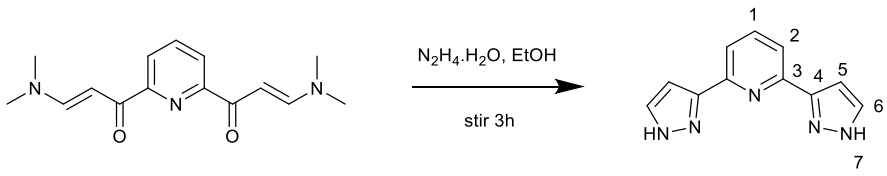

Scheme 4. 4 *Cyclisation of 3-Bpp by reaction with hydrazine monohydrate*

4.7.2 General Synthesis of the Tetra Ester

Under a nitrogen atmosphere dimethyl 5-hydroxyisopthalate (4.86 g, 23.1 mmol), α,ω-dibromoalkane (10.0 mmol) and K_2CO_3 (5.0 g) were stirred in dry DMF 25 mL for 48 h. The reaction mixture was poured into H_2O 400 mL and stirred vigorously for 15 minutes. The resulting white precipitate was collected by vacuum filtration and washed with H_2O (3 x 100 mL). The precipitate was then dissolved in $CH_2Cl_2/CHCl_3$ (400 mL) and washed with 5% NaOH (3 x 100 mL). The solution was dried over $MgSO_4$ and filtered. The solvent was removed *in vacuo* and the product was isolated as a white powder. Yields varied depending on the alkyl chain.

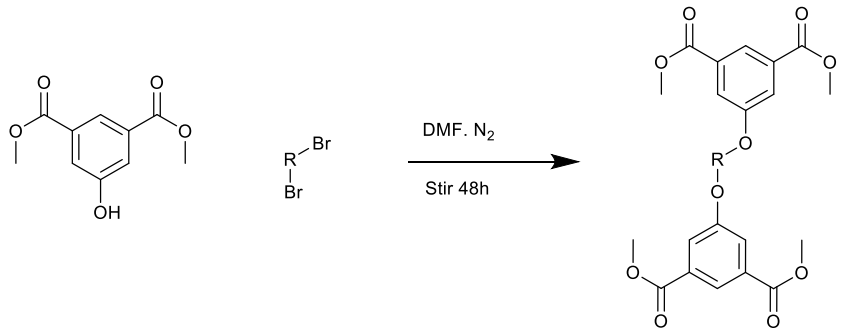

Scheme 4. 5 *General synthesis of tetraester compounds where R = Ethyl, Pentyl, Decyl and p-Xylyl linker*

Ethyl – ^{1}H NMR 400 MHz ($CDCl_3$) δ ppm = 8.34 (t, 2H, -CH_{Ar}); 7.84 (d, 4H, -CH_{Ar}); 4.47 (s, 4H, O-CH_2); 3.97 (s, 12H, O-CH_3). ^{13}C NMR 400 MHz ($CDCl_3$) δ ppm = 1661.1 (C=O); 158.7 (CH_{Ar}); 132.0 ($CH_{Ar}{}^2$Ph); 123.6 ($CH_{Ar}{}^6$Ph); 123.6 ($CH_{Ar}{}^1$Ph); 120.1 ($CH_{Ar}{}^5$Ph); 67.1 (O-CH_2); 52.6 (CO_2-Me). ATR IR ν_{max}/cm^{-1} 3693.52; 3605.52; 1723.70; 1599.76. ESI-MS: 447.13 ($C_{22}H_{25}O_{10}^+$, $M+H^+$), 469.11($C_{22}H_{24}O_{10}Na^+$, $M+Na^+$). Yield = 25%

Pentyl - ^{1}H NMR 400 MHz ($CDCl_3$) δ ppm = 8.25 (t, 2H, -CH_{Ar});); 7.74 (d, 4H, -CH_{Ar}); 4.09 (t, 4H, -O-CH_2); 3.94 (s, 12H, -O-CH_3); 1.92 (q, 4H, -CH_2); 1.72 (m, 4H, -CH_2); ^{13}C NMR 400 MHz ($CDCl_3$) δ ppm = 166.6 (C=O); 159.5 (C-O_{Ar}); 132.1 ($C_{Ar}{}^6$Ph); 123.2 ($CH_{Ar}{}^1$Ph); 120.2 ($CH_{Ar}{}^5$Ph); 68.30

(CH_2-O); 52.39 (O-CH_3), 28.82 (CH_2), 22.68 (CH_2), .IR ν_{max}/cm^{-1} 3691, 3605, 1722, 1601, 1435. ESI-MS =581.23 ($C_{30}H_{38}O_{10}Na^+$, M+Na^+). Yield = 92%

Decyl -^{1}H NMR 400 MHz ($CDCl_3$) δ ppm = 8.25 (t, 2H, -CH_{Ar}); 7.73 (d, 4H, -CH_{Ar}); 4.03 (t, 4H, -O-CH_2); 3.93 (s, 12H, -O-CH_3); 1.80 (q, 4H, -CH_2); 1.48 (q, 4H, -$CH_{2)}$; 1.35 (m,8H, -CH_2). ^{13}C NMR 400 MHz ($CDCl_3$) δ ppm = 166.3 (C=O); 159.4 (C_{Ar} ^{2}Ph); 131.8 (C_{Ar} ^{6}Ph); 122.7 (CH_{Ar} ^{1}Ph); 119.9 (CH_{Ar} ^{5}Ph); 68.7 (H_2C-O); 52.5 (CO_2-Me); 29.6, 29.44, 29.21, 26.09 (CH_2).IR ν_{max}/cm^{-1} 3691, 3605, 1722, 1601, 1435. ESI-MS =581.23 ($C_{30}H_{38}O_{10}Na^+$, M+Na^+). Yield = 93%

p-Xyxyl – ^{1}H NMR 400 MHz ($CDCl_3$) δ ppm = 8.30 (t, 2H, CH_{Ar}); 7.84 (d, 4H, CH_{Ar}); 7.48 (s, 4H, CH_{Ar}); 5.16 (s, 4H, -O-CH_2); 3.94 (s, 12H, -O-CH_3). ^{13}C NMR 400 MHz ($CDCl_3$) δ ppm = 166.1 (R-C=O); 158.7 (C_{Ar} ^{2}Ph); 136.23 (C-O_{Ar} ^{6}Ph); 131.9 (C_{Ar} ^{8}Ph); 127.9 (C_{Ar} ^{9}Ph); 123.3 (C_{Ar} ^{1}Ph); 120.2 (C_{Ar} ^{5}Ph); 70.1 (CO-CH_2); 52.54 (CO_2-Me). IR ν_{max}/cm^{-1} 3691, 1723, 1598, 1457, 1435. ESI-MS = 545.14 ($C_{28}H_{26}O_{10}Na^+$, M+Na^+). Yield = 78%

4.7.3 General Synthesis of Tetracaroxylic Acids

The tetra ester was suspended in MeOH, 5% NaOH was added and the reaction heated to 60 ^{o}C for 12h. This was then allowed to cool and filtered. The white precipitate (ppt) was collected and washed once with cold MeOH, this was then dissolved in H2O. This solution was filtered then treated with conc. HCl to precipitate out the tetra acid, which was collected by vacuum filtration and dried**.**

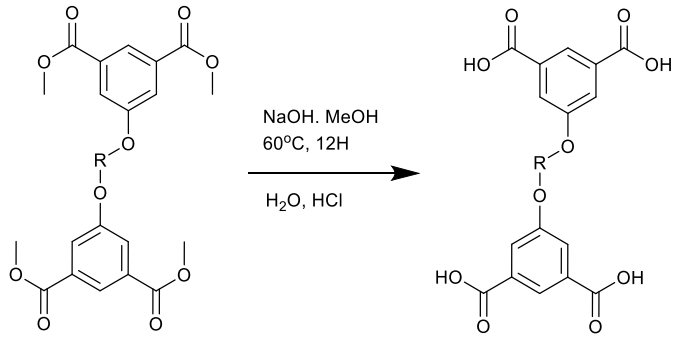

Scheme 4. 6 *General Synthesis of tetracarboxylic acids where R = Ethyl, Pentyl, Decyl and p-Xylyl linker*

Ethyl - ^{1}H NMR (400MHz D_2O, K_2CO_3) δ ppm= 7.93 (t, 2H, -CH_{Ar}); 7.60 (d, 4H, -CH_{Ar}); 4.51 (s, 4H, -O-CH_2). ^{13}C NMR (400 MHz D_2O, K_2CO_3) δ ppm= 177.2 (C=O); 160.4 (C_{Ar} ^{2}Ph); 140.7 (C_{Ar} ^{5}Ph); 124.8 (CH_{Ar} ^{1}Ph); 120.2 (CH_{Ar} ^{4}Ph); 67.0 (H_2C-O); ATR IR ν_{max}/cm^{-1} 3690, 3608, 3048, 2360, 1602,1239. ESI-MS = 389 ($C_{18}H_{15}O_{10}^{+}$, M+H)$^{+}$. Yield = 78%

Pentyl – ^{1}H NMR (400 MHz D_2O, K_2CO_3) δ ppm = 7.84 (t, 2H, -CH_{Ar}); 7.46 (d, 4H, -CH_{Ar}); 3.99 (t, 4H, -O-CH_2); 1.68 (q, 4H, -CH_2); 1.45 (m, 4H, -CH_2); ^{13}C NMR (400 MHz D_2O, K_2CO_3) δ ppm = 177.0 (C=O); 160.5 (C_{Ar} ^{2}Ph); 140.4 (C_{Ar} ^{5}Ph); 124.3 (CH_{Ar} ^{1}Ph); 120.1 (CH_{Ar} ^{4}Ph); 71.2 (CH_2-O); 30.5, 24.2 (CH_2). ATR IR ν_{max}/cm^{-1} 3691, 3605, 1722, 1601, 1435. ESI-MS =581.23 ($C_{30}H_{38}O_{10}Na^{+}$, M+Na^{+}). Yield = 78%

Decyl - ^{1}H NMR (300 MHz D_2O, K_2CO_3) δ ppm = 8.05 (t, 2H, -CH_{Ar}); 7.55 (d, 4H, -CH_{Ar}); 7.51 (s, 4H, -CH_{Ar}); 5.16 (s, 4H, -O-CH_2);. ^{13}C NMR (400 MHz D_2O, K_2CO_3) δ ppm = 177.2 (C=O); 160.8 (C_{Ar} ^{2}Ph); 140.7 (C_{Ar} ^{5}Ph); 124.6 (CH_{Ar} ^{1}Ph); 120.5 (CH_{Ar} ^{4}Ph); 71.6 (CH_2-O); 31.4, 31.1, 31.1, 27.9 (CH_2). ATR IR ν_{max}/cm^{-1} 3690, 3609, 3042, 1653. Yield = 77%

p-Xylyl - ^{1}H NMR (400 MHz D_2O, K_2CO_3) δ ppm = 7.93 (t, 2H, -CH_{Ar}); 7.61 (d, 4H, -CH_{Ar}); 7.51 (s, 4H, -O-CH_2); 5.17 (s, 4H, -CH_2); ^{13}C NMR (400 MHz D_2O, K_2CO_3); 178.8 (C=O); 162.0 (C-C=O ^{2}Ph); 142.3 (C-O ^{5}Ph); 140.7 (C, ^{5}Ph); 132.8 (C, ^{8}Ph); 126.5 (C, ^{1}Ph); 122.2 (C, ^{4}Ph); 74.6 (H_2C-

O); ATR IR ν_{max}/cm^{-1} 3690, 3607, 3051, 3005, 1602,1239. ESI-MS = 465 ($C_{24}H_{17}O_{10}^-$, M-H), 489.10 ($C_{24}H_{17}O_{10}Na^+$, M+Na^+). Yield = 85%

4.7.4 General Synthesis of Barium Salts

The TCA was dissolved in a minimum volume of NaOH to which was added 0.5 equivalent of $BaSO_4$ Stirred for x minutes. Filtered, dried in 40-60^o oven overnight.

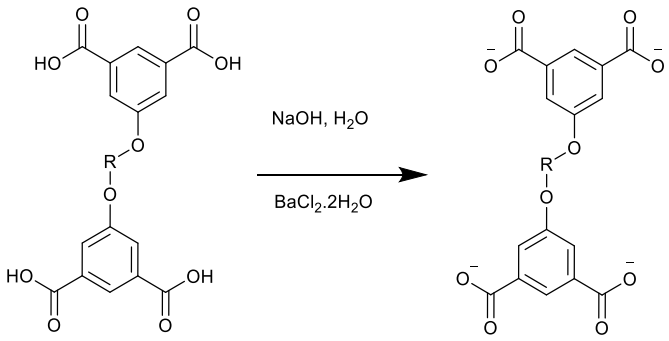

Scheme 4. 7 *Synthesis of tetracarboxylate barium salts where R = Ethyl, Pentyl, Decyl and p-Xylyl linker*

Due to the insolubility of the subsequent barium salts there were no reasonable techniques to identify their structure other than XRD or elemental analysis. The elemental analysis was inconclusive due to inadequate drying and the reactions did not yield single crystals, therefore only the yield is reported here. The characterisation up to this point was considered adequate to continue using the materials as made with the assumption that they were in the form Ba_2TCA.

Ethyl = 63%, Pentyl = 83% , Decyl = 93%, P-xylyl = 85%

4.7.5 General Material Synthesis

Under an inert atmosphere 3-Bpp (0.106 g, 0.5 mmol) and $FeSO_4$ (0.070 g, 0.25 mmol) were dissolved in degassed MeOH (10 mL) upon which the reaction mixture turned a deep red colour. After stirring for 1h a suspension of Ba_2(TCA) (0.125 mmol) in H_2O (10 mL) was added.

The orange precipitate that formed containing $BaSO_4$ was filtered through a Por4 frit (10 – 16 μm) and the precipitate was washed with MeOH (6 mL). The filtrates were combined to obtain an optimum MeOH:H_2O ratio of 5:3 and left undisturbed. An insoluble orange powder formed initially, followed by colourless crystals of 3-Bpp and red plate like crystals of the desired material.

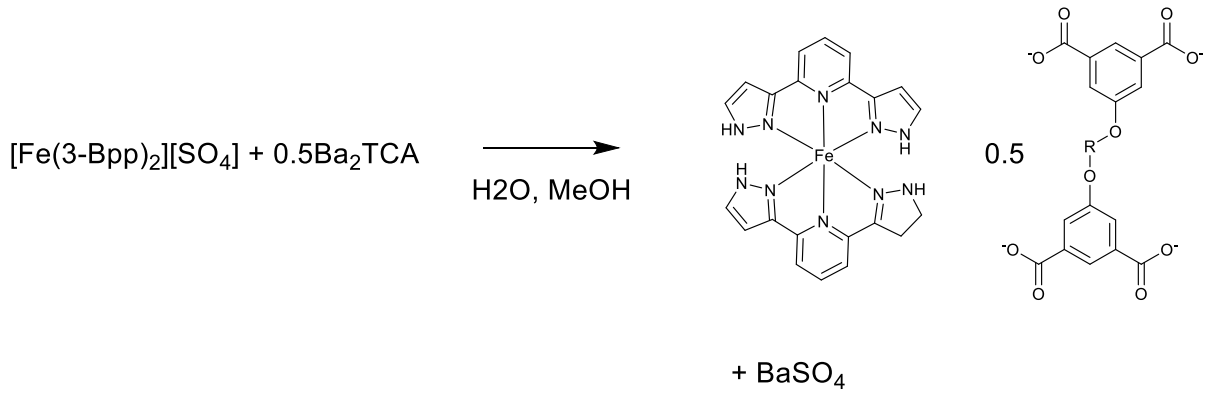

Scheme 4. 8 *General synthetic route for materials where R = Ethyl, Pentyl, Decyl and p-Xylyl linker, TCA = Tetracarboxylate anion of R variation*

$Fe(3\text{-}Bpp)_2TCA\text{-}2C$. $[Fe(3\text{-}Bpp)_2](TCA\text{-}2C).20H_2O$ – Yield N/A crystals not collectable in bulk.

$Fe(3\text{-}Bpp)_2TCA\text{-}5C$. $[Fe(3\text{-}Bpp)_2](TCA\text{-}5C).15H_2O$ –57 mg, 24 % Yield

$Fe(3\text{-}Bpp)_2TCA\text{-}10C$. $[Fe(3\text{-}Bpp)_2]0.5[TCA\text{-}10C].9H_2O$ – 14.4 mg, 6.5 % Yield

$Fe(3\text{-}Bpp)_2TCA\text{-}p$. $[Fe(3\text{-}Bpp)_2]0.5(TCA\text{-}p).2H_2O.2MeOH$ – 66 mg, 32.9 % Yield

4.8 Conclusions

With the exchange of discrete counterions for large high charge and flexibility counterions we were able to show that the favoured terpyridine embrace packing motif is capable of partially distorting to various degrees in order to incorporate these counterions and also to create porous networks which maintain their spin crossover behaviour but not their crystallinity on dehydration. Increasing the size to charge ratio from pentyl to decyl further disrupts the packing motif which becomes dominated by the hydrophobic interactions of the aliphatic chain forming layers of counterions bridged by pillars of cation. Increasing the rigidity and introducing aromaticity in the form of the *p*-xylyl linker completely disrupts the terpyridine embrace. The magnetism of these materials is dominated by the solvent stabilisation of the LS state and the subsequent loss of this solvent due to increased temperature causing a spin transition.

4.9 Appendices

4.9.1 Crystallographic Data

Material	1	2	3	4
Identification code	FEGMLE	FEGMLG1	FEGMLB2	FEGLMF
Empirical formula	$C_{62.02}H_{83.03}Fe_2N_{20}O_{31.02}$	$C_{32.5}H_{41}FeN_{10}O_{12.5}$	$C_{70}H_{62}Fe_2N_{20}O_{25}$	$C_{36}H_{37}FeN_{10}O_9$
M_w	1716.82	827.60	1695.09	809.60
T/K	120.01(10)	117.15	120(2)	120(2)
Crystal system	triclinic	triclinic	monoclinic	monoclinic
Space group	P-1	P-1	P2/c	$P2_1/c$
a/Å	15.9712(10)	8.06380(10)	20.917(3)	9.57070(10)
b/Å	16.1776(10)	15.9966(2)	7.8571(14)	13.4025(2)
c/Å	18.3443(13)	29.8020(4)	24.774(6)	28.4974(3)
α/°	64.905(7)	100.4330(10)	90	90
β/°	64.722(7)	97.1740(10)	106.01(2)	94.1230(10)
γ/°	81.391(5)	93.3120(10)	90	90
Volume/Å^3	3878.5(5)	3738.36(8)	3913.6(14)	3645.94(8)
Z	2	4	2	4
ρ_{calc}g/cm^3	1.470	1.470	1.438	1.475
μ/mm^{-1}	3.843	0.445	3.751	3.920
F(000)	1791.0	1728.0	1748.0	1684.0
Crystal size/mm^3	Na	Na	0.067 × 0.032 × 0.023	0.172 × 0.046 × 0.021
Radiation	CuKα (λ = 1.54184)	(λ = 0.6889)	CuKα (λ = 1.54184)	Cu Kα (λ = 1.54184)
2Θ range for data collection/°	7.31 to 130.178	3.08 to 72.452	7.424 to 177.934	6.22 to 146.826
Index ranges	-26 ≤ h ≤ 25, -5 ≤ k ≤ 9, -30 ≤ l ≤ 31	-11 ≤ h ≤ 11, -16 ≤ k ≤ 16, -19 ≤ l ≤ 35	-13 ≤ h ≤ 13, -26 ≤ k ≤ 26, -49 ≤ l ≤ 49	-18 ≤ h ≤ 18, -18 ≤ k ≤ 17, -21 ≤ l ≤ 21
Reflections collected	17400	19764	80535	62755
Independent reflections	7193 [R_{int} = 0.1307, R_{sigma} = 0.2740]	7157 [R_{int} = 0.0214, R_{sigma} = 0.0227]	34544 [R_{int} = 0.0814, R_{sigma} = 0.0738]	12583 [R_{int} = 0.2166, R_{sigma} = 0.1308]
Data/restraints/parameters	7193/1700/683	7157/0/537	34544/0/1054	12583/21/1065
Goodness-of-fit on F^2	1.096	1.083	1.091	1.029
Final R indexes [I>=2σ (I)]	R_1 = 0.1564, wR_2 = 0.3810	R_1 = 0.0343, wR_2 = 0.0892	R_1 = 0.0996, wR_2 = 0.3226	R_1 = 0.1584, wR_2 = 0.3681
Final R indexes [all data]	R_1 = 0.3999, wR_2 = 0.4811	R_1 = 0.0374, wR_2 = 0.0913	R_1 = 0.1234, wR_2 = 0.3411	R_1 = 0.2453, wR_2 = 0.4408
Largest diff. peak/hole / e Å^{-3}	0.51/-0.44	0.30/-0.38	2.33/-1.85	1.78/-0.66

4.9 References

1 O. Kahn, J. Kröber and C. Jay, *Adv. Mater.*, 1992, **4**, 718–728.

2 G. Molnár, S. Rat, L. Salmon, W. Nicolazzi and A. Bousseksou, *Adv. Mater.*, 2018, **30**, 1–23.

3 O. Kahn and C. J. Martinez, *Science.*, 1998, **279**, 44–48.

4 J. Ferrando-Soria, J. Vallejo, M. Castellano, J. Martínez-Lillo, E. Pardo, J. Cano, I. Castro, F. Lloret, R. Ruiz-García and M. Julve, *Coord. Chem. Rev.*, 2017, **339**, 17–103.

5 M. Urdampilleta, S. Klyatskaya, J. P. Cleuziou, M. Ruben and W. Wernsdorfer, *Nat. Mater.*, 2011, **10**, 502–506.

6 E. Coronado, *Nat. Rev. Mater.*, 2020, **5**, 87–104.

7 P. Gütlich, Y. Garcia and H. A. Goodwin, *Chem. Soc. Rev.*, 2000, **29**, 419–427.

8 M. A. Halcrow, *Chem. Soc. Rev.*, 2011, **40**, 4119–4142.

9 G. Aromí, L. A. Barrios, O. Roubeau and P. Gamez, *Coord. Chem. Rev.*, 2011, **255**, 485–546.

10 A. Bousseksou, G. Molnár, L. Salmon and W. Nicolazzi, *Chem. Soc. Rev.*, 2011, **40**, 3313–3335.

11 G. Molnár, M. Mikolasek, K. Ridier, A. Fahs, W. Nicolazzi and A. Bousseksou, *Ann. Phys.*, 2019, **531**, 1–21.

12 P. Gütlich, A. Hauser and H. Spiering, *Angew. Chemie Int. Ed. English*, 1994, **33**, 2024–2054.

13 G. Chastanet, M. Lorenc, R. Bertoni and C. Desplanches, *Comptes Rendus Chim.*, 2018, **21**, 1075–1094.

14 O. Kahn, *Curr. Opin. Solid State Mater. Sci.*, 1996, **1**, 547–554.

15 E. Tailleur, M. Marchivie, J. P. Itié, P. Rosa, N. Daro and P. Guionneau, *Chem. - A Eur. J.*, 2018, **24**, 14495–14499.

16 A. B. Gaspar, G. Molnár, A. Rotaru and H. J. Shepherd, *Comptes Rendus Chim.*, 2018, **21**, 1095–1120.

17 J. Long Her, Y. H. Matsuda, M. Nakano, Y. Niwa and Y. Inada, *J. Appl. Phys.*, 2012, **111**, 053921.

18 H. L. B. Boström, A. B. Cairns, L. Liu, P. Lazor and I. E. Collings, *Dalt. Trans.*, 2020, **49**, 12940–12944.

19 K. Bairagi, A. Bellec, C. Fourmental, O. Iasco, J. Lagoute, C. Chacon, Y. Girard, S. Rousset, F. Choueikani, E. Otero, P. Ohresser, P. Sainctavit, M. L. Boillot, T. Mallah and V. Repain, *J. Phys. Chem. C*, 2018, **122**, 727–731.

20 L. J. Kershaw Cook, R. Kulmaczewski, R. Mohammed, S. Dudley, S. A. Barrett, M. A. Little, R. J. Deeth and M. A. Halcrow, *Angew. Chemie - Int. Ed.*, 2016, **55**, 4327–4331.

21 W. Nicolazzi and A. Bousseksou, *Comptes Rendus Chim.*, 2018, **21**, 1060–1074.

22 H. Spiering and N. Willenbacher, *J. Phys. Condens. Matter*, 1989, **1**, 10089–10105.

23 W. Nicolazzi, J. Pavlik, S. Bedoui, G. Molnár and A. Bousseksou, *Eur. Phys. J. Spec. Top.*, 2013, **222**, 1137–1159.

24 M. A. Halcrow, *New J. Chem.*, 2014, **38**, 1868–1882.

25 M. A. Halcrow, *Coord. Chem. Rev.*, 2009, **253**, 2493–2514.

26 M. A. Halcrow, *Coord. Chem. Rev.*, 2005, **249**, 2880–2908.

27 L. J. Kershaw Cook, R. Mohammed, G. Sherborne, T. D. Roberts, S. Alvarez and M. A. Halcrow, *Coord. Chem. Rev.*, 2015, **289**–**290**, 2–12.

28 G. A. Craig, O. Roubeau and G. Aromí, *Coord. Chem. Rev.*, 2014, **269**, 13–31.

29 R. Pritchard, C. A. Kilner and M. A. Halcrow, 2007, 577–579.

30 C. A. K. and M. A. Simon A. Barrett and Halcrow, *Dalt. Trans.*, 2011, **40**, 12021–12024.

31 M. del C. Giménez-López, M. Clemente-León and C. Giménez-Saiz, *Dalt. Trans.*, 2018, **47**, 10453–10462.

32 V. Jornet-Mollá, Y. Duan, C. Giménez-Saiz, J. C. Waerenborgh and F. M. Romero, *Dalt. Trans.*, 2016, **45**, 17918–17928.

33 E. Coronado, M. del Carmen Gimenez-Lopez, C. Giménez-Saiz and F. M. Romero, *CrystEngComm*, 2009, **11**, 2198–2203.

34 K. H. Sugiyarto, W. A. McHale, D. C. Craig, A. D. Rae, M. L. Scudder and H. A. Goodwin, *Dalt. Trans.*, 2003, 2443–2448.

35 K. H. Sugiyarto and H. A. Goodwin, *Aust. J. Chem.*, 1988, **41**, 1645–1663.

36 K. Sugiyarto, D. Craig, A. Rae and H. Goodwin, *Aust. J. Chem.*, 1994, **47**, 869.

37 M. Nishio, *Phys. Chem. Chem. Phys.*, 2011, **13**, 13873–13900.

38 Agilent, 2014, CrysAlis PRO. Agilent Technologies Ltd, Yarnton, O.

39 G. M. Sheldrick, *Acta Crystallogr. Sect. A*, 2008, **64**, 112–122.

40 G. M. Sheldrick, *Acta Crystallogr. Sect. C*, 2015, **71**, 3–8.

41 Y. -i Lin and S. A. Lang, *J. Heterocycl. Chem.*, 1977, **14**, 345–347.

42 J. P. Collman, J. I. Brauman, J. P. Fitzgerald, P. D. Hampton, Y. Naruta, J. W. Sparapany and J. A. Ibers, *J. Am. Chem. Soc.*, 1988, **110**, 3477–3486.

Chapter 5

Final Remarks

5.1 Final Remarks

5.1.1 Chapter 2

A novel PdS_x@CNF_m catalyst has been successfully investigated for its catalytic performance towards the HER under acidic conditions. Electrochemical investigation of the PdS_x@CNF_m illustrates the exceptional switchable behaviour of this material and the significant role that the carbon support plays. By cycling between -0.9 V and 1.2V it is possible to irreversibly generate an active PdS_{x-y}@CNF_m which can compete with reported Pt/C parameters by selectively oxidising and reducing the internal folded edge.

It was observed through CA, extended CV experiments and OCP that the performance of the catalyst diminishes but is recovered through subsequent activation experiments. CVs taken before and after these deactivation/recovery experiments were used to indicate the proposed mechanism for activation, which is accelerated with respect to the addition of PdS_x NPs into the CNF_m. Further studies of the activated PdS_{x-y}@CNF_m material will show its ability as a catalyst for other key reactions within PEM-WE and PEMFC.

5.1.2 Chapter 3

Molecule immobilisation for catalysis and magnetic applications requires the functionalisation of more and more complex ligands, the synthetic process has been shown to be possible by the synthesis of previously reported alkene linked compounds (E)-3,5-dichloro-4′-methylstilbene which was successfully applied to a phenyl **3** 3,5-(Dimesityl)-4-Iodo-(E)-Stilbene and pyrene derivative **5** 3,5-(Dimesityl)-4-iodo-(E)-((styryl)pyrene)terphenyl. Crystallographic studies of **5** show that π-π interactions are present in the solid state and could be exploited for immobilisation on

carbon surfaces. Alongside this synthesis, progress was made towards the synthesis of an ether linked compound with the successful synthesis of TIP silyl ether protected and deprotected *para* hydroxy *m*-terphenyl iodides. The choice of linker needs to be stable to lithiation which for **3** and **5** is known from the literature, the acidity of benzylic protons were shown not to be stable. Careful planning of the next steps is necessary in progressing the ether linker synthesis but there is the basis for progressing to the synthesis of metal complexes.

5.1.3 Chapter 4

The synthesis of a range of materials based on $[Fe(3\text{-bpp})_2]_2[TCA].xH_2O$ were synthesised with large high charge TCA counterions. These materials due to the large size and flexibility of the counterion proved difficult to synthesise, the crystallographic analysis of these materials showed that the terpyridine packing motif is robust and can withstand the incorporation of these counterions with minimal disruption as in $Fe(3\text{-Bpp})_2$TCA-2C and $Fe(3\text{-Bpp})_2$TCA-5C. Increasing to a larger counterion or a more rigid counterion it is possible to disrupt the interactions partially in $Fe(3\text{-Bpp})_2$TCA-10C and fully in $Fe(3\text{-Bpp})_2$TCA-*p*. Magnetic measurements confirmed that the spin transitions of the molecules are still dominated by the solvation of the iron centres due to the hydrogen bonding between NH bonds and solvent molecules. Increased yields are required to characterise the materials further.

Concluding Remarks

Chapter 2 introduces a palladium chalcogenide material that is able to switch catalytic performance as potentials are applied. Chapter 3 describes the synthesis of sterically demanding ligands for future applications in materials and catalysts with switchable

properties. Chapter 4 describes the synthesis of a molecular crystalline material with spin cross-over switching in magnetic properties. Overall, materials were developed at the level of nanoparticles, molecules, and molecular crystals as innovative tools in materials design.